

**INTEGRATION OF NANOPOROUS STRUCTURE INTO
VERTICAL ORGANIC FIELD EFFECT TRANSISTOR**

MUHAMMAD ZHARFAN BIN MOHD HALIZAN

**FACULTY OF SCIENCE
UNIVERSITY OF MALAYA
KUALA LUMPUR**

2018

**INTEGRATION OF NANOPOROUS STRUCTURE INTO
VERTICAL ORGANIC FIELD EFFECT TRANSISTOR**

MUHAMMAD ZHARFAN BIN MOHD HALIZAN

**DISSERTATION SUBMITTED IN FULFILMENT OF
THE REQUIREMENTS FOR THE DEGREE OF MASTER
OF SCIENCE**

**DEPARTMENT OF PHYSICS
FACULTY OF SCIENCE
UNIVERSITY OF MALAYA
KUALA LUMPUR**

2018

UNIVERSITY OF MALAYA
ORIGINAL LITERARY WORK DECLARATION

Name of Candidate : **MUHAMMAD ZHARFAN BIN MOHD HALIZAN**

Matric No : **SGR 150066**

Name of Degree : **MASTER OF SCIENCE**

Title of Dissertation :

**INTEGRATION OF NANOPOROUS STRUCTURE INTO VERTICAL
ORGANIC FIELD EFFECT TRANSISTOR**

Field of Study : **EXPERIMENTAL PHYSICS**

I do solemnly and sincerely declare that:

- (1) I am the sole author/writer of this Work;
- (2) This Work is original;
- (3) Any use of any work in which copyright exists was done by way of fair dealing and for permitted purposes and any excerpt or extract from, or reference to or reproduction of any copyright work has been disclosed expressly and sufficiently and the title of the Work and its authorship have been acknowledged in this Work;
- (4) I do not have any actual knowledge nor do I ought reasonably to know that the making of this work constitutes an infringement of any copyright work;
- (5) I hereby assign all and every right in the copyright to this Work to the University of Malaya ("UM"), who henceforth shall be owner of the copyright in this Work and that any reproduction or use in any form or by any means whatsoever is prohibited without the written consent of UM having been first had and obtained;
- (6) I am fully aware that if in the course of making this Work I have infringed any copyright whether intentionally or otherwise, I may be subject to legal action or any other action as may be determined by UM.

Candidate's Signature

Date:

Subscribed and solemnly declared before,

Witness's Signature

Date:

Name:

Designation:

INTEGRATION OF NANOPOROUS STRUCTURE INTO VERTICAL ORGANIC FIELD EFFECT TRANSISTOR

ABSTRACT

Since the last three decades, a lot of endeavours have been done by researchers to enhance the performance of Organic Field Effect Transistor (OFET) by altering the organic semiconductors properties through modifying the molecular/monomeric units or doping the semiconductor materials. The challenges are to increase the output current, to increase the ON/OFF ratio and to decrease the turn on voltage. Vertical Organic Field Effect Transistor (VOFET) is a new structure of OFET which has the vertical structure instead of lateral. By having the vertical designation, this type of transistor enabled to have way smaller channel length between drain and source which is in nanoscale compared to lateral OFET's microscale. The current industrial market is focusing on the lateral OFET and therefore, by providing the alternative of vertical structure of organic material-based transistor, the enhancement can be achieved. For the first phase, the fabrication of in-situ anodic alumina template (AAO) directly onto glass substrate is realized. Uniformity and density of pore size, can be respectively tuned by varying the stirring speeds (0 – 300 rpm) and molarity of pore widening agent (0 – 10 % of phosphoric acid). Consequently, template with 100 rpm stirring rate has a better uniformity with 1540 pores compared to 0, 50 and 200 rpm. Furthermore, the pore widening technique using phosphoric acid is studied by varying its concentrations. Occurrence of merging pores is observed by increasing the molarity of acid to 10 % which unlikely to happen in the lower molarity of 5 % phosphoric acid. Porous alumina template will then be used to infiltrate vanadyl 2, 9, 16, 23-tetraphenoxy- 29H, 31H-phthalocyanine (VOPcPhO) prior to the formation of alumina:VOPcPhO nanocomposite. Studies of template production on top of different substrates are done with glass and ITO substrates. As the result, both of these substrates produced templates with almost similar total number of pores of 1540 and 1455 for glass

and ITO substrate, respectively. In the second part, this work aims at improving the performance of VOFET by synthesizing the different morphology of dielectric layer; porous and non-porous to be used in the fabrication of 3-dimensional (3D) VOFET. To produce the 3D VOFET, porous alumina template is applied as to allow the replicating process between the template and P(VDF-TrFE) to occur. It is found that the replicating process has generated the porous structure of P(VDF-TrFE). The study on the VOFET fabrication is done where the preparation of dielectric layer (copolymer P(VDF-TrFE)), spin coating of silver nanowire, semiconducting material (VOPcPhO) and deposition of aluminium are carried out. Two systems are prepared in this study; (i) thin film copolymer (without the application of alumina template) and (ii) nanostructured copolymer (with the application of alumina template). VOFET without the porous has the current of 3.5×10^{-4} A obtained at drain-source voltage (V_{DS}) of 25 V with the turn-on voltage of 10 V. Meanwhile, the VOFET integrated with porous recorded a better current of 2.0×10^{-3} A at V_{DS} of 25 V with the turn-on voltage of 7 V. The novelty of this work is, the fabrication of nanostructured copolymer and its integration into VOFET which has enhanced the output currents and turn on voltages.

Keywords: AAO template, nanoporous structure, P(VDF-TrFE), silver nanowire, VOFET.

PENGINTEGRASIAN STRUKTUR LIANG NANO KE DALAM TRANSISTOR KESAN KAWASAN ORGANIK

ABSTRAK

Sepanjang tiga dekad lalu, pelbagai usaha dijalankan oleh penyelidik bagi meningkatkan kemampuan Transistor Kesan Kawasan Organik (OFET) sama ada mengubahsuaikan sifat-sifat semikonduktor organik melalui pengubahsuaian unit-unit molekulnya atau pendedapan bahan semikonduktor lain. Halangan-halangan yang dihadapi oleh penyelidik ialah untuk meningkatkan arus keluaran, nisbah BUKA/TUTUP dan mengurangkan voltan bukaannya. Transistor Kesan Kawasan Organik Menegak (VOFET) ialah satu struktur OFET yang mempunyai struktur menegak dan bukannya melintang. Transistor jenis rekaan menegak ini membolehkan untuk mempunyai jarak ruang antara elektrod 'longkang' dan 'sumber' yang jauh lebih kecil iaitu dalam skala nano jika dibandingkan dengan skala mikro dalam OFET melintang. Pada masa kini, transistor keluaran industri lebih menekankan mengenai penghasilan OFET melintang. Justeru, dengan menyediakan alternatif kepada mereka dengan transistor struktur menegak yang berasaskan bahan organik, penambahbaikan boleh dicapai. Bagi fasa pertama dalam kajian ini, pembuatan acuan anodik alumina (AAO) terus ke substrat kaca dicapai. Keseragaman dan kepadatan saiz liang boleh ditala dengan mengubah kelajuan kacauan (0 – 300 rpm) dan kepekatann ejen pelebaran liang (0 – 10 % fosforik asid). Hasilnya, bagi parameter kelajuan kacauan, acuan dengan 100 putaran per minit (rpm) kadar kacauan mempunyai keseragaman liang nano yang lebih baik dengan 1540 bilangan struktur liang nano dibandingkan dengan acuan dengan kadar 0, 50 dan 200 rpm. Selain itu, teknik pembesaran liang nano menggunakan kepekatan fosforik asid yang berbeza telah dilakukan. Berlakunya penggabungan liang dengan meningkatkan kepekatan asid kepada 10 % yang mana tidak mungkin berlaku dalam kepekatan yang lebih rendah iaitu sebanyak 5 % asid fosforik. Acuan alumina kemudian boleh digunakan

untuk dimasuki oleh vanadyl 2, 9,16, 23-tetraphenoxy - 29H, 31H-phthalocyanine (VOPcPhO) sebelum penghasilan alumina: VOPcPhO komposit nano. Akhir sekali, kajian penghasilan acuan di atas substrat yang berbeza dilakukan dengan substrat kaca dan substrat ITO. Hasilnya, kedua-dua substrat ini menghasilkan templat dengan jumlah total struktur liang nano yang hampir sama dengan 1540 dan 1455 untuk masing-masing substrat kaca dan ITO. Bagi fasa kedua, kerja-kerja ini bertujuan meningkatkan prestasi VOFET dengan menghasilkan morfologi lapisan dielektrik yang berbeza; berliang dan bebas-berliang untuk digunakan dalam pembuatan 3-dimensi (3D) VOFET. Untuk menghasilkan 3D VOFET, acuan alumina berliang nano digunakan untuk membenarkan proses peniruan antara acuan dan P(VDF-TrFE) berlaku. Ia didapati bahawa proses peniruan telah menjana struktur berliang pada permukaan P(VDF-TrFE). Kajian mengenai penghasilan VOFET telah dijalankan di mana penyediaan lapisan dielektrik (ko-polimer P(VDF-TrFE)), pelapisan secara berputar bagi wayar nano perak dan bahan semikonduktor (VOPcPhO) serta pelapisan aluminium telah dilaksanakan. Dua sistem telah disediakan bagi kajian ini (i) lapisan ko-polimer yang rata (tiada aplikasi acuan alumina) dan (ii) lapisan ko-polimer yang mempunyai struktur nano (dengan aplikasi acuan alumina). VOFET tanpa liang nano mempunyai arus sebanyak 3.5×10^{-4} A yang diperolehi di voltan longkang-sumber (V_{DS}) pada 25 V dengan voltan bukaan sebanyak 10 V. Sementara itu, VOFET yang bersepadu dengan liang nano mencatatkan arus lebih baik 2.0×10^{-3} A dengan V_{DS} 25 V dengan voltan bukaan sebanyak 7 V. Pembaharuan bagi kajian ini ialah mengenai pemfabrikasian ko-polimer dengan struktur nano dalam VOFET yang telah meningkatkan arus keluaran dan voltan bukaan transistor ini.

Kata kunci: Acuan alumina, struktur liang nano, P(VDF-TrFE), wayar nano perak, VOFET.

ACKNOWLEDGEMENTS

Alhamdulillah thanks to Allah for His willing that enable me to finish my Master degree. He gave me incredible strength to do and focus to my research almost every day. I shall give my gratitude to my supportive supervisor, Dr. Azzuliani binti Supangat who gave her trust in me to conduct such a tough yet interesting research works that further enhance my ability and potential. I am also indebted to my mentor, Dr. Shahino for his guidance and patience in guiding me towards fabrication of VOFET.

I am very well appreciate supports and assists from my OERG group members, Dr. Khaulah Sulaiman, Dr. Qayyum, Dr. Mansoor, Syifa, Haaziq, Izzat, Saipul, Asma, Lim and Doris whom helped me and gave me a lot of interesting experiences before. Many thanks to other LDMRC members who helped me as a newbie before, Mr. Arif, Mr. Mad, Kak Lela, Kak Ain, Kak Lin and Fa that guide me to feel comfortable with our lab.

Many thanks to my family who gave me strength to accomplish my studies. Thank you to my mom, A'abidah binti Ishak for her kind spiritual support and guidances. Worth to mention for, thanks to my sister, Zayree Azna Halizan and my brothers, Yusri Halizan and Zulfadli Halizan for their supports and toleration with me. Thanks too to my friends, Farah Norazlin Azmi and Diyana Hambali for their kind support and guidances as a peer in Master Degree.

Last but not least, thanks to all physics departments' lecturers and staffs especially LDMRC's and colleagues whom contributed in any means in accomplishing my studies.

Muhammad Zharfan Mohd Halizan

TABLE OF CONTENTS

ABSTRACT	iii
ABSTRAK	v
ACKNOWLEDGEMENT	vii
LIST OF FIGURES	xi
LIST OF TABLES	xv
LIST OF SYMBOLS AND ABBREVIATIONS	xvi
CHAPTER 1: INTRODUCTION	1
1.1 Introduction	1
1.2 Motivation	2
1.3 Research Objective	3
1.4 Thesis Framework	4
CHAPTER 2: BACKGROUND AND LITERATURE REVIEWS	5
2.1 Introduction	5
2.2 Transistor I-V Measurements	7
2.3 Field Effect Transistor	8
2.3.1 Junction Field Effect Transistor (JFET)	9
2.3.2 Metal Oxide Semiconductor Field Effect Transistor (MOSFET)	10
2.4 Material for Organic Field Effect Transistor	11
2.4.1 Structure of Organic Field Effect Transistor	13
2.4.2 Mechanism of Organic Field Effect Transistor	14
2.5 Vertical Organic Field Effect Transistor	16
2.5.1 Mechanism of Vertical Organic Field Effect Transistor	17
2.6 Anodic Aluminium Oxide (AAO) Template	18

CHAPTER 3: MATERIALS AND EXPERIMENTAL PROCEDURES.....	21
3.1 Introduction	21
3.2 Material and Chemicals.....	22
3.2.1 P(VDF-TrFE)	22
3.2.2 MEK.....	23
3.2.3 VOPcPhO.....	24
3.2.4 Chloroform.....	25
3.2.5 Isopropanol Alcohol.....	25
3.2.6 Anodic Aluminium Oxide (AAO)	26
3.2.7 Silver Nanowire	27
3.3 Fabrication Techniques	28
3.3.1 Substrate Cleaning Process	28
3.3.2 Preparation of P(VDF-TRFE) Process.....	28
3.3.3 Thermal Evaporation Process	29
3.3.4 Anodization Process.....	30
3.3.5 Spin coating Deposition Process.....	31
3.4 Measurement and Characterizations	32
3.4.1 Morphological Analysis	32
3.4.2 Phase Analysis	35
3.4.3 Bonding Analysis	36
3.4.4 Optical Properties Analysis	38
3.4.4.1 Ultraviolet visible Light Spectroscopy (UV-vis).....	38
3.4.4.2 Photoluminescence (PL) Spectroscopy.....	39
3.4.5 Structural Analysis	41
3.4.6 Profilometer Characterization	42
3.4.7 I-V Characterization	43

CHAPTER 4: SYNTHESIS OF POROUS AAO TEMPLATES.....	45
4.1 Introduction.....	45
4.2 Results and Discussion.....	45
4.2.1 Anodization Process.....	45
4.2.2 Synthesis Porous Alumina and Alumina:VOPcPhO Nanocomposite	47
4.2.3 Optical Characteristics of Porous Alumina And Alumina:VOPcPhO Nanocomposite.....	59
4.2.4 Anodization Process onto Glass and ITO Substrate	64
4.3 Summary	67
CHAPTER 5: THIN FILM VOFET AND NANOSTRUCTURED VOFET.....	69
5.1 Introduction.....	69
5.2 Results and Discussion.....	69
5.2.1 Alumina Porous Template and P(VDF-TrFE)	69
5.2.2 Anodization of Aluminium:P(VDF-TrFE)	72
5.3 Summary	79
CHAPTER 6: CONCLUSION AND FUTURE WORKS	81
6.1 Conclusions.....	81
6.2 Future Works.....	82
REFERENCES	83
LIST OF PUBLICATIONS AND PAPER PRESENTED.....	90

LIST OF FIGURES

Figure 2.1 :	(a) Output and (b) Transfer characteristics of FET (Fan et al., 2004), and (c) FET structure (Bao et al., 1996).....	9
Figure 2.2 :	Schematic diagram of JFET and (b) symbol of JFET (https://www.allaboutcircuits.com/textbook/semiconductors/chpt-2/junction-field/effect-transistors).....	10
Figure 2.3 :	(a) Schematic diagram of JFET and (b) symbol of MOSFET (http://courses.egr.uh.edu/ECE/ECE4339/Class%20Notes/MOSFET_illustration.html).....	10
Figure 2.4 :	Three types of OFET structure arrangements of (a) top-contact bottom-gate OFET, (b) bottom-contact bottom-gate OFET and (c) bottom-contact top-gate OFET.....	14
Figure 2.5 :	Operation mechanism of OFET for (a) <i>n</i> -type semiconductor and (b) <i>p</i> -type semiconductor (Facchetti, 2007).....	15
Figure 2.6 :	Structural difference between (a) lateral OFET or conventional FET and (b) vertical OFET.....	17
Figure 2.7 :	Patterned source electrode in VOFET as reported by Ben Sasson et.al, 2009.....	17
Figure 2.8 :	Schottky barrier mechanism at (a) no bias and (b) at positive gate bias for <i>n</i> -type semiconductor material where Φ_m = barrier height of metal, E_{fmetal} = Fermi energy of metal, E_c = conduction energy of semiconductor, E_f = Fermi energy of semiconductor and E_v = valence energy of semiconductor.....	18
Figure 2.9 :	(a) Schematic diagram (Balde et al., 2015) and (b) FESEM image of an AAO template.....	20
Figure 3.1 :	Flowcharts of research methodology.....	21
Figure 3.2 :	(a) Chemical structure and (b) visual image of P(VDF-TrFE).....	22
Figure 3.3 :	(a) Chemical structure of MEK and (b) visual image of MEK.....	23
Figure 3.4 :	(a) Chemical structure (Abdullah et al., 2012) and (b) visual image of VOPcPhO.....	24
Figure 3.5 :	(a) Chemical structure and (b) visual image of chloroform.....	25

Figure 3.6 :	(a) Chemical structure and (b) visual image of IPA.....	26
Figure 3.7 :	(a) Cross-sectional and (b) top-view FESEM images of AAO template.....	27
Figure 3.8 :	(a) FESEM image of silver nanowire and (b) visual image of silver nanowire in IPA solvent.....	28
Figure 3.9 :	Schematic diagram of preparation of P(VDF-TrFE).....	29
Figure 3.10:	(a) Thermal evaporator Auto-Edward 306 and (b) Schematic diagram of thermal evaporator during aluminium coating process.....	30
Figure 3.11:	Schematic diagram of (a) anodization process from aluminium thin film to porous alumina and (b) pore widening process.....	31
Figure 3.12:	(a) Schematic diagram of anodization process and (b) Protech model 631D water bath.....	31
Figure 3.13:	(a) Schematic diagram of spin coating method during spinning process and (b) Laurell P6000 spin coater.....	32
Figure 3.14:	(a) Visual image and (b) schematic diagram of JSM 7600-F FESEM-EDX.....	34
Figure 3.15:	(a) Visual image and (b) schematic diagram of SU 8000 XRD.....	36
Figure 3.16:	(a) Visual image and (b) schematic diagram of Nicolet i10 FTIR.....	37
Figure 3.17:	(a) Visual image and (b) schematic diagram of Lambda 750 UV-Vis spectroscopy.....	38
Figure 3.18:	(a) Visual image and (b) schematic diagram of PL spectroscopy.....	40
Figure 3.19:	Schematic diagram of Raman spectroscopy.....	41
Figure 3.20:	(a) Visual image and (b) schematic diagram of KLA Tencor stylus-type profilometer.....	43
Figure 3.21:	I-V Measurement Set-up.....	44
Figure 4.1 :	Anodization graph of (a) with and (b) without stirring process.....	46

Figure 4.2 : (a) Pores formation from pure Al, cracking process to nanochannel production and (b) movements of ions during anodization process.....	46
Figure 4.3 : FESEM images of AAO template with 5 % of phosphoric acid (widening) at stirring speed of (a) 0 rpm, (b) 50 rpm, (c) 100 rpm, (d) 200 rpm, and (e) 300 rpm (outset is a plot profile).....	49
Figure 4.4 : 3-Dimensional surface plot of AAO template with 5 % of phosphoric acid (widening) at stirring speed of (a) 0 rpm, (b) 50 rpm, (c) 100 rpm, (d) 200 rpm, and (e) 300 rpm (the analysed surface area is 628 nm x 660 nm).....	50
Figure 4.5 : FESEM images of AAO template at stirring speed of 100 rpm with (a) no pore widening, (b) widening in 5 % phosphoric acid and (c) widening in 10 % phosphoric acid (outset is a plot profile).....	53
Figure 4.6 : Surface plot of AAO template at stirring speed of 100 rpm with (a) no pore widening, (b) widening in 5 % phosphoric acid and (c) widening in 10 % phosphoric acid.....	54
Figure 4.7 : FESEM images of AAO: VOPcPhO nanocomposite in (a) top-view and (b) cross-section view, (c) surface plot of AAO: VOPcPhO nanocomposite and (d) 3D simulation of AAO: VOPcPhO nanocomposite surface.....	56
Figure 4.8 : Chart distribution of template with pores diameter of (a) 0 rpm, (b) 50 rpm, (c) 100 rpm, (d) 200 rpm, (e) widening in 5 % phosphoric acid and (f) widening in 10 % phosphoric acid.....	58
Figure 4.9 : UV-vis spectra of (a) transmittance and (b) absorption of AAO:VOPcPhO nanocomposite.....	60
Figure 4.10: (a) PL spectra and (b) Raman spectra of AAO:VOPcPhO nanocomposites.....	64
Figure 4.11: FESEM image of AAO on (a) glass and (b) ITO with stirring rate of 100 rpm in sulphuric acid.....	65
Figure 4.12: Chart distribution of template with 100 rpm stirring on (a) glass and (b) ITO substrates.....	65
Figure 4.13: 3D surface plot of AAO template on (a) glass and (b) ITO substrates.....	66

Figure 4.14: FESEM images of AAO under anodization of 40 V on (a) glass and (b) ITO.....	66
Figure 5.1 : (a) FESEM image, (b) cross-sectional simulation view, (c) 3D simulation view and (d) EDX of AAO template.....	70
Figure 5.2 : (a) & (b) FESEM images and (c) cross-sectional simulation view of P(VDF-TrFE).....	70
Figure 5.3 : Graph of (a) FTIR and (b) XRD before and after P(VDF-TrFE) soaked in anodization electrolytes.....	72
Figure 5.4 : Anodization graph of (a) aluminium and (b) aluminium: P(VDF-TrFE).....	73
Figure 5.5 : FESEM images of (a) P(VDF-TrFE) thin film and (b) nanostructured P(VDF-TrFE).....	74
Figure 5.6 : Cross-sectional view of fabricated VOFETs of (a) P(VDF-TrFE) thin film and (b) nanostructured P(VDF-TrFE).....	75
Figure 5.7 : Output graph of VOFET integrated with (a) P(VDF-TrFE) thin film & (c) nanostructured P(VDF-TrFE). Transfer graph of VOFET integrated with (b) P(VDF-TrFE) thin film (d) nanostructured P(VDF-TrFE).....	76
Figure 5.8 : Schematic diagram of differences in effective contact areas between single silver nanowire and VOPcPhO of (a) non-porous and (b) porous structures.....	79

LIST OF TABLES

Table 3.1: Descriptions of IV characterization equipment.....	44
Table 4.1: Peaks absorption of alumina: VOPcPhO nanocomposites.	61
Table 4.2: Photoluminescence peaks of alumina: VOPcPhO nanocomposites.	62
Table 4.3: Raman shift and assignments of alumina: VOPcPhO nanocomposites.....	63
Table 4.4: Results of different stirring rates.	67
Table 4.5: Results of different substrates.....	68
Table 5.1: IV curve data of thin film and nanostructured dielectric layer.....	80

University of Malaya

LIST OF SYMBOLS AND ABBREVIATIONS

A	:	Ampere
AAO	:	Anodic Aluminium Oxide
FTIR	:	Fourier Transform Infrared
FESEM	:	Field Emission Scanning Electron Microscopy
IPA	:	Isopropanol Alcohol
ITO	:	Indium Tin Oxide
I-V	:	Current-Voltage
mA	:	Milliampere
MEK	:	Methyl Ethyl Ketone
nm	:	Nanometer
OFET	:	Organic Field Effect Transistor
OPV	:	Organic Photovoltaic
PL	:	Photoluminescence
P(VDF-TrFE)	:	Poly (vinylidene fluoride-trifluoroethylene)
s	:	Seconds
UV-vis	:	Ultraviolet-visible Spectroscopy
V	:	Voltage
V_{DS}	:	Drain-Source Voltage
V_{GS}	:	Gate-Source Voltage
VOFET	:	Vertical Organic Field Effect Transistor
VOLED	:	Vertical Organic Light Emitting Diode
VOPcPhO	:	Vanadyl 2, 9, 16, 23-tetraphenoxy- 29H, 31H-phthalocyanine
XRD	:	X-Ray Diffraction

CHAPTER 1: INTRODUCTION

1.1 Introduction

Over the last two decades, studies in organic semiconductor have instigated with much potential can be explored. At that time, new findings started to fulfil the potential and promises where organic electronics started to challenge the properties of inorganic electronics. This organic semiconductor studies then applied in various devices, famously the transistor and diodes. However, over the years, inorganic electronics sector still possess higher performance if compared with the organic electronics devices such as transistor that performed at low current output and high working voltage which may up to 100 V generally (Wang et al., 2003). Therefore, researchers in organic electronics field need to study a new and fresh idea to increase the performance of organic electronics devices likewise Organic Field Effect Transistor (OFET) so that it can be applied in various applications such as active-matrix flat panel. Therefore, idea of increasing the dielectric constant of dielectric layer (Dimitrakopoulos et al., 1999; Wang et al., 2004) or reconstructing the structure of OFET towards vertical structure does took place (Ma & Yang, 2004).

In this work, we are going to fabricate the vertical OFET structure to study its performance. Electrical properties studies will be done besides morphology study. Our new idea is to alter the structure of dielectric layer (P(VDF-TrFE)) so that we can study its correlation with the performance of vertical OFET. Detailed knowledge about the working mechanism of altered vertical OFET can be applied for theoretical studies and optimizing the vertical OFET in the future.

1.2 Motivation

In this work, we plan to develop a new way or technique to improve the output current of OFET by applying vertical structure in OFET. By having this special structure, we can develop a new type of OFET with a very short (~ 10 nm) channel between semiconductor and source electrode. To fully understand the behaviour of vertical OFET (VOFET), we are planning to study this structure by using VOPcPhO as the semiconductor layer with presence of silver nanowire as the source layer and β -phase P(VDF-TrFE) copolymer as dielectric layer. Integrating this type of phase in this copolymer as a dielectric layer in a transistor is advantageous as this can ease in tunnelling the charge carriers through the layers within VOFET. P(VDF-TrFE) has been proven to have excellent effect towards the metal insulator capacitor electrical performance (Ismail et al., 2015). Since dielectric layer in VOFET will act as a capacitor cell structure, it could potentially increase the electrical properties of the VOFET. VOPcPhO is a good semiconductor material with relatively excellent mobility of $15.5 \times 10^{-3} \text{ cm}^2 \text{ v}^{-1} \text{ s}^{-1}$ as a single material (Azmer et al., 2014). The application of silver nanowire is included as to produce flexible device with high conductivity. VOFETs concept has been reported by Professor Yang Yang (Yang & Wudl, 2006) and his team back in 2004 where they succeeded to fabricate the VOFET with active cell on top of capacitor cell structure. Their device consists of drain electrode, source electrode, gate electrode, substrate, dielectrics, and organic semiconductor. The fabricated VOFET produced high output current $10 \times 10^{-3} \text{ A cm}^{-1}$ with low working voltage and high ON/OFF ratio.

In this work, we plan to further enhance the performance of VOFET by altering the structure of P(VDF-TrFE) as reported works claimed to enhance performance of OFET by introducing the different microstructures in dielectric layer P(VDF-TrE) by electric field treatment (Ashar & Narayan, 2017). Therefore, we would like to try another

technique of AAO template-assisted to form patterned dielectric surface which we believe has positive effects towards the performance of VOFET in our work.

1.3 Research Objectives

Objectives of this work are:

- To deposit the anodic alumina template (AAO) template on substrates.
- To study the morphological, structural and optical properties of AAO templates.
- To fabricate the non-porous and porous VOFET.

University of Malaya

1.4 Thesis Framework

Chapter 2 elaborates the working mechanism and principle of Field Effect Transistor (FET), Organic Field Effect Transistor (OFET) and Vertical Organic Field Effect Transistor (VOFET). Besides, this chapter describes the detailed background of past researches and current study that related to the research topics. Chapter 3 presents the materials and experimental techniques employed in this research. All characterization procedures consist of optical, morphological, structural and electrical procedures carried out during the study are presented. Chapter 4 discusses on the results of the anodization of nanoporous alumina templates obtained by varying the parameters. These discussions cover the electrical, morphological, structural and optical properties of nanoporous alumina templates. Chapter 5 outlines the findings of integrated copolymer and nanoporous alumina template, which led to the fabrication of VOFET. Emphasize is given on the discussion of electrical properties of fabricated VOFET. Chapter 6 can be divided into two sections where the primary section is the summary of the whole research works and the later section consists of suggested future works.

CHAPTER 2: BACKGROUND AND LITERATURE REVIEWS

2.1 Introduction

From 1980s till now, organic semiconductor sectors have utilised applications of unique organic semiconductor devices such as Organic Field Effect Transistors (OFETs) and Organic Light Emitting Diodes (OLEDs) (Geffroy et al., 2006; Minami et al., 2015; Muccini, 2006; Rost et al., 2004; Scharber et al., 2006; Sun et al., 2005; Wu et al., 2008). OFETs possess some advantages such as cheaper, ability to be fabricated in enormous scale and ability to be folded or cut. Commercial transistors will require the low operating voltage, high electron or holes mobility and high ON/OFF ratio. To achieve these criteria, a new organic semiconductor must be developed. Recently, performance or mobility of synthesized organic semiconductors are comparable to the amorphous-silicon-based FETs (Yamashita, 2009). OFETs have the ability to perform well, however, its operational voltage still higher than the inorganic FETs. This is mainly due to the high resistance of OFET besides its low charge carrier mobility. Enhancing its electrical characteristics is one of the major efforts in ensuring to the production of reliable transistor. By altering the architecture of OFET from planar to vertical, one can expect the low series resistance and low turn on voltage. Basically, reducing or shortening the length's channel between source and drain can decrease the low operational voltage. In OFET, channel thickness of around tens of micrometres could produce around tens of operational voltage (So, 2009). Meanwhile in VOFET the channel between source and drain electrode will be in hundreds of nanometres that is far shorter than in planar OFET and thus possible in lowering the operational voltage to only a few volts. With the vertical structure, the gate capacitor will act as a supercapacitor with all the gate bias falling on the electrode interface (Ben-Sasson et al., 2009). With the vertical structure, the gate capacitor will act as a supercapacitor with all the gate bias falling on the electrode interface (Ben-Sasson & Tessler, 2011).

In a VOFET structure, dielectric layer is important as current barrier and at the same time as the passage for the charge polarizations from the gate electrode bias. There are numbers of dielectric polymers available and PVDF homopolymer and copolymers such as Polyvinylidene fluoride Trifluoroethylene P(VDF-TrFE) are potentially to be explored due to their ability to stabilize their chemical composition and high spontaneous polarization. Polyvinylidene fluoride (PVDF) homopolymer and its copolymer have been extensively studied due to their excellent properties of dielectricity, piezoelectricity and ferroelectricity (Furukawa, 1989; Latour & Moreira, 1986; Nakagawa et al., 2016). In order to achieve permanent polarization in P(VDF-TrFE), any mechanical stretching to obtain the crystal structure with dipole is not needed (Weber et al., 2010). This copolymer possesses a wide band gap which acts as insulator and has crystallites structure that is interconnected like maze or rice, with a width within 60 - 120 nm. By annealing its structure, the crystallinity can be enhanced (Naber et al., 2005). Four types of crystalline phases available in P(VDF-TrFE) copolymer i.e. β (initial phase), α (second phase), γ (third phase) and δ (final phase) (Xu et al., 2000). β -phase has large spontaneous polarization along b -axis where this axis is perpendicular to the direction of polymer chain and thus parallel to C-F dipole moment (Hu et al., 2009). P(VDF-TrFE) is a good dielectric polymer with the dielectric constant is between 7.8 and 11 (Mao et al., 2011) at room temperature. By having β -phase copolymer with its low dielectric constant make it possible to be used as dielectric layer in transistor since it can assist in charge carrier movements between layers.

In addition to the dielectric layer properties, the choice of organic material as an organic layer of the active channel in VOFET is deemed important. In the active channel of VOFET, the three main layers are essential that composed of drain electrode, organic layer and source electrode. Vanadyl 2,9,16,23-tetraphenoxy-29H,31H-phthalocyanine (VOPcPhO) is a small molecules semiconductor organic material that widely used in

OPVs, humidity sensor and photo-detectors (Abdullah et al., 2012; Azmer et al., 2016; Kamarundzaman et al., 2013). It is widely regarded for its excellent characteristics such as semi-conductive, photo-conductive and high thermal stabilities (Supangat et al., 2014). It has a tendency to produce a low operational voltage and thus potential to be used in VOFET. Nanostructured source electrode such as silver nanowire has the probability to generate a low sheet resistance and thus, low operational voltage. Silver nanowires have been given the attention for their excellent in thermal, optical and electrical properties (Sun, 2010). Silver nanowire films are highly transparent with diffusive transmittance is $\sim 95\%$ at a wavelength of 550 nm. Besides, it is very conductive with sheet resistance of $\sim 10 \Omega/\text{sq.}$ and can exhibit higher flexibility (Song et al., 2013). Pertaining to their outstanding properties, silver nanowire is promising material to be used as a source electrode in VOFETs.

2.2 Transistor I-V Measurements

I-V characteristic curves of electronic devices are a set of graphical curves that are used to define its operation within an electrical circuit. I-V graphs show the relationship between the applied voltage and the current that flow through the electronic devices. I-V curves usually used to learn the parameters and basic characteristics of a device. In addition, the mathematical model of device's behaviour can be performed from the characteristic of I-V curves. If the voltage applied to the resistive element was varied, one can calculate the current across the terminals with $I = V/R$ which known as Ohm's Law equation. Therefore, from this equation, it is possible to construct the relationship graph between voltages and current (I-V graph). I-V measurements indeed is important in showing us on the operation and mechanisms of electronic devices by combining the current and voltage as a graphical presentation to aid our understanding visually on the behaviour of current within circuit (<http://www.electronics-tutorials.ws/blog/i-v-characteristic-curves.html>)

2.3 Field Effect Transistor

Field Effect Transistor (FET) is a transistor which able to amplify signals whether analogue or digital. Usually, this type of transistor is applied to amplify weak signals such as wireless signals. Apart of that, FET can be functioned as oscillator or switching DC. For this transistor to be functioned, current must flow into the channel, which is composing of semiconductor materials. Besides, two electrodes of 'source' and 'drain' are located at the bottom and top of channel layer, respectively. One can control the effective electrical current by altering its voltage, which then controls the so-called 'gate' electrode. Conductivity of FET is changing depending on the amount or scale of electrical diameter of the channel. To understand this, a tiny alter in voltage of gate electrode can cause much change of current from source to drain. As an amplifier, FET operates this way to amplify incoming signals. There are two well-known FETs that utilize inorganic materials, namely Junction Field Effect Transistor (JFET) and Metal Oxide Semiconductor Field Effect Transistor (MOSFET). FET is very preferred in small or weak signals processing (e.g. in wireless communications or broadcast receivers) and circuits that need the high impedance. However, this type of transistor is not suitable for high power system amplification. To be used in small amplification system, FET will be fabricated into Integrating Circuit (IC) chips. A single IC can contain many thousands of FETs, along with other components such as resistors, capacitors, and diodes. Figure 2.1 (a-c) exhibit the example of output and transfer characteristics of FET and its structure. Many efforts have been done to enhance the output value of FET. One of the efforts is to integrate the inorganic materials such as zinc oxide nanowires (Fan et al., 2004) and silicon nanowires (Cui et al., 2003) to increase the output values with electron mobility around $1350 \text{ cm}^2/\text{Vs}$ is successfully achieved. Apart from that, carbon nanotube is well-known for application in FET to increase its performance. One of the results obtained from other researchers' work is about $25 \mu\text{A}$ at drain-source voltage (V_{DS}) of 0.6 V with

palladium metal used as drain electrode (Javey et al., 2003). Bio-related approach even done in integrating carbon nanotube with FET, by introducing DNA template to form carbon nanotube to enhance the interconnection between carbon nanotube with about 3.5 μA output current at 3 V_{DS} (Keren et al., 2003).

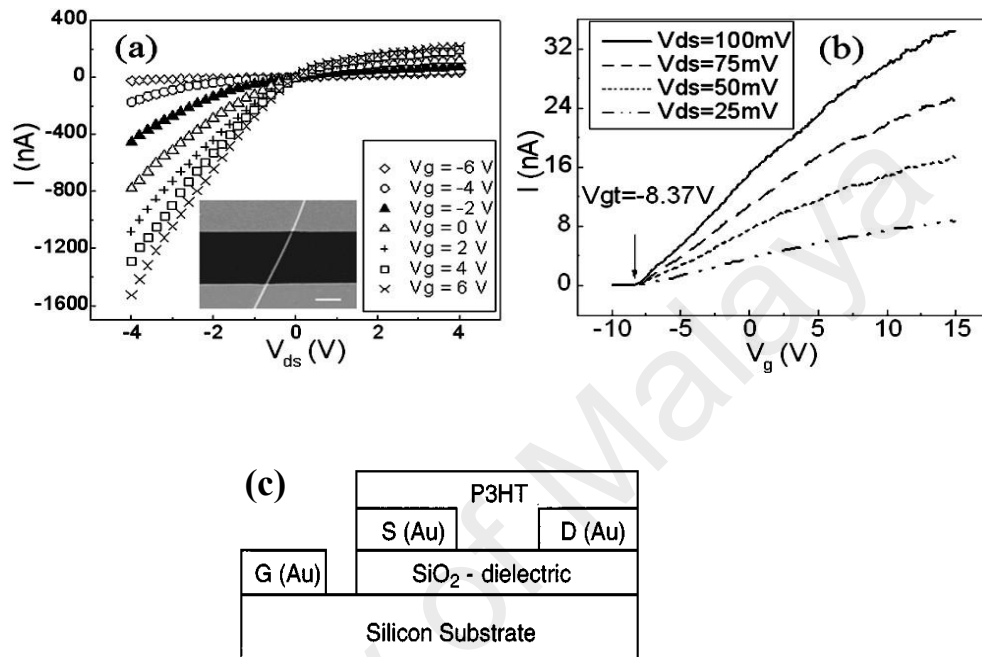


Figure 2.1: (a) Output and (b) Transfer characteristics of FET (Fan et al., 2004), and (c) FET structure (Bao et al., 1996).

2.3.1 Junction Field Effect Transistor (JFET)

In JFET, junction is defined as the boundary between the gate and channel. It has a channel that can be composed either n -type or p -type material. For n -type FET, electrons are its primary charge carriers while in p -type; the primary charge carriers are holes. Normally, in most conditions, p - n junction is set in reverse biased in order to ensure that the currents cannot be flow between the channel and gate. Its ability to operate in high temperature due to its operation supported by buried semiconductor junction instead of metal/semiconductor Schottky barrier. One of the effective JFET materials is based on inorganic semiconductor GaAs which it succeeded to function well from room temperature up to 400 $^{\circ}\text{C}$. Besides, GaN material also effective at high temperature in

debt to its large 3.42 eV band gap and high electron saturation velocity (Zolper, 1998).

Figure 2.2 portrays schematic and symbol of JFET.

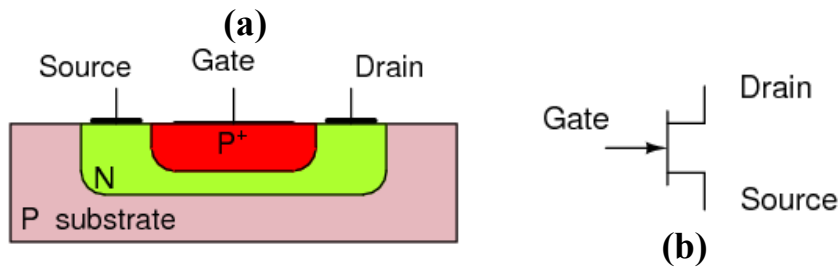


Figure 2.2: (a) Schematic diagram and (b) symbol of JFET ([https://www.allaboutcircuits.com/textbook/semiconductors/chpt-2/junction field/effect-transistors](https://www.allaboutcircuits.com/textbook/semiconductors/chpt-2/junction-field-effect-transistors)).

2.3.2 Metal Oxide Semiconductor Field Effect Transistor (MOSFET)

In MOSFET, the channel can also be either *n*-type or *p*-type with the gate consists of a piece of oxidized-surface metal. This layer will then act as a dielectric to ensure no current is flowing between the channel and gate during the signal cycle. This condition enables enormous input impedance produced by this type of FET. Robert Chau and his team utilized silicon semiconductor material in MOSFET and they obtained around 1.8 μA of output current at 1.4 V of V_{DS} (Chau et al., 2004). Figure 2.3 exhibits schematic diagram and symbol of MOSFET.

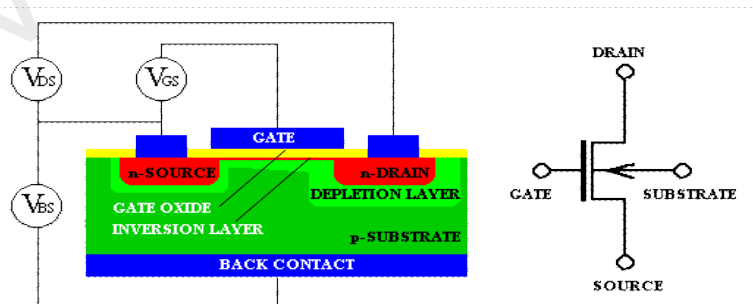


Figure 2.3: (a) Schematic diagram and (b) symbol of MOSFET (http://courses.egr.uh.edu/ECE/ECE4339/Class%20Notes/MOSFET_illustration.html).

2.4 Material for Organic Field Effect Transistor

Organic Field Effect Transistor (OFET) is a FET that utilizes organic material instead of inorganic material as the active layer or 'channel' in its operation. Dihexyl- α -pentathiophene and dihexyl- α -tetrathiophene are two organic materials that have been used as channel active layer in OFETs (Bao, 2000). In organic semiconductor material, interaction between molecules is mainly weak van der Waals attractions. This type of interaction will enable the realisation of special transport system which is intermediate between conventional low-mobility hopping in amorphous glasses (Davis & Mott, 1970) and high-mobility band transport in covalently bonded single-crystals (Sirringhaus, 2014). Apart from that, covalent bond also takes place inside the materials. This type of interaction is normally much stronger than other intramolecular interactions likewise van der Waals forces. Meanwhile intermolecular interactions' energy is much weaker than 40 kJ/mol as this interaction normally caused by the intramolecular interactions. Therefore, the much weaker intermolecular interaction energy will cause production of many states in the energy gap due to narrower transport band compared to inorganic material, which is easily broken by disorders (Małachowski & Żmija, 2010).

For comparison, in the inorganic semiconductors such as Silicon and Germanium, atoms are held together with very strong covalent bonds as high as 300 kJ/mol for Si. In these semiconductors, charge carriers move as highly delocalized plane waves and indicate a high mobility of charge carriers much larger than $1 \text{ cm}^2/\text{Vs}$ (Małachowski & Żmija, 2010). Organic semiconductor materials have disadvantages due to its weak interactions between its molecules which then will provide low charge carrier mobility. Besides, the doping process between semiconductor materials does not substitutional as in inorganic semiconductors (Natali et al., 2007).

However, organic semiconductor research field does counter its weaknesses by offering the introduction of new materials and with cheaper cost. Furthermore, this material then does enable the large-scale production for electronic appliances, in which environmentally friendly, flexible and light electronic devices can be guaranteed by applying organic semiconductor materials (Ben-Sasson et al., 2015). Development of organic electronics have adopted organic semiconducting material such as small molecule of VOPcPhO (Kamarundzaman et al., 2013; Makinuddin et al., 2015), conjugated polymer of PCDTBT (Bakar et al., 2014; Beaupré & Leclerc, 2013) and conjugated polymer of PFO-DBT (Fakir et al., 2014; Hou et al., 2006). However, for OFET applications, small molecules material often desired for their ability to arrange themselves nicely in solid state. This ability is due to their crystallinity. Subsequently, high charge-carrier mobility can be achieved as mainly intermolecular interactions are the main factor that affect the mobility (Allard et al., 2008).

In order to enhance the performance of OFET, many new semiconductor materials have been introduced hoping to have higher electron mobility to increase the output current in OFET. For instance, PDI-FCN2 films have been used in OFET to obtain the mobility of electrons of $0.1 \mu\text{cm}^2/\text{Vs}$ with 10^8 ON/OFF ratio (Jones et al., 2008). The other works done by Matthew and co. where they produced an OFET with electron mobility of $7.6 \mu\text{cm}^2/\text{Vs}$ and ON/OFF ratio of 10^5 (Durban et al., 2010) while Stefan et. al. had an OFET with electron mobility of $3 \times 10^{-4} \text{cm}^2/\text{Vs}$ with ON/OFF ratio of 10^3 by applying P3HT as semiconducting material (Gamerith et al., 2007). The other technique to enhance the electron mobility is by doping the semiconductor material likewise done by Yan and his research group where they doped P(NDI2OD-T2) and P3HT to obtain an OFET with electron mobility of around $0.45 - 0.85 \text{cm}^2/\text{Vs}$ with ON/OFF ratio of 10^4 (Yan et al., 2009). Lu and co. doped P3HT and PS materials to obtain an OFET with mobility of electron of $0.1 - 0.2 \text{cm}^2/\text{Vs}$ with ON/OFF ratio of $10^6 - 10^8$ (Lu et al., 2013).

2.4.1 Structures of Organic Field Effect Transistor

OFET primarily constructed based on the structure and principle of thin film transistor (TFT) where two basic constructions of the OFET whether gate at the top or gate at the bottom part of OFET (Allard et al., 2008). In this structure, the distance between drain and source (horizontally) does defined the channel length.

For the bottom-gate and top-contact (source and drain) structure arrangement, gate will be the second most bottom part of the structure as the most bottom part should be the substrates likewise glass or Indium Tin Oxide (ITO). This gate layer then sandwiched with the dielectric layer as the insulator, followed by semiconductor layer as the second uppermost layer and both source and drain will be on top of this structure with smaller sizes than underneath layers. However, the top-contact structure is often difficult to be made with organic FETs. Attachment of the electrodes is usually carried out thermally with metals and which could potentially damage the thin organic layers by diffusing metal atoms into the organic material. Therefore, researchers create another structure of bottom-gate and bottom-contact. In these structures, the substrate, gate and dielectric arranged accordingly form bottom to upper part. However, drain and source comes after dielectric layer instead of semiconductor layer. Hence, semiconductor layer will be placed on top of the structure.

Meanwhile for top-gate construction, the substrate will be the most bottom part followed by drain and source. Instead of dielectric layer, semiconductor layer comes first to accommodate these electrodes. On top of that, dielectric layer placed with the uppermost layer accommodated by gate. The top-gate configuration is favoured for printed transistors. Conducting polymers such as polyethylenedioxythiophene/poly(styrene sulfonic acid) (PEDOT/PSS) can function as electrodes in OFETs while insulating polymers such as polyvinylphenol (PVP),

poly(vinyl alcohol) (PVA), polyimide (PI) or poly(methyl methacrylate) (PMMA) are used as dielectric layer (Facchetti, 2007). Figure 2.4 (a-c) exhibit three types of OFET structure arrangements with the most well-known structure is top contact bottom gate structure. OFET by Yan and co. is an example of work applying top-contact bottom-gate OFET (Yan et al., 2009), while work done by Li et. al. and Hwang et. al. applying bottom-contact bottom-gate OFET and bottom-contact top-gate OFET, respectively (Hwang et al., 2011; Li et al., 2003).

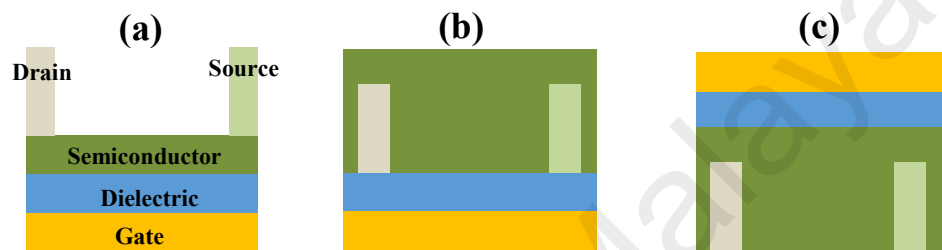


Figure 2.4: Three types of OFET structure arrangements of (a) top-contact bottom-gate OFET, (b) bottom-contact bottom-gate OFET and (c) bottom-contact top-gate OFET.

2.4.2 Mechanism of Organic Field Effect Transistor

Figure 2.5 (a) & (b) illustrate the operation of OFET. For *n*-type semiconductor application mechanism, as gate-source voltage is set on positive values ($V_{GS} > 0$ V), positive field of the gate electrode will be set to the top of this layer which is near dielectric layer. This action will attract negative field from dielectric layer to accumulate at bottom part of this layer while the other field will be at the upper part of dielectric layer which is near bottom part of semiconductor layer. Hence, negative field from semiconducting layer then focusing at bottom area of this layer while positive ones align at uppermost part of this layer. As applied drain-source voltage is positive ($V_{DS} > 0$ V), the electrons from the source will be attracted to the drain through the semiconductor layer. However, for the other operation, that is *p*-type semiconductor application, as V_{GS} is set up on negative values ($V_{GS} < 0$ V), the negative field will be at the bottom of gate electrode which is near the dielectric layer. This action will attract positive field from

dielectric layer to align at bottom part of this layer while the opposite field will be at the upper part of dielectric layer. Later, negative field from semiconducting layer then accumulate at bottom area of this layer while positive ones focus at uppermost part of it. When the drain-source voltage is applied at negative values ($V_{DS} < 0$ V), the positive charge carriers (hole) from source will move to drain electrode through the semiconductor layer (Facchetti, 2007). For the application of both negative V_{GS} and V_{DS} , the organic material is named as p -channel as holes are the majority and primary charge carriers. On the other hand, upon the application of positive V_{GS} and V_{DS} , electrons are the majority charge carrier and hence the semiconductor is said as n -channel.

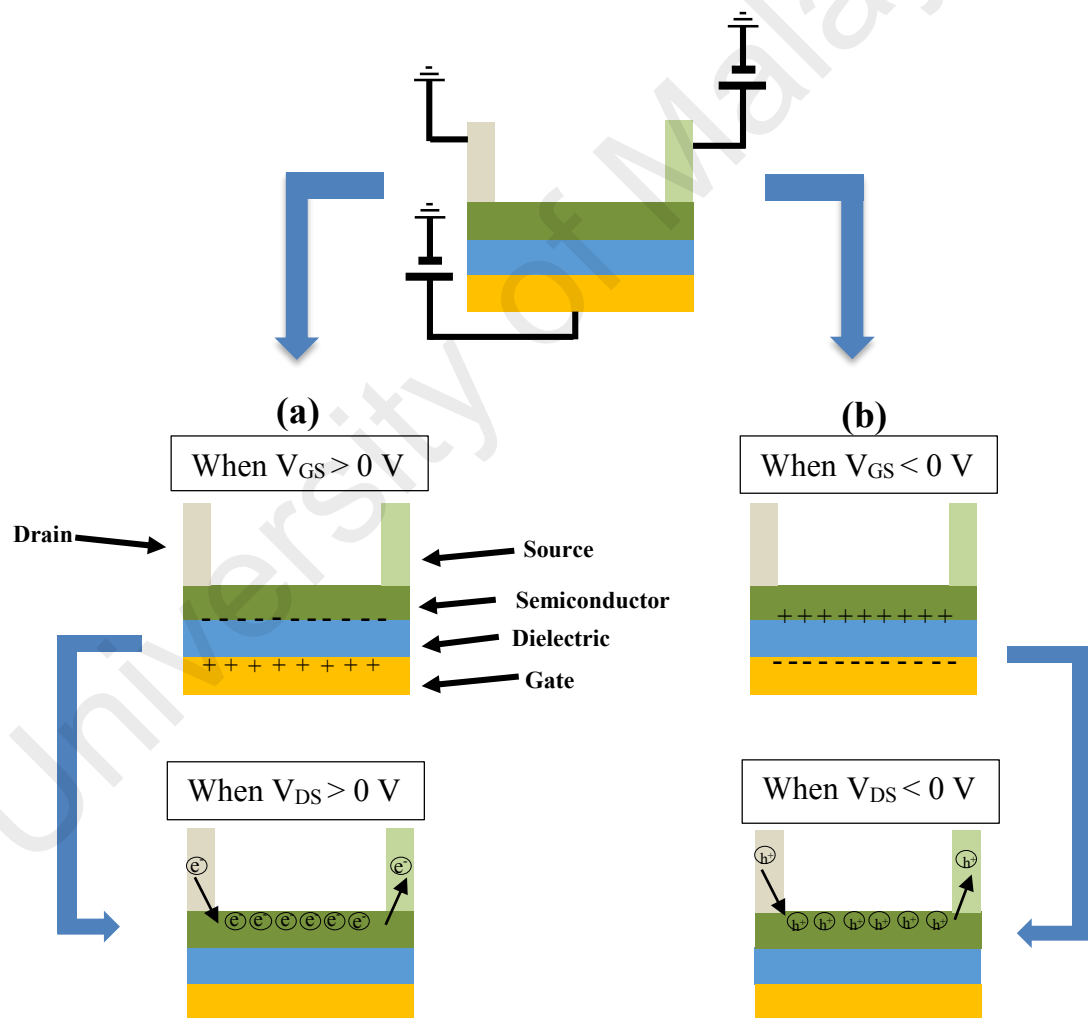


Figure 2.5: Operation mechanism of OFET for (a) n -type semiconductor and (b) p -type semiconductor (Facchetti, 2007).

2.5 Vertical Organic Field Effect Transistor

As discussed earlier, OFET does offer low charge carriers mobility and relatively higher turn on voltage compared to inorganic FET. The output current in conventional OFET is inversely proportional to channel length. By decreasing the channel length in OFET, one can effectively increase the output current even though the semiconductor material has low carrier mobility. Since it requires high cost to produce the short channel OFET, then moderate structural changes need to be made in order to achieve high output product with low turn on voltage. One of the famous structures is by applying vertical structure instead of typical horizontal OFET. With this structure, it is believed can improve the output currents by lowering the distance between drain and source electrode. Hence, as a result of this reduced channel length, it can operate at low-power consumption with drive high current densities. Therefore, these make it perfect for active matrix OLED pixels. The VOFET combines excellent performance (high output current, low-voltage, high frequency) together with easiness of fabrication (Ben-Sasson & Tessler, 2012).

Another absolute advantage of VOFET is that this device can be integrated with light emitting diode (LED) or other devices to produce the optoelectronic device namely VOLED with transparent electrodes on top-side or the bottom-side for light emission in and out of the devices (Yu et al., 2016). In the vertical channel structure, the channel length is defined by the source-drain distance which is perpendicular to the substrate. Thus, the channel length is actually the thickness of the thin film, which can be easily made in the nanometre scale. Basically, short length of channel can permit good performance of transistor since electron needs to cover much less distance despite the low carrier mobility of semiconductor material.

Figure 2.6 (a) & (b) illustrate the structural difference between conventional OFET and vertical OFET. Yang et. al (Ma & Yang, 2004) found the vertical structure in 2004.

Nowadays, Ben Sasson and co-workers is one of the most active researchers working on VOFET. To further enhance the performance of this novel OFET structure, patterned source electrode is formed by lithographic process to increase the probability of the charge carriers' accumulation before swept upwards to the drain electrode (Figure 2.7) (Ben-Sasson et al., 2013; Ben-Sasson et al., 2009). Application of silver nanowire is one of the other ways to form the perforated source electrode to achieve this target (Ben-Sasson et al., 2015).

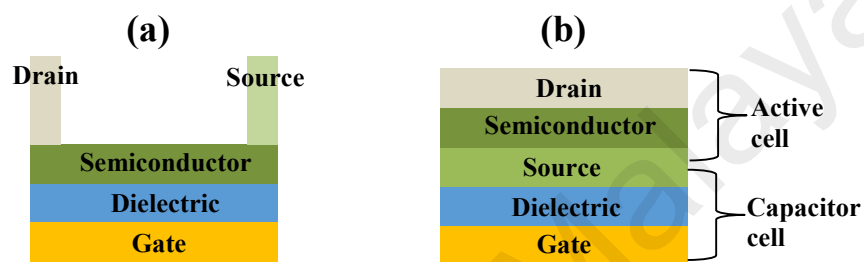


Figure 2.6: Structural difference between (a) lateral OFET or conventional FET and (b) vertical OFET.

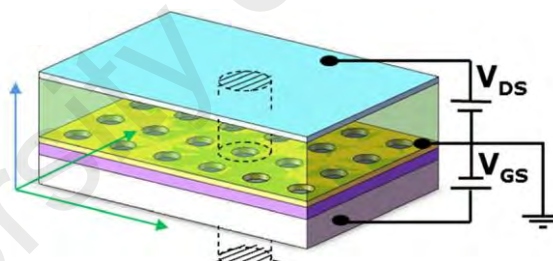


Figure 2.7: Patterned source electrode in VOFET as reported by Ben Sasson et.al, 2009.

2.5.1 Mechanism of Vertical Organic Field Effect Transistor

Operating mechanism of the VOFET must not be directly compared with the OFET's since the different current flow directions. The Schottky mechanism been a dominant role when the contact barrier height between the electrode and semiconductor material is much higher than 0.25 eV (Lin et al., 2015). There are two areas in the VOFET structure; that are capacitor cell and active cell regions. Capacitor cell area is from source electrode to the drain electrode while the active cell region commences from gate electrode to the

source electrode. Therefore, the source electrode is used as a common cathode for both cell. Hence, source electrode does control the injection of current for the active cell by tuning the electron injection from the source. This mechanism is similar to that of a Schottky barrier transistor (Ma & Yang, 2004) where source electrode and semiconducting material chosen must be from unequal energy level whenever at no bias at gate electrode. After bias from gate, electrons from source can jump over or channelling through the Schottky barrier to the semiconductor layer. Figure 2.8 illustrates the Schottky mechanism (a) before and (b) after gate bias.

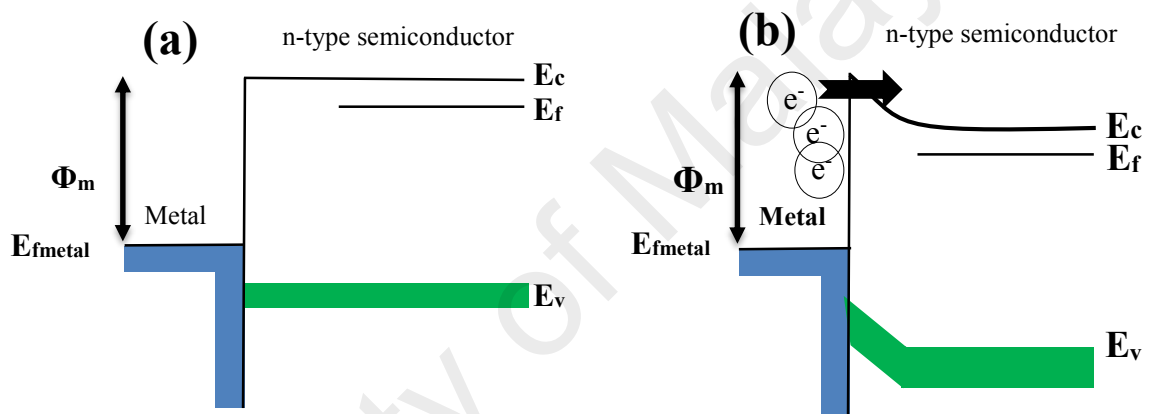


Figure 2.8: Schottky barrier mechanism at (a) no bias and (b) at positive gate bias for n -type semiconductor material where Φ_m = barrier height of metal, E_{fmetal} = Fermi energy of metal, E_c = conduction energy of semiconductor, E_f = Fermi energy of semiconductor and E_v = valence energy of semiconductor.

2.6 Anodic Aluminium Oxide (AAO) Template

Since the last 10 years, method to construct the promising porous template has been extensively studied in preparing the 1-D nanomaterial (Yuxiang Li et al., 2009). Anodized aluminium oxide (AAO) templates are the most extensively used porous membranes for almost uniform nanostructures whether nanotubes or nanowires synthesis (Hu et al., 2001; Kyotani et al., 1996; Li et al., 1999; Rahman & Yang, 2003; Routkevitch et al., 1996; Suh & Lee, 1999; Sui et al., 2001). Even nanorings and nanocones can be garnered from this template (Zhao et al., 2006). Since the studies by Masuda and Fukuda on the

self-ordered porous alumina membranes by a two-step replicating process (Masuda et al., 1995), AAO films have become one of the most prominent template materials for the preparation of nanostructured materials. This template is studied because of its ability to exhibit the excellent quality production and used in the fabrication of composite in nanoscale (Wang & Han, 2003). Template-assisted method could generate the low-cost nanofabrication technique, produce the high uniformity of nanomaterials and garner the high aspect ratio structure (Houng et al., 2014). Porous AAO template is widely used for replication by any materials especially the soft matter which in turn could be utilised in the fabrication of nanoscale devices (Wang & Han, 2003). Templating method is one of the affordable approaches and the easiest control process, which could result to the highly uniform pore diameter and size (Houng et al., 2014). When the aluminium is anodized, porous oxide film or barrier-type anodic film can be formed depending on the type of electrolyte (Li et al., 1998). They can be produced by anodizing pure Al in various acids which are sulphuric acid, phosphoric acid and oxalic acid (Diggle et al., 1969; Li et al., 1998; Masuda et al., 1998; Shen et al., 2013). Under different anodization conditions, mostly the AAO templates can have uniform hexagonal array of parallel and cylindrical channels meanwhile the pore diameters can be consistently varied from 10 to 200 nm (Shankar & Raychaudhuri, 2005). Anodic aluminium oxide (AAO) template has been studied due to its capability to garner high quality porous template and thus utilize in the fabrication of nanoscale device (Wang & Han, 2003). Templating technique is an affordable approach and easiest control process, which could result the high uniform pore diameter and high aspect ratio of pore size. It is well known that AAO template has ability to produce excellent quality of nanoscale fabrication with good uniformity, low cost and most importantly high aspect ratio of pores size over their length (Houng et al., 2014). However, in production of AAO template, there are presence of barrier layer at the bottom of the anodized aluminium layer which must be eliminated in purpose of

producing free standing nanostructures as done by researchers nowadays. Figure 2.9 (a) and (b) shows the schematic diagram and FESEM image of AAO template, respectively. Various anodization techniques are implemented including the two-steps technique that introduced by Masuda and Fukuda (Masuda & Fukuda, 1995). There are also works on the application of the four-steps anodization technique that separated by the three steps of oxide layer's removal (Hwang et al., 2002).

Glass and Indium Tin Oxide (ITO) is the common substrate used in anodization of aluminium layer (Houng et al., 2014). AAO templates can be synthesized on top of these substrates which prominent for the optoelectronic technology (Zhuo et al., 2011). Researchers have reported on the usage of ITO and glass as the substrate in producing the vertical standing nanorod arrays using DC magnetron sputtering technique of 200 nm (Houng et al., 2014) and 500 nm (Musselman et al., 2008) of aluminium layer thickness.

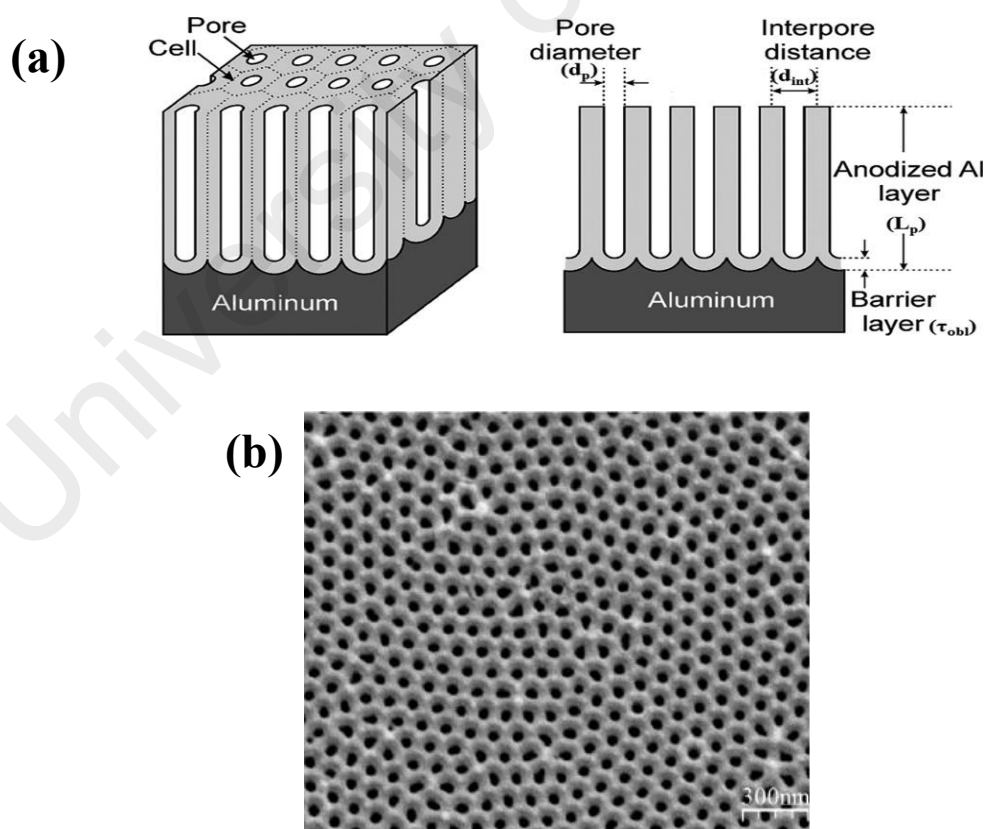


Figure 2.9: (a) Schematic diagram (Balde et al., 2015) and (b) FESEM image of an AAO template.

CHAPTER 3: MATERIALS AND EXPERIMENTAL PROCEDURES

3.1 Introduction

In this chapter, all of materials applied in this research presented with the procedures included to prepare or fabricate samples or layer by layer devices. The described procedures included are cleaning of substrates (glass or ITO), deposition of organic material as active material by spin coating method, deposition of inorganic material via thermal evaporation technique for electrode purpose and preparation of buffer layer. On top of that, descriptions on characterization method and equipment have been done in this chapter including Field Emission Scanning Electron Microscope (FESEM), Fourier Transform Infra-Red (FTIR), Ultra-Violet Visible Spectroscopy (UV-Vis), X-Ray Diffraction (XRD), Raman spectroscopy (RAMAN), Photoluminescence spectroscopy (PL), profilometer and I-V equipment. The detailed steps and the flow of the experiment are described concisely. Figure 3.1 below exhibit the flowchart in this work.

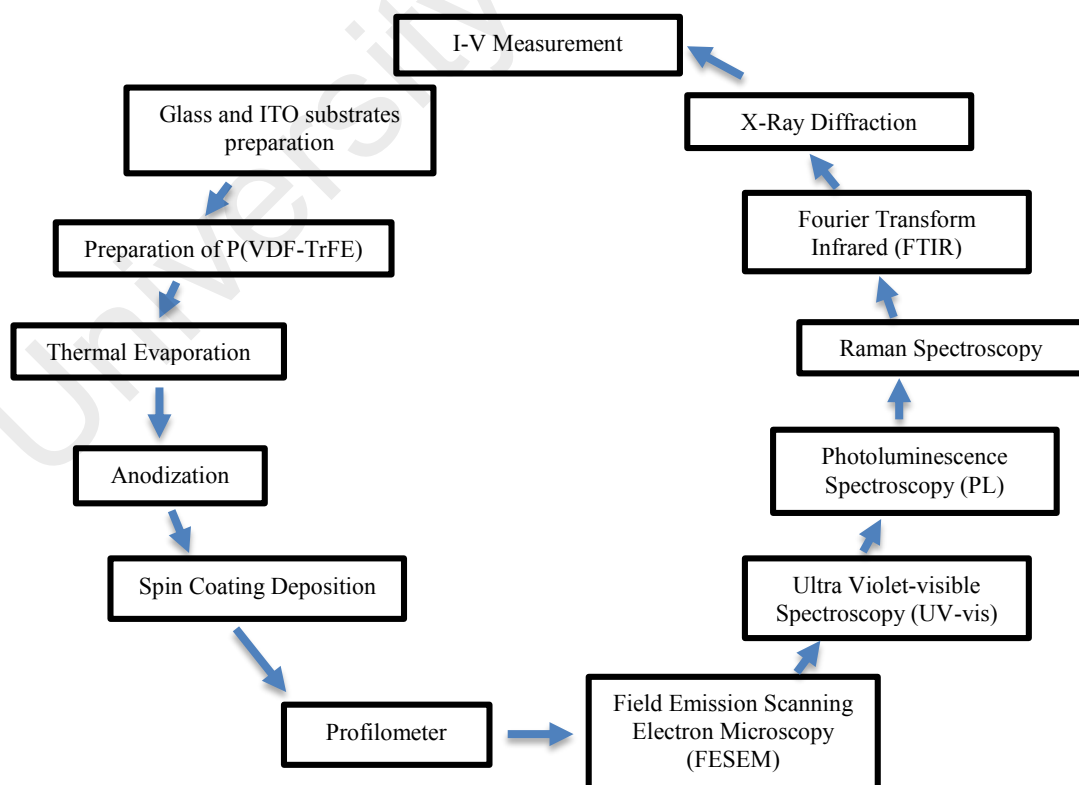


Figure 3.1: Flowcharts of research methodology.

3.2 Materials and Chemicals

3.2.1 P(VDF-TrFE)

Polyvinylidene fluoride-Trifluoroethylene P(VDF-TrFE) is a polymer that physically and chemically stable with good flexibility (Tashiro, 1995). It is a crystalline polymer and has ferroelectric properties which is due to the huge difference in electronegativity between hydrogen, fluorine, carbon with Pauling's values of 2.1, 4.0, 2.5, respectively (Pauling, 1960). Its Curie temperature is above melting temperature of 195 – 197 °C. Addition of P(TrFE) into the PVDF does aid in transiting its phase transition by modifying the PVDF crystal structure. It is done by enhancing interplanar distance with the unit cell size of the ferroelectric phase (Tashiro, 1995). In form of packed copolymer chains, there would be phase- β , phase- α , phase- γ and phase- δ crystalline phases (Xu et al., 2000). Phase- β is the only one polar phase that contains enormous spontaneous polarization which perpendicular to the polymer chain direction (c-axis) and along the b-axis which is positioned parallel to the C-F dipole moment (Hu et al., 2009). The (a) molecular structure and (b) visual image of P(VDF-TrFE) is shown in Figure 3.2. This material used in this work is in ratio PVDF:TrFE of 75:25 with density of 0.805 gml⁻¹ from Kureha brand, Japan was purchased and used without further purification.

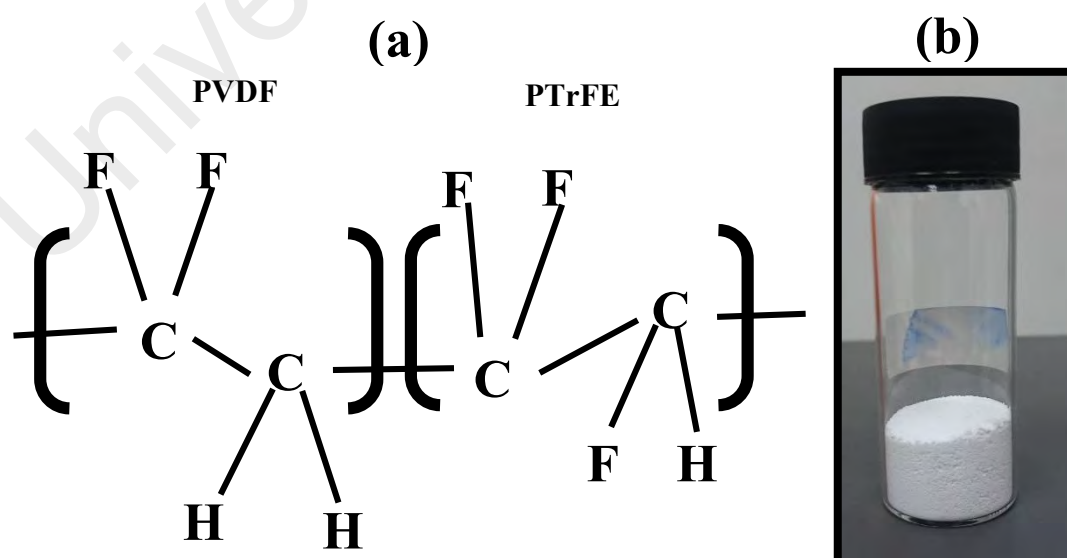


Figure 3.2: (a) Chemical structure and (b) visual image of P(VDF-TrFE).

3.2.2 MEK

Methyl Ethyl Ketone (MEK) also referred as 2-butanone, is a solvent used throughout this work to dissolve P(VDF-TrFE). It has electron configuration of $\text{CH}_3\text{C}(\text{O})\text{CH}_2\text{CH}_3$. Usually, MEK is used as solvent in processing the cellulose nitrite, cellulose acetate, resins and gums. Besides, it also used in synthetic rubber industry, to remove glues. This solvent is easily dissolved in water and has colourless appearance. It is a volatile liquid and therefore has reactivity properties. The chemical formula for MEK is $\text{C}_4\text{H}_8\text{O}$ as in Figure 3.3 (a) and its molecular weight is ~ 72.10 g/mol. Figure 3.3 (b) shows the visual image of MEK solution. MEK has sweet odour reminiscent of butterscotch and acetone. It can be found in small amount in nature and mainly synthesized industrially with huge-scale. Short-term exposure or inhalation to MEK results in irritation to the throat, nose and eyes. In this work, MEK is obtained from Merck brand, Germany.

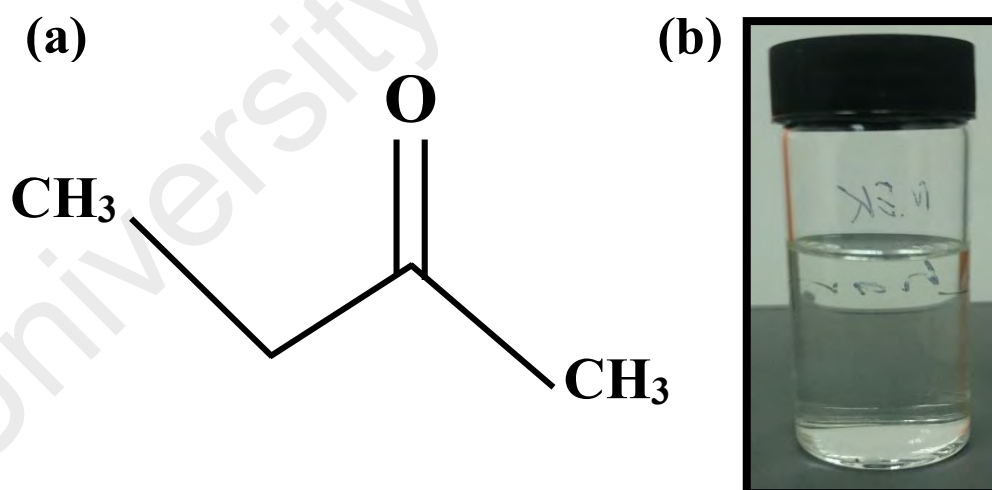


Figure 3.3: (a) Chemical structure of MEK and (b) visual image of MEK.

3.2.3 VOPcPhO

Vanadyl 2, 9, 16, 23-tetraphenoxy- 29H, 31H-phthalocyanine (VOPcPhO) is a semiconducting organic that has been widely studied in solar cells, humidity sensor and photodetector (Abdullah et al., 2012; Azmer et al., 2016; Zafar et al., 2014). It is popular due to its excellence in semiconductivity, high thermal stabilities and photoconductivity (Kamarundzaman et al., 2013). Thus, it is suitable to be used as an organic layer in the vertical OFETs. It has conjugated π -electron system which can aid the delocalization of orbital wavefunctions. Therefore, electron withdrawing groups or donating groups can be attached to this material to facilitate hole or electron transport. This material purchased from Sigma Aldrich brand, USA in dark green powder form with molecular weight of 947.85 g/mole. The molecular structure and visual image of VOPcPhO is shown in Figure 3.4 (a) & (b), respectively. In this work, VOPcPhO with 10 mg/ml of concentration is prepared by dissolving it in chloroform. VOPcPhO will then spin coated onto the sample with spin rate of 4000 rpm.

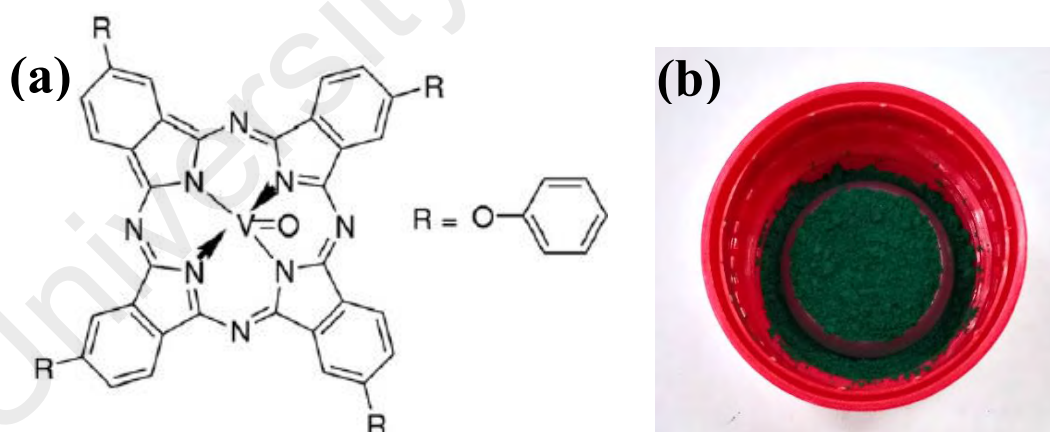


Figure 3.4: (a) Chemical structure (Abdullah et al., 2012) and (b) visual image of VOPcPhO.

3.2.4 Chloroform

In this work, chloroform is used as a solvent to dissolve VOPcPhO. It is obtained from Eriendemann Schmidt brand, Germany with molecular weight of 119.38 g/mol. Chloroform is colourless and has volatile properties yet non-flammable. It has chemical configuration of CHCl_3 . Besides, it has an ether-like smell and is a derivative in liquid form of the trichloromethane. Acute exposure or inhalation to human could cause cardiac arrhythmia, nausea, liver function problem and central nervous system dysfunctional problems. This material often applied as the solvent for oils, fats, wax, rubbers and resins. Besides, it also used as cleansing agents and in fire extinguisher. The molecular structure and visual image of chloroform is as in Figure 3.5.

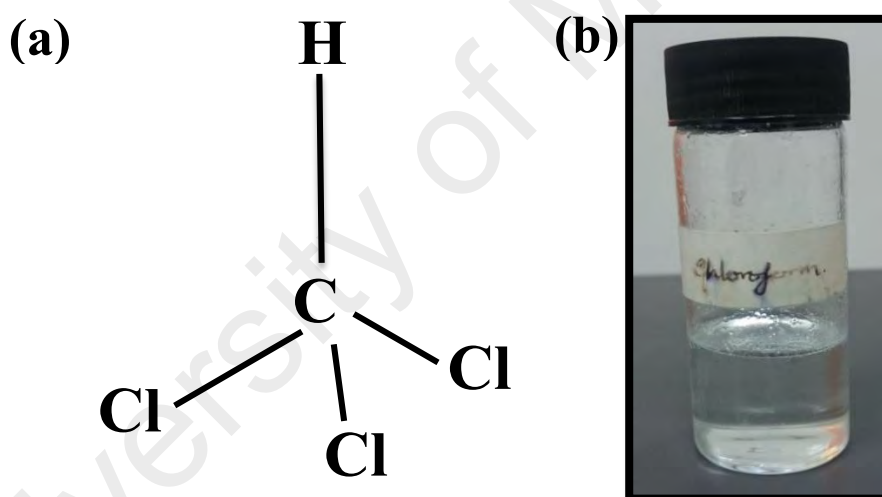


Figure 3.5: (a) Chemical structure and (b) visual image of chloroform.

3.2.5 Isopropanol Alcohol

Isopropanol Alcohol (IPA), or 2-propanol is a solvent that used to dissolve the silver nanowire throughout this experiment that obtained from System brand, Malaysia. It has electron configuration of $(\text{CH}_3)_2\text{CHOH}$ with a colourless appearance that is miscible with water. Its boiling points and melting points are 82.3 °C and -89 °C, respectively. This alcohol is one of the cheapest alcohols worldwide and therefore often applied as solvent

to replace ethanol since they share the similar solvent properties. Exposure or inhalation to this solvent could result in moderate irritation of the eyes, nose and throat while oral exposure could cause moderate to severe dizziness and headache. IPA is made by dissolving the propylene gas in sulphuric acid. Then, by hydrolysing the formed sulphate ester, IPA can be extracted. Formerly, it was obtained by catalytic reduction of acetone. The chemical structure and visual image of IPA is shown in Figure 3.6 (a) & (b), respectively.

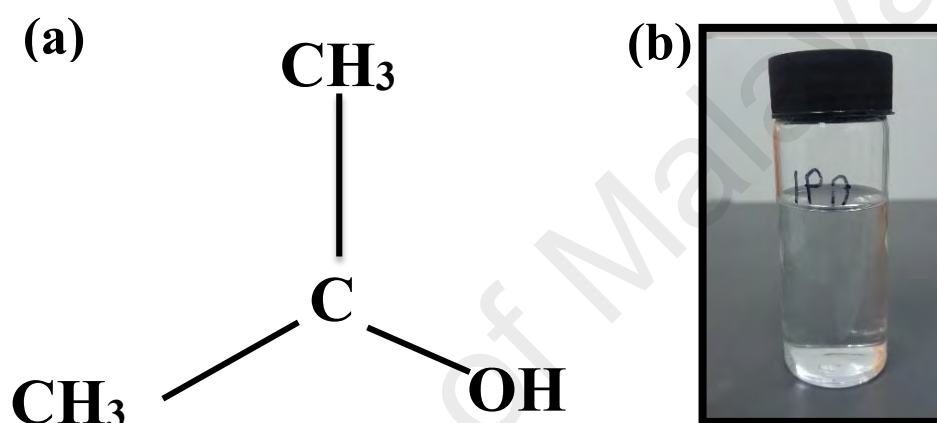


Figure 3.6: (a) Chemical structure and (b) visual image of IPA.

3.2.6 Anodic Aluminium Oxide (AAO)

AAO template is hugely studied and utilized for its capability in replicating the composite in nanoscale for its ability to garner the high quality nanochannel (Drury et al., 2007). It is recognized that AAO template can produce relatively cheaper nanoscale fabrication with production of highly uniform nanoscale (Houng et al., 2014). AAO template is commercially available. However, the commercial template does not attach to any substrate. Hence, it may have two holes; top hole and bottom hole. In our work, the template is a homemade-type template synthesised by anodization procedure. This homemade template can be attached to the desired substrates. The thickness of the template can be varied from 100 nm up to the micron scale. The cross-sectional view

FESEM image of AAO template is shown in Figure 3.7 (a) & (b) exhibits the top-view FESEM of AAO template.

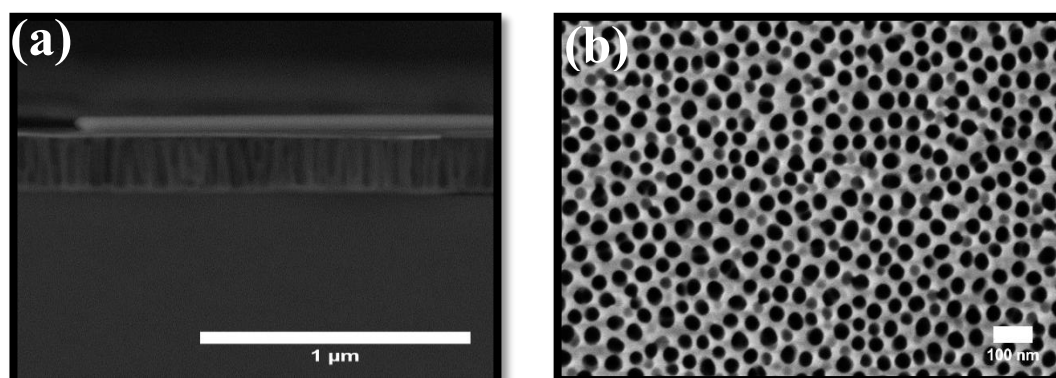


Figure 3.7: (a) Cross-sectional and (b) top-view FESEM images of AAO template.

3.2.7 Silver Nanowire

Nanostructured electrode such as silver nanowire has the probability to generate low sheet resistance and thus, low operational voltage. Silver nanowires have been given the full attention because of well-known excellent properties of electrical, optical and thermal (Yugang Sun, 2010). Silver nanowire films are highly transparent with diffusive transmittance at around 95 % at a wavelength of 550 nm. Besides, it is very conductive with sheet resistance at $\sim 10 \Omega/\text{sq}$ and can exhibit higher flexible (Song et al., 2013). Thus, this nanowire was applied as source electrode in our work with 0.5 % in isopropanol (IPA) spin coated on top of the prepared sample. Silver nanowire with length of 1.8 μm and diameter of 30 nm is obtained from ACS Material brand (USA). Figure 3.8 (a) & (b) exhibit the FESEM image of silver nanowire and its visual image, respectively.

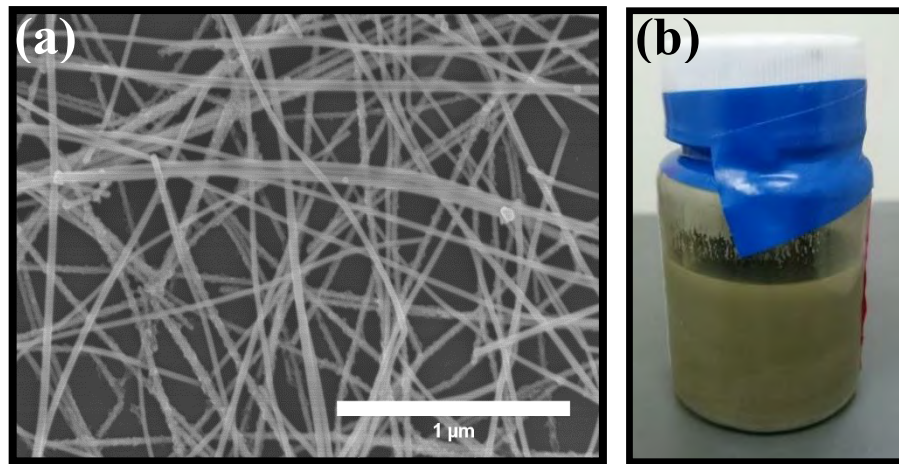


Figure 3.8: (a) FESEM image of silver nanowire and (b) visual image of silver nanowire in IPA solvent.

3.3 Fabrication Techniques

3.3.1 Substrates Cleaning Process

Prior to the preparation of sample, substrates were firstly cleaned with liquid soap and then placed in the ultrasonic cleaner for 15 minutes. Later, it rinsed in distilled water after it cleaned in acetone and ethanol. For the drying process, they were placed in the oven where the temperature is set to 100 °C for 10 minutes. These steps are crucial in order to eliminate all impurities and tiny dirt such as dust or grease that most probably avail on the commercial substrates. These impurities could potentially affect the performance of samples and materials.

3.3.2 Preparation of P(VDF-TrFE) Process

MEK was used as solvent to dissolve the P(VDF-TrFE) which was fixed at 5 wt. % concentration. Sample was stirred for an hour at 1000 rpm of 90 °C. Later, sample was spin coated onto substrates i.e. glass or Indium Tin Oxide (ITO) for 30 s. Annealing was then done at 100 °C for 1 hour in order to increase the crystallinity of copolymer. Finally,

drying process was done at 70 °C overnight to ensure no vapour presence. Figure 3.9 exhibits the preparation of P(VDF-TrFE).

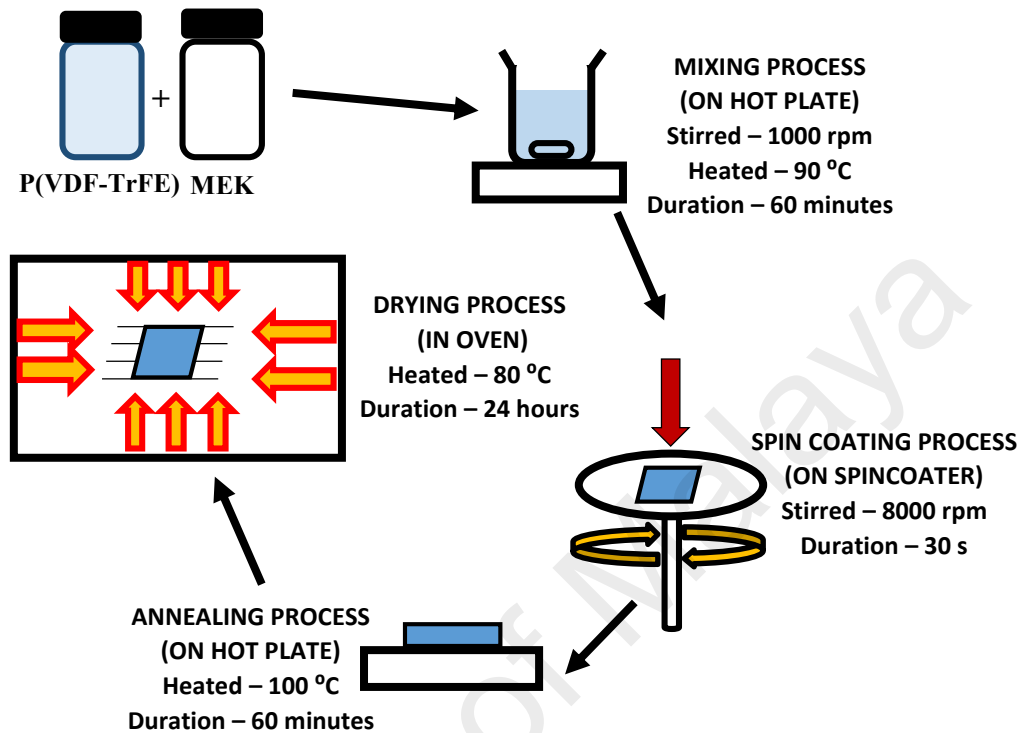


Figure 3.9: Schematic diagram of preparation of P(VDF-TrFE).

3.3.3 Thermal Evaporation Process

After PVDF-TrFE is dried, this sample will undergo aluminium evaporation process using the Auto-Edward 306 (Edwards, UK) thermal evaporator as shown in Figure 3.10 (a) with its cross section illustrated in Figure 3.10 (b). 8-10 pieces of aluminium wires (99.99% pure) were attached to tungsten coil and placed inside the thermal evaporator. Sealing process was done until the air pressure exerted inside the chamber reached to 1.00×10^{-5} mbar. During the evaporation process, aluminium was burnt slowly with 24 V of constant voltage. The current supplied to aluminium will provide energy to electrons in aluminium to collide and change its form into heat that dissipated from the evaporation process. Thickness of 100 nm aluminium thin films was coated on top of the sample.

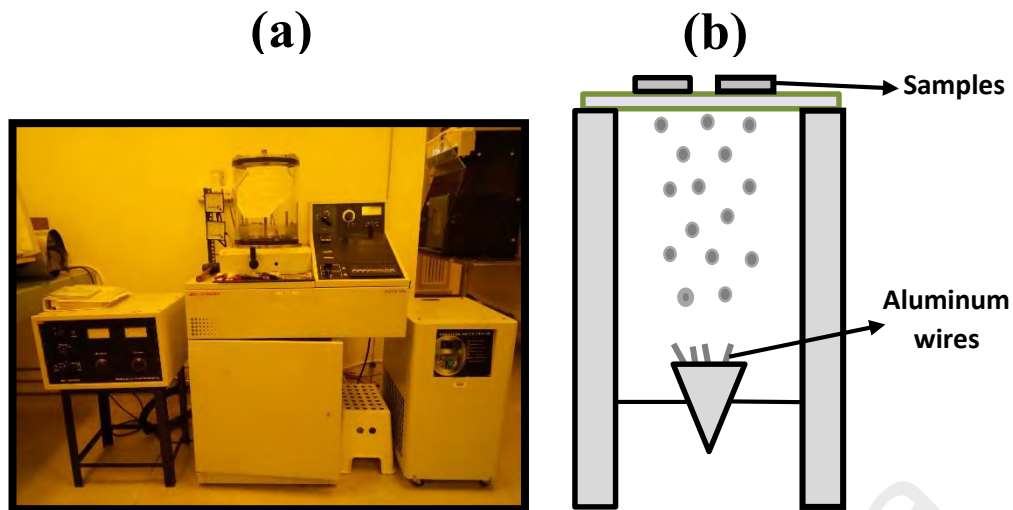


Figure 3.10: (a) Thermal evaporator Auto-Edward 306 and (b) Schematic diagram of thermal evaporator during aluminium coating process.

3.3.4 Anodization Process

To construct anodic aluminium oxide (AAO) template, one-step anodization process was applied with constant voltage of 25 V supplied. Then, pore enlargement method was conducted to garner the admired pore sizes (Figure 3.11 (a) & (b)). At 10 °C temperature, anodization process was done in 0.3 M sulphuric acid (Sigma Aldrich, USA) (electrolyte) which was placed in the water bath. Sample and platinum mesh placed as anode and counter electrode, respectively. Anodization was performed in Protech model 631D (Protech, USA) water bath (Figure 3.12 (a) & (b)). For pore widening process, the anodized samples that has undergone 100 rpm of stirring speed were then immersed in 0, 5 and 10 % phosphoric acid (Sigma Aldrich, USA) for 15 mins at temperature of 30 °C.

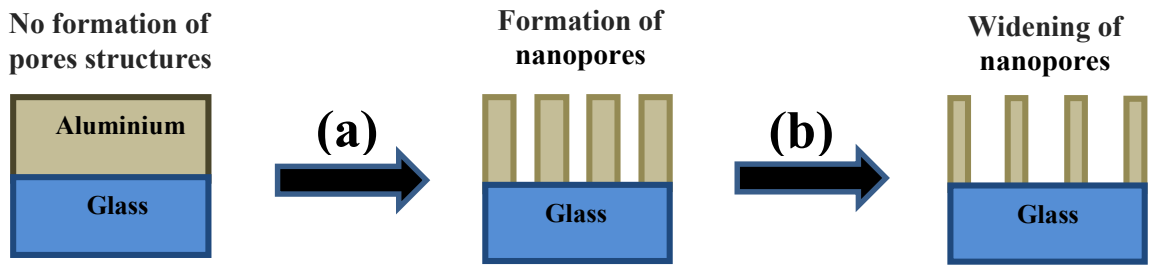


Figure 3.11: Schematic diagram of (a) anodization process from aluminium thin film to porous alumina and (b) pore widening process.

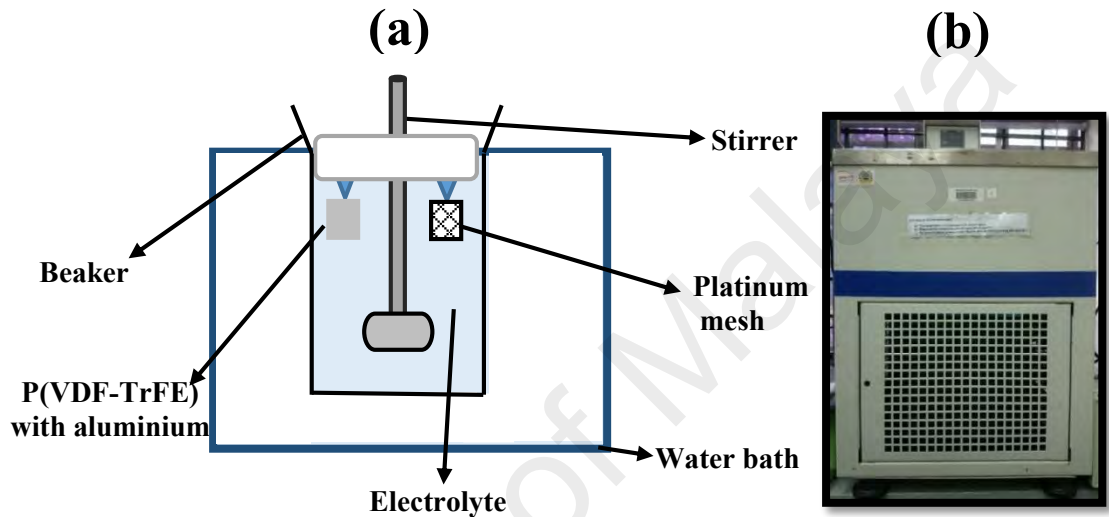


Figure 3.12: (a) Schematic diagram of anodization process and (b) Protech model 631D water bath.

3.3.5 Spin Coating Deposition Process

Spin coating deposition is the common technique to deposit thin film organic materials. In this technique, nitrogen gas is needed to suck the substrate/sample on top of the spin coater so that it static during spinning process (Figure 3.13 (a)). By using this method, the speed of the spin (8000 rpm for P(VDF-TrFE) and 4000 rpm for VOPcPhO), acceleration in rpm and duration in seconds (30 s for both P(VDF-TrFE) and VOPcPhO) can be set. During the spinning process, ones can deposit the solution material on top of the other prepared substrate/sample. Theoretically, the higher the spin rate, the thinner the sample would be produced. However, this theory may not imply to all type of organic

materials. Spin coater model Laurell P6000 (Laurell, USA) is used in this study (Figure 3.13 (b)).

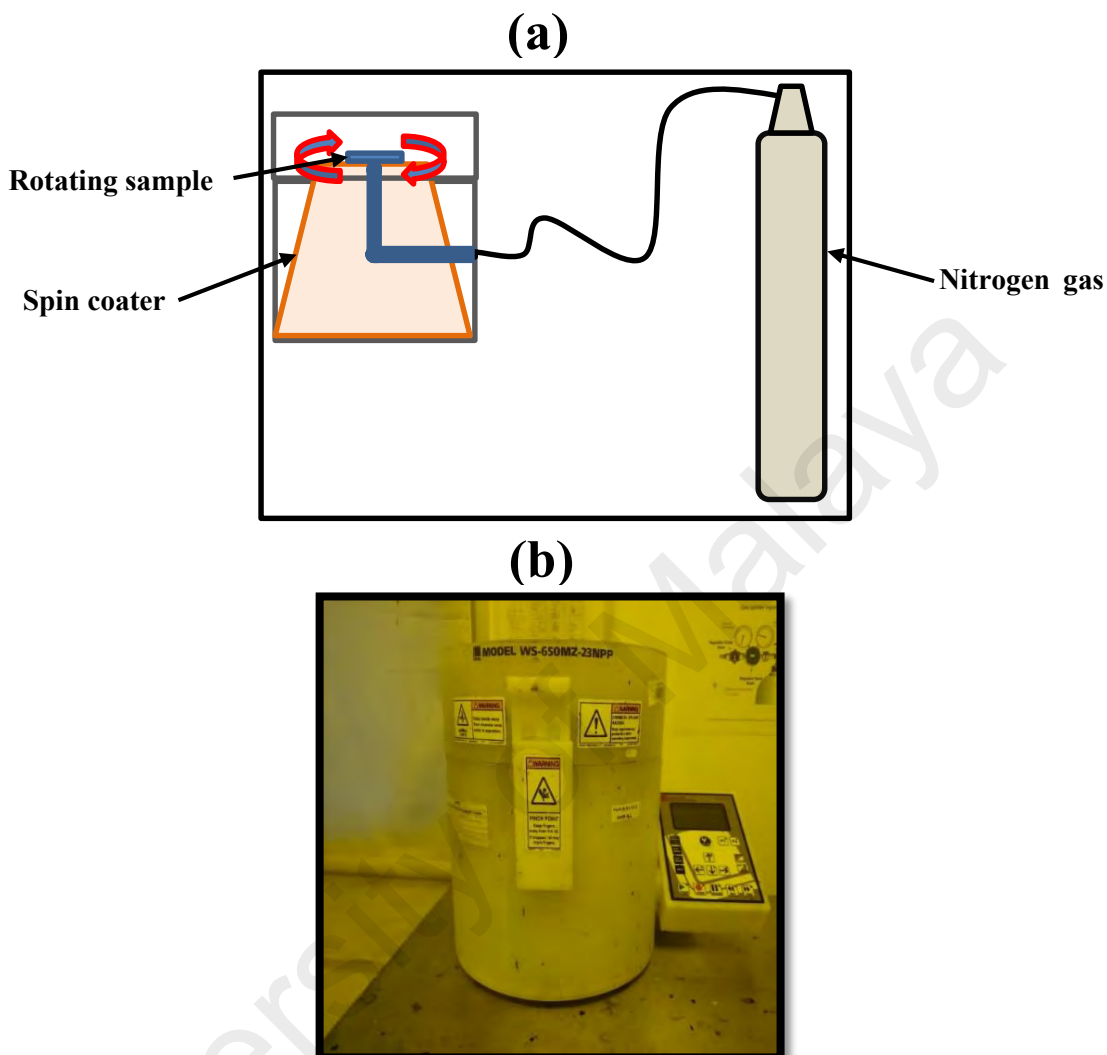


Figure 3.13: (a) Schematic diagram of spin coating method during spinning process and (b) Laurell P6000 spin coater.

3.4 Measurements and Characterisations

3.4.1 Morphological Analysis

The morphological and structural studies are important in this work, as these studies could provide information of the basic structure of produced templates. Field Emission Scanning Electron Microscopy (FESEM) does provide morphological properties of samples with about 10 to 300,000 times magnification. In this study, JSM 7600-F

FESEM-EDX (Jeol, Japan) model is used (Visual image in Figure 3.14(a) with schematic diagram in Figure 3.14(b)). FESEM produces a clearer and less electro-statistical distorted images compared to conventional SEM. In addition, it offers spatial resolution with three to six times better. Releasing electrons from field emitter source does the scanning operation. There are two anodes available for electrostatic focusing purpose. The first anode with field emission tip function to controls the current emission (1 ~ 20 μA) by controlling the extraction voltage. The second anode together with cathode work together to increase the beam energy to tune the electrons' velocity. This voltage combined with the beam diameter determines the resolution. The higher the voltage applied, better resolution can be achieved. Condenser functions to condense the beam diameter to make it smaller than feature in order to resolve a feature on the specimen surface. Then, these electrons will pass through electromagnetic lenses to assist in the condensation of the beam. Soon, they will be focused to sample by objective lens and deflected by deflection coil and this deflection action later will produce narrow scan beam through continuous bombardment onto the sample. Thus, this action produced secondary electrons emission from the bombarded sample and a photo sensor will detect the emitted secondary electrons. These steps enable the topological surface imaging of the sample surface to be shaped nicely. Besides, it has the ability to examine smaller area spot at electron accelerating voltages that are compatible with energy dispersive spectroscopy (EDS). Therefore, this ability enables users to determine the elements that exist on the sample. In this work, the samples were coated with platinum before being placed onto sample holders to be analysed by the equipment.

(a)



(b)

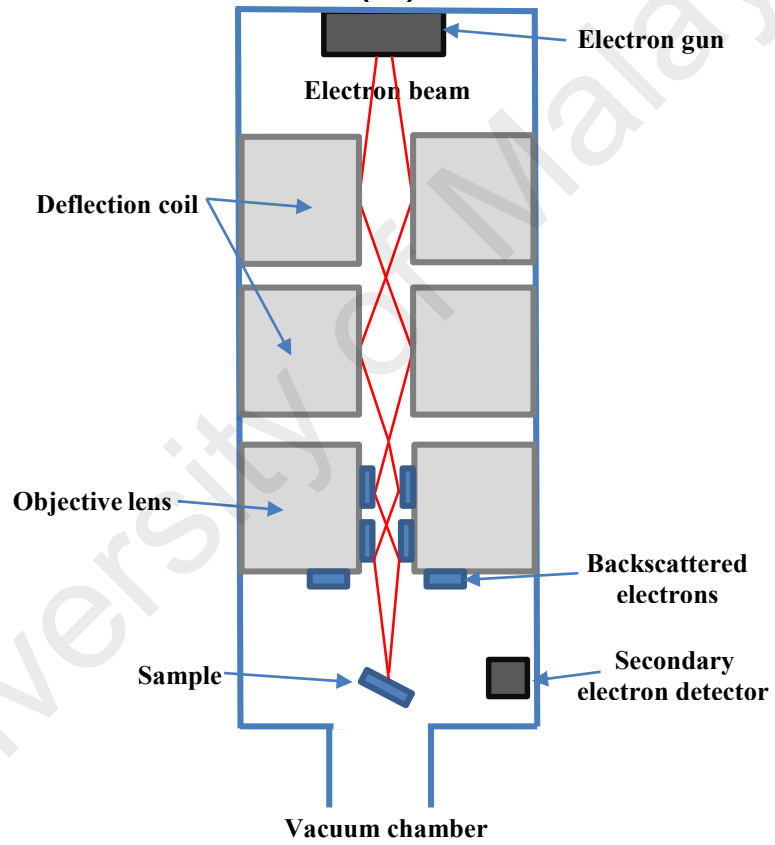


Figure 3.14: (a) Visual image and (b) schematic diagram of JSM 7600-F FESEM-EDX.

3.4.2 Phase Analysis

For phase identification, X-Ray Diffraction (XRD) is a technique used to identify phases of a crystalline material. It can provide data of unit cell dimensions. In this work, XRD was used to prove that P(VDF-TrFE) could undergo anodization process without having to lose its important properties which is polar β -phase. XRD consists of mainly three basic components, which are X-ray detector, X-ray tube and sample holder. Function of cathode ray tube is to produce X-rays by heating the filament to produce electrons. By applying the voltage, these electrons will be accelerated through the ray tubes towards sample. X-ray spectra will be produced and the specific wavelengths at the spectra are the characteristic of the target materials. To generate monochromatic X-ray for diffraction process, crystal monochromator or foil filtering will be needed. These X-rays are directed towards the sample. Intensity of the X-rays that are reflected are recorded as detector and sample are rotated. Constructive interference occurs and produced the peak in intensity as Bragg equation satisfied by the geometry of the incoming X-rays that directed towards the sample. These peaks later recorded by a dedicated detector and they then processed to be converted into count rate. Figure 3.15 (a) shows the image of the SU 8000 XRD (Skyray, USA) while Figure 3.15 (b) shows its schematic diagram. In this work, range of 2θ used is from 10 to 80 with K-alpha radiation of 1.54 Å wavelength.

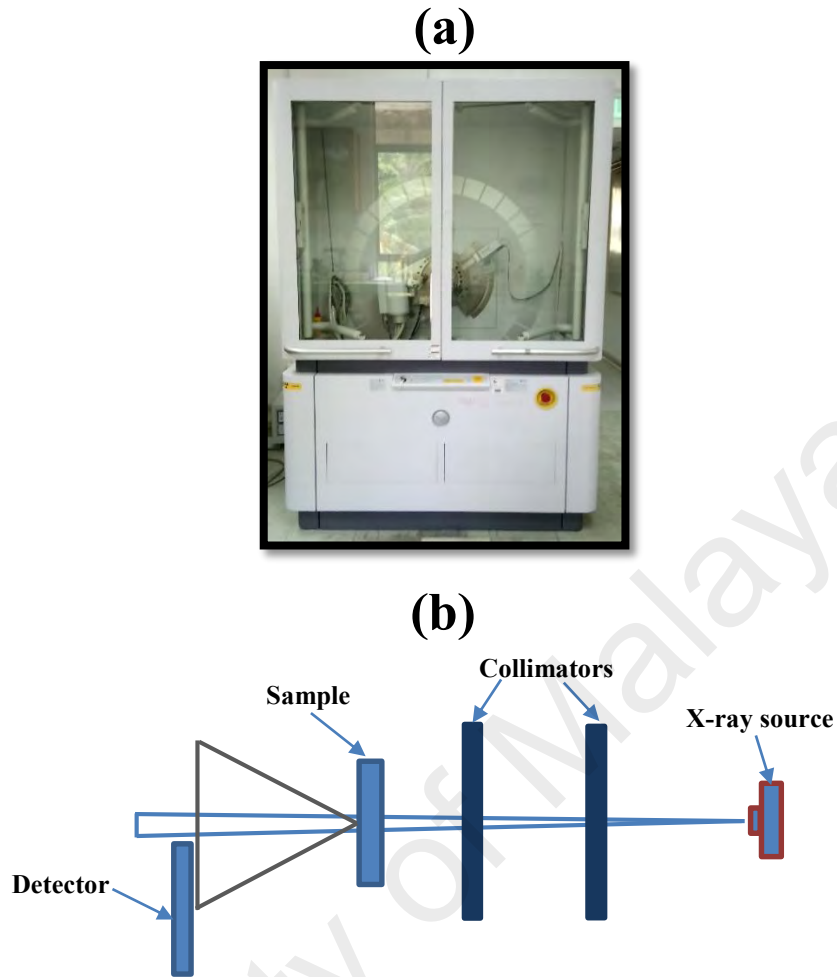


Figure 3.15: (a) Visual image and (b) schematic diagram of SU 8000 XRD.

3.4.3 Bonding Analysis

For bonding study, Fourier Transform Infrared (FTIR) is applied to study the bonding that obtained in P(VDF-TrFE) before and after the anodization process. In FTIR mechanism, infrared radiation emitted from a blackbody source collimated and will pass through the sample. Ideally half of the intensity of the light refracted to the stationary mirror while the other half should be channelled towards the movable mirror. Then, light is reflected back to the beam splitter from these mirrors and fractions of the original light passes into the sample. Before leaving the sample, light then focused to the detector. These beams will then be passed to detector for measurement. The detector is specially designed so that it could measure the interferogram signal. Spectra that produced will

represent the absorption and transmission of molecules and thus generating molecular fingerprint of the sample. This method could identify unknown materials by identifying the elements in a mixture. In this measurement, a measurement of background spectrum is a must in order to generate a relative scale for the absorption intensity. Figure 3.16 (a) shows the image of Nicolet i10 FTIR (Thermo Fisher, USA) while Figure 3.16 (b) shows its schematic diagram. In this work, no special treatment is needed for the sample before its being placed into sample holder for analysis. The wavenumber applied in this study is $0 - 4000 \text{ cm}^{-1}$.

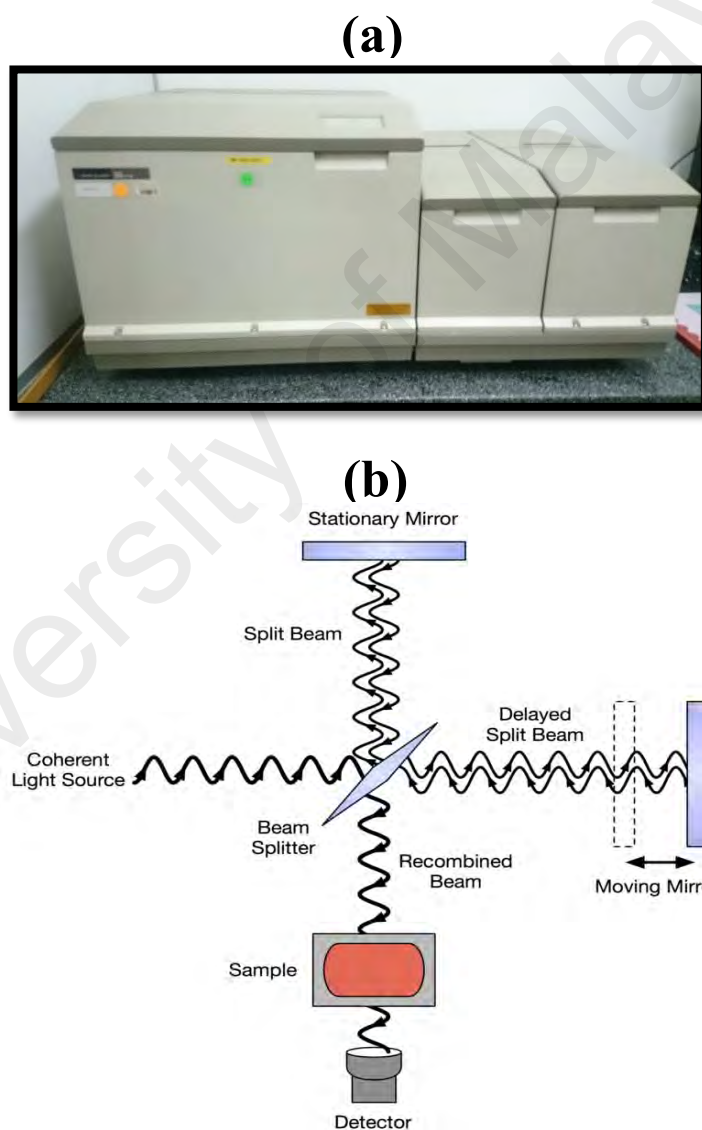


Figure 3.16: (a) Visual image and (b) schematic diagram of Nicolet i10 FTIR.

3.4.4 Optical Properties Analysis

3.4.4.1 Ultra Violet-visible Spectroscopy (UV-vis)

For optical study, UV-vis spectroscopy is important and crucial for researcher to study the optical properties of a material. UV-vis spectroscopy works by separating beam of light from UV or visible light source into their components wavelengths by using a prism. These monochromatic wavelengths will further split up into two same intensity beams. These smaller beams later will be channelled to each reference sample and sample that being studied. To compare the intensity of two beams, detector was used for measurement. These two intensities are referred to I_0 (reference) and I (sample). If the studied sample is able to absorb light, its intensity I would be less than I_0 . If the sample does not absorb any light, then its intensity would be I_0 . The difference between these intensities was plotted as graph (intensity versus wavelength). Absorbance is presented as $[A = \log \frac{I_0}{I}]$ while transmittance is $[T = \frac{I}{I_0}]$. Figure 3.17 (a) exhibits the visual image of model Lambda 750 (Perkin Elmer, UK) UV-vis equipment while Figure 3.17 (b) exhibits its schematic diagram. The range of wavelength used is between 400 – 1200 nm for transmittance study while 400 – 800 nm for absorption study.

(a)

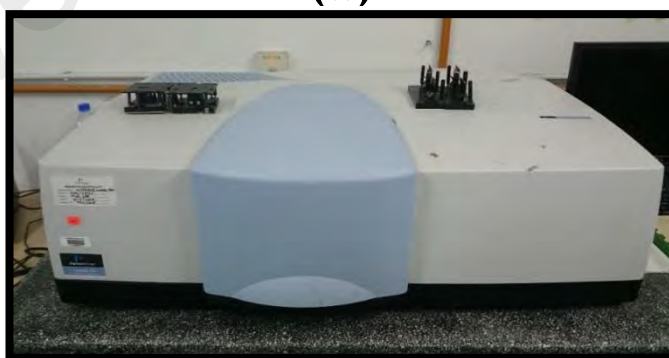


Figure 3.17: (a) Visual image and (b) schematic diagram of Lambda 750 UV-Vis spectroscopy.

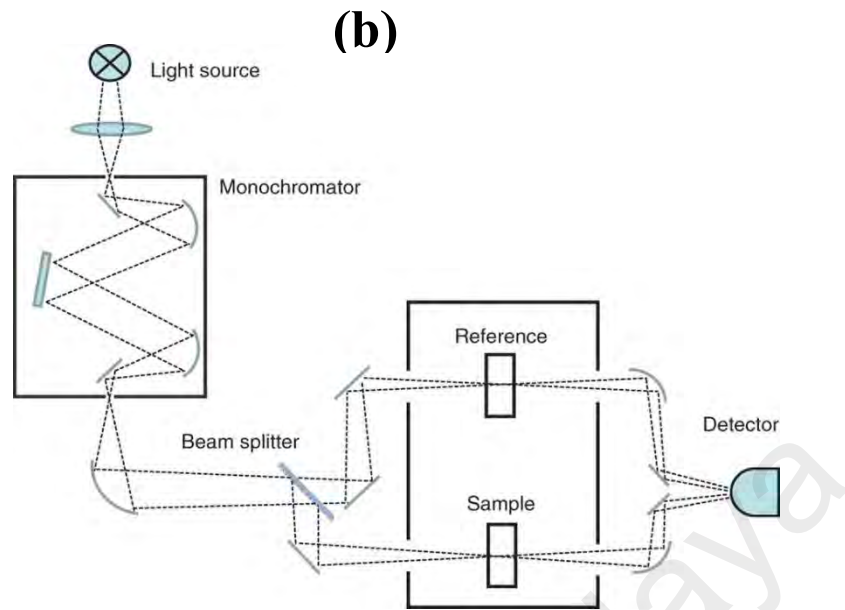


Figure 3.17, continued.

3.4.4.2 Photoluminescence (PL) Spectroscopy

Photoluminescence (PL) spectroscopy is another technique to determine the optical properties of material. PL can be used to study crystal defects and this is importance for materials like diamond and silicon carbide (SiC). PL comprises fluorescence process and originates from an absorption/emission process between different electron energy levels in the studied material. Basically, PL instigated by the excitation of photons and emission of light of any forms of matter. An electron that has been excited above the conduction band of a material will eventually fall and recombine to the hole that has been excited below the valance band after losing some energy through releasing a phonon to the lowest available non-radiative energy level. Relaxation process occurs when photon is reradiated. The type of PL selection does heavily depend on material studied and laser wavelength chosen. Usually, by choosing appropriate laser wavelength, ones can eliminate unwanted fluorescence and interference can be avoided by choosing an appropriate laser wavelength since PL bands are strong and broad. Figure 3.18 (a) shows the image of Renishaw PL (Renishaw, UK) spectroscopy while Figure 3.18 (b) exhibits

its schematic diagram. Light from the xenon lamp collected by a mirror which then focused on the excitation monochromator, particularly on the entrance slit. There are two types of monochromator which are excitation monochromator and emission monochromator. For both monochromator, there are slits that are available at their entrance and exit. Width of the slit of excitation monochromator act to tune the band pass of light wave to the sample cell. Slit of the emission monochromator functions to tune the intensity of the fluorescence signal to the detector. Detector then act to count the photon that it encounters. In this work, PL source has 325 nm of wavelength and no special treatment is needed for sample to undergo PL characterization.

(a)



(b)

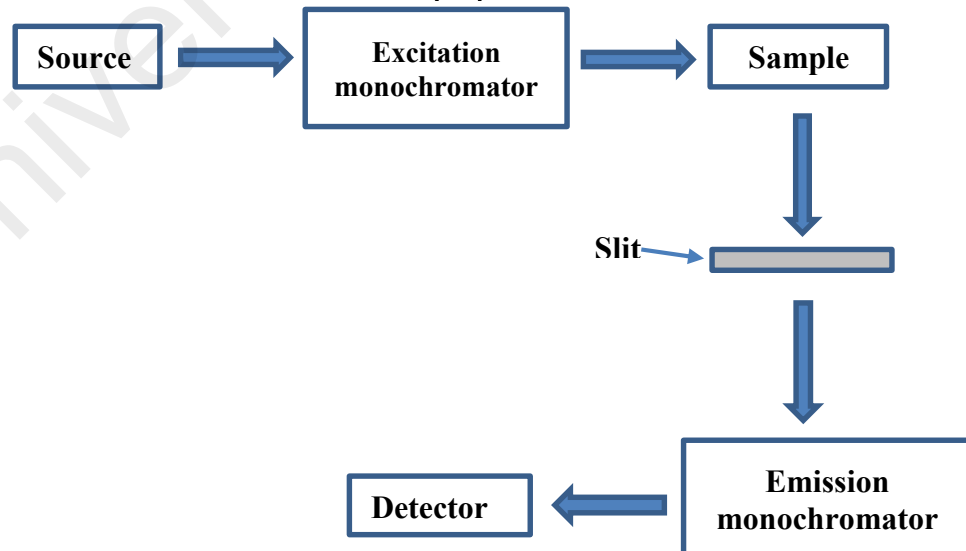


Figure 3.18: (a) Visual image and (b) schematic diagram of PL spectroscopy.

3.4.5 Structural Analysis

For structural analysis, Raman spectroscopy is the suitable characterization. Its theory is correlated with the ability of molecules to vibrate. These motions are instigated by specific frequency, which is normally in infrared region. These modes are quantized similar to atomic energy levels where lowest vibrational energy level of a molecule is zero-point energy. In this spectroscopy, molecules or ions would be irradiated by photons of known energy. In Stokes scatter, the target molecule will absorb the photon energy and excited to higher level or state. Some of the energy from the incident photon causes the molecule to move to higher level of vibrational and rotational states, while the remaining would be released as a photon. This type of photon is known as Raman photon. This photons' energy is equal to a transition of molecule from ground energy state to higher vibrational state for the studied molecule. Anti-Stokes scatter happens when a molecule in an excited state gains energy from the incident photon. Then it would decay back to a lower energy level or ground state by emitting higher energy photon than the incident radiation. Since very few molecules reemitted in the excited state, Anti-Stokes scatter does not predominate in a Raman Spectra. In Raman, light from laser collimated and reflected at a stationary mirror where this reflected light will be focused at the focus lens. From this focus lens, light then targeted to the sample cell. From there, the light continues to move through the camera lens to the polychromator where several slits are available in this part. From here, light will pass to the multichannel detectors which is a Charge Coupled Devices (CCD) which functions to detect the Raman scattered light. It has array of detectors to look at range of wavelengths. This kind of detector have eased the use of Raman spectroscopy by allowing scientist to take data precisely. In this work, we used Renishaw PL (Renishaw, UK) spectroscopy which its Raman laser has 514 nm of wavelength. Figure 3.19 portrays its schematic diagram.

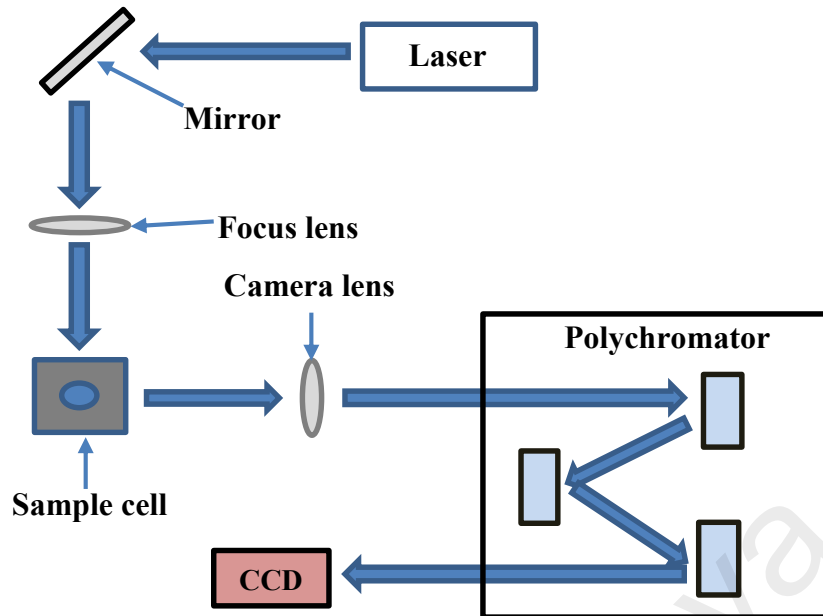


Figure 3.19: Schematic diagram of Raman spectroscopy.

3.4.6 Profilometer Characterization

In the present work, profilometer technique is used to measure the thickness of all samples. Profilometer machine model KLA Tencor (USA) is used and shown in Figure 3.20 (a). Usually, profilometer consists of two parts – a stage and a detector. Stage is needed to hold the sample so that the detector can scan it properly. Detector is crucial for determining the location of points of the sample. The stage to hold the sample usually is able to move so that measurement can be much efficient. In this work, stylus profilometer is applied where it utilises a probe to scan the sample surface. This probe will then obtain the height of surface by moving along it. This process is done mechanically with a loop that monitors the push force of the sample towards the detector when it scans along the sample surface. A feedback system which consists of z-axis point is used to keep the arm with a specific amount of torque on it, known as the set-point. Changes in z-axis position then used to reconstruct the surface. This type of profilometer requires physical touching to the sample surface. Figure 3.20 (b) exhibits this machine's schematic diagram.

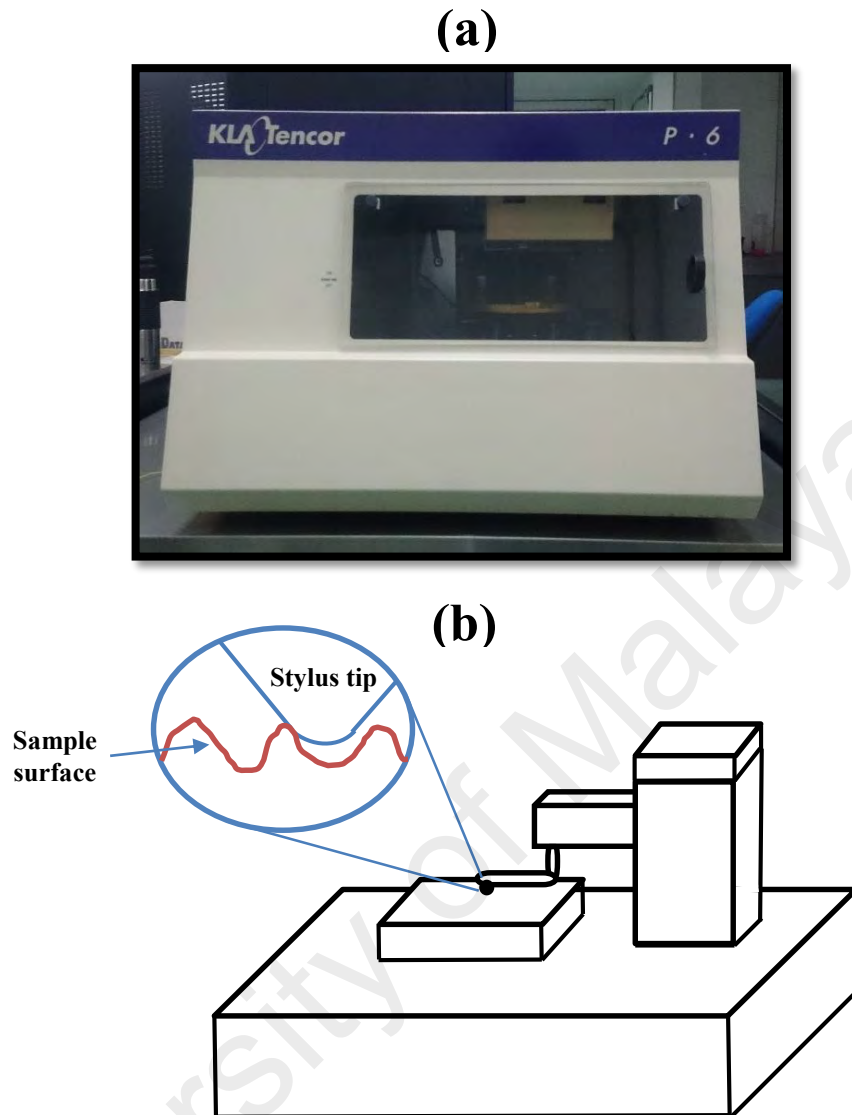


Figure 3.20: (a) Visual image and (b) schematic diagram of KLA Tencor stylus-type profilometer.

3.4.7 I-V Measurement

Samples will undergo I-V measurement using the 2-point probes that was tipped to the drain (aluminium) and source (silver nanowire) electrode contacts. The gate electrode contact was attached to another crocodile clip. These contacts were connected to the source meter unit (SMU) (Keithley, USA) to apply the voltage and record the current readings. Voltage that applied to gate electrode and drain electrode voltage is needed for the transistor output curve and transfer curve, respectively. For VOFET output graph,

gate voltage supplied was 0 - -6V while drain voltage supplied was 0 - 25 V. Meanwhile for transfer graph of VOFET, the gate electrode supplied between -10 to 10 V while its drain voltage was -5 and -10 V. These readings were transferred to the software installed in PC. The setup of this measurement is shown in Figure 3.21. Table 3.1 shows the simple description of IV measurement setup.

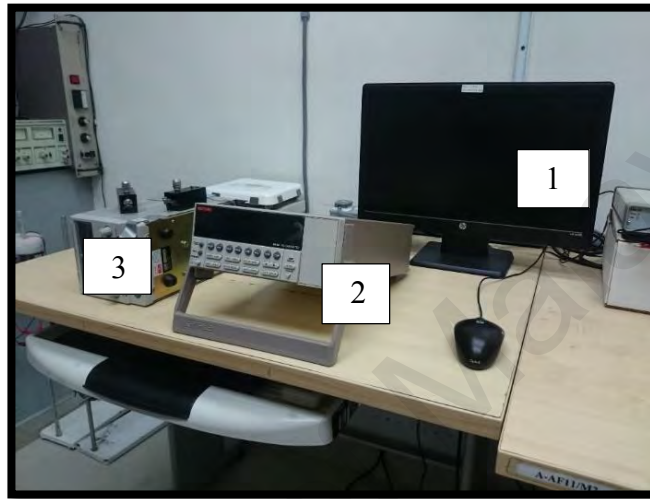


Figure 3.21: I-V Measurement Set-up.

Table 3.1: Descriptions of IV characterization equipment.

No.	Components	Functions
1	PC	To analyse the data and curves
2	SMU	To apply voltage and to tabulate data
3	2-points probes	To connect to drain and source of sample

CHAPTER 4: SYNTHESIS OF POROUS AAO TEMPLATES

4.1 Introduction

In this chapter, we are going to discuss the results for the production of porous anodic aluminium oxide (AAO) templates by using different stirring rate applied. The discussions including morphological, optical and structural studies. Besides, there are study about the application of different concentrations of acid for AAO templates' pore widening purpose and comparison about the production of template on top of glass and ITO which still comprising of morphological, optical and structural characterizations.

4.2 Results and Discussion

4.2.1 Anodization Process

Figure 4.1 shows the anodization graph of current (mA) versus time (s) for both no stirring and stirring process. In graph (a), shape of graph obtained is almost the same as Taşaltın and co. (Taşaltın et al., 2009) except that sulphuric acid is used in our work. Besides, this graph occurs in much shorter period. This may due to the thinner aluminium layer, which enable anodization to occur rapidly. Initially, current will decrease rapidly due to the production of aluminium oxide barrier layer. Little increase in current shows that the pores started to be produced at random locations. The constant current indicates the self-organizing of pores while the further decrease in current is due to penetration of pores to the glass surface which increased the resistance and reduced the current. In graph (b), the current is gradually decreased between 0 and 5 s of anodization until it achieved its steady decrement in current at $\sim 5 \times 10^{-4}$ mA. Current is started to decrease which may have been due to the oxidation of aluminium film. An individual crack may have been formed during this stage, and gradually move through the barrier layer randomly. These cracks then acted as nucleation sites for the pores construction. Formations of self-organized pores are initiated where their structure's composition is dominated by alumina

(Al₂O₃). The steady reduction of current has supported that the steady penetration process of pores into the alumina layer most likely facilitated by the stirring process. Anodizing current is highly related to the movement of oxygen molecules (originated from acid), which possess ions with oxygen (O²⁻ or OH⁻). These ions move through the barrier layer (situated at the bottom of pores) into the interface of oxide layer with the occurrence of outward drift by Al³⁺ ions across the oxide structure. When the formation of oxide layer is sufficient enough, diffusion of ions start to be limited and diffusion path become longer along the porous layer (Sulka & Stepniowski, 2009). Figure 4.1 (a) and (b) illustrates the pore formation and the movements of ions during anodization process, respectively.

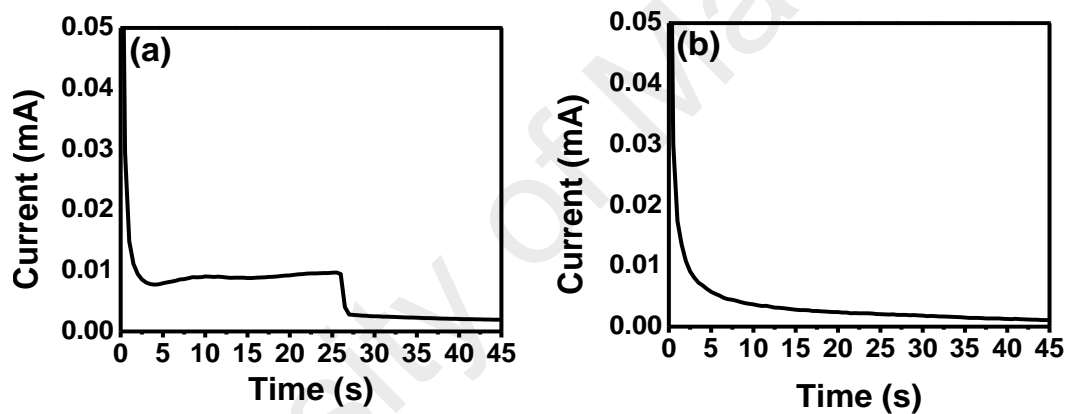


Figure 4.1: Anodization graph of (a) with and (b) without stirring process.

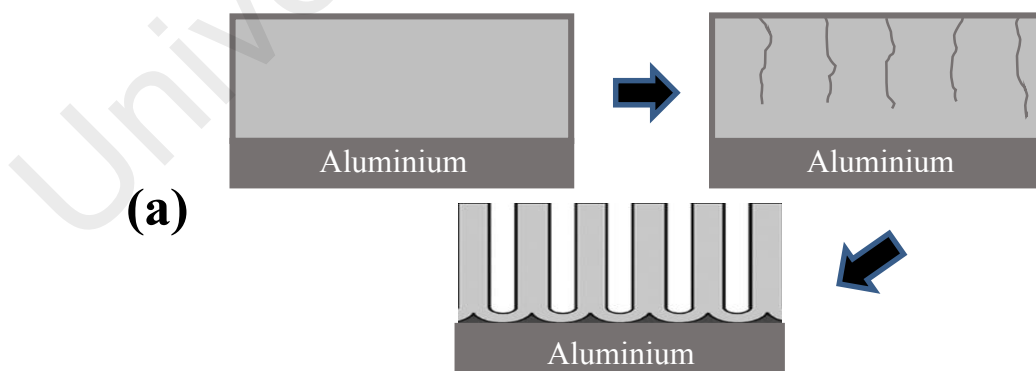


Figure 4.2: (a) Pores formation from pure Al, cracking process to nanochannel production and (b) movements of ions during anodization process.

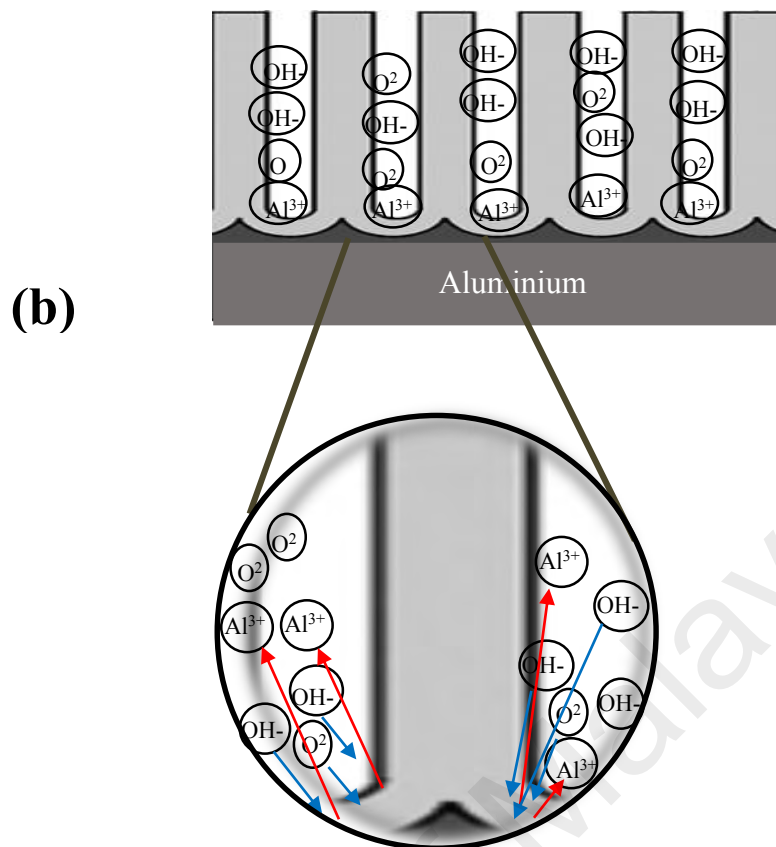


Figure 4.2, continued.

4.2.2 Synthesis The Porous Alumina and Alumina:VOPcPhO Nanocomposite.

Figure 4.3 (a-e) shows the FESEM images of AAO template that undergone pore widening in 5 % phosphoric acid at different stirring speeds of 0, 50, 100, 200 and 300 rpm, respectively. Comparing these four different stirring speeds with the one without stirring, huge differences by means of the shape of porous are detected. Three different shapes namely hexagonal-, rounded- and elongated-like porous are observed by stirring the electrolyte at 0, 50, 100 and 200 rpm, respectively. AAO template that fabricated without any stirring process has produced a bigger pores size if compare with template that undergone stirring process. Although, AAO template without stirring produces a bigger pores size, its homogeneity is inconsistent. Throughout the template surfaces, pores are likely to enlarge which lead to the formation of thin-walled porous. Some of the pores become larger than the others due to the recombination of two or more pores. The

plot profile for no stirring sample exhibits largest pores sizes variation among all samples. Stirring process could assist to the better dispersion of electrolyte by disturbing the static solution. However, the speed of stirring has a significant effect to the formation of nanopores. Between the speed of 50 and 200 rpm, uniform formation of pores sizes of smaller diameter and thicker wall are observed. Plot profiles from 50 to 200 rpm show increment in homogeneity and pores density from 50 to 200 rpm with slightly smaller decrement in pores sizes. Sample of 100 rpm stirring presents the densest pores among the other three speeds with 1540 pores while sample with 200 rpm has 932 pores, sample with 50 rpm has 780 pores and lastly sample with no stirring has 650 pores. This observation has led to the assumption that at the certain point (saturated), the pore will have to stop its expansion to avoid any recombination of two or more pores during anodization, which latter create a thicker wall. Despite of having a better homogeneity porous growth at higher stirring speed, increase the speed even higher to 300 rpm has resulted in adverse formation. From plot profile, no well-arranged pores view presented for this sample. Instead of forming the uniform pores size, AAO template has only experienced the elongated-like pore shape of incomplete anodization on its surface. The elongated-like shape is a gap between the cracked alumina layers of poor transformation from its film to porous structure.

In a closed system of only the small volume of heat is allowed to escape, the stirring effect could provide temperature uniformity aside from low temperature outside the beaker. Due to the movement of substance within the electrolyte solution, the kinetic energy will then be converted into thermal energy and satisfied the principle of conservation energy. The stirring process during anodization can slightly increase the local temperature of electrolyte acid and thus, further increase the rate of anodization (oxide dissolution and formation) and produce the smaller, more abundant and homogenous nanopores array. At 300 rpm, the stirring is very much faster which causes

the less hydrogen ion from electrolyte to fully attack the aluminium film. As reported elsewhere (Sulka & Stepniowski, 2009), 500 and 800 rpm of stirring speeds have been used in anodization process and succeeded to produce the unvarying nanopores structure. However, these speeds are applied on aluminium film with thickness of 0.25 mm in multi-steps anodization process with the fully complete anodization process is achieved.

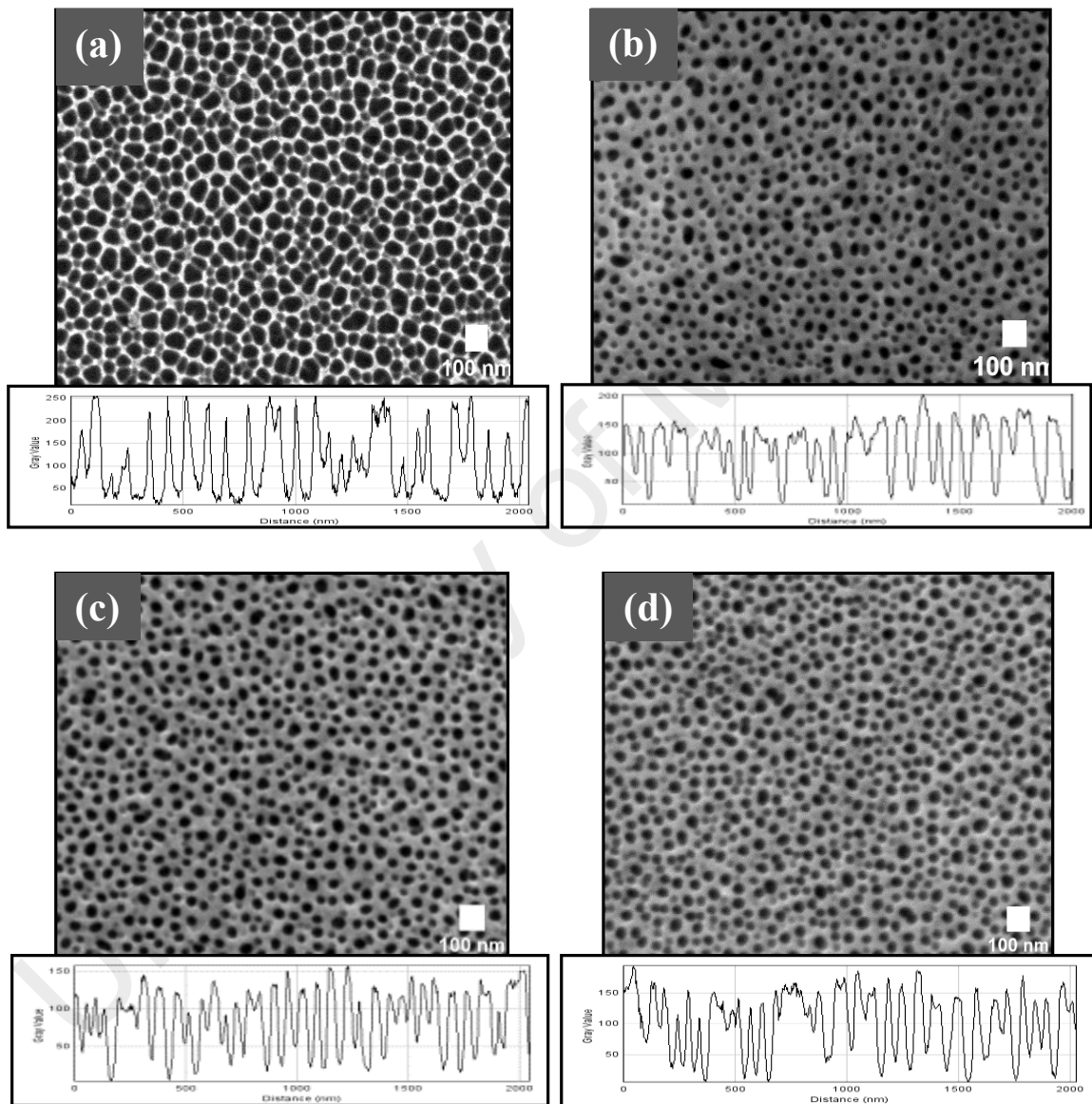


Figure 4.3: FESEM images of AAO template with 5% of phosphoric acid (widening) at stirring speed of (a) 0 rpm, (b) 50 rpm, (c) 100 rpm, (d) 200 rpm, and (e) 300 rpm (outset is a plot profile).

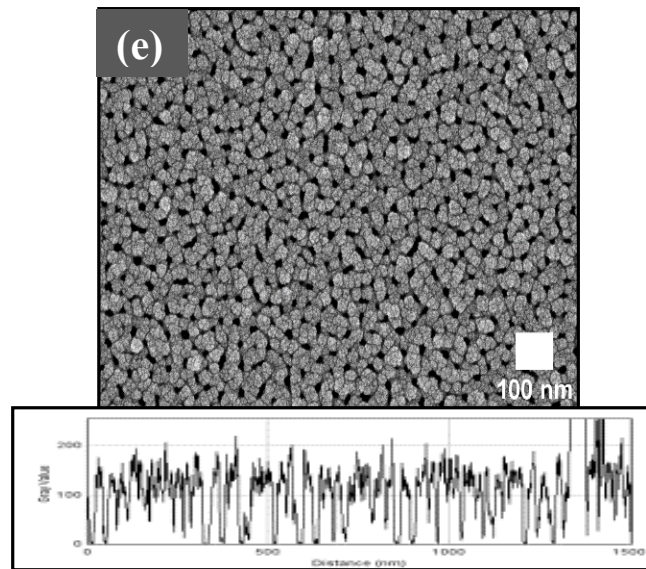


Figure 4.3, continued.

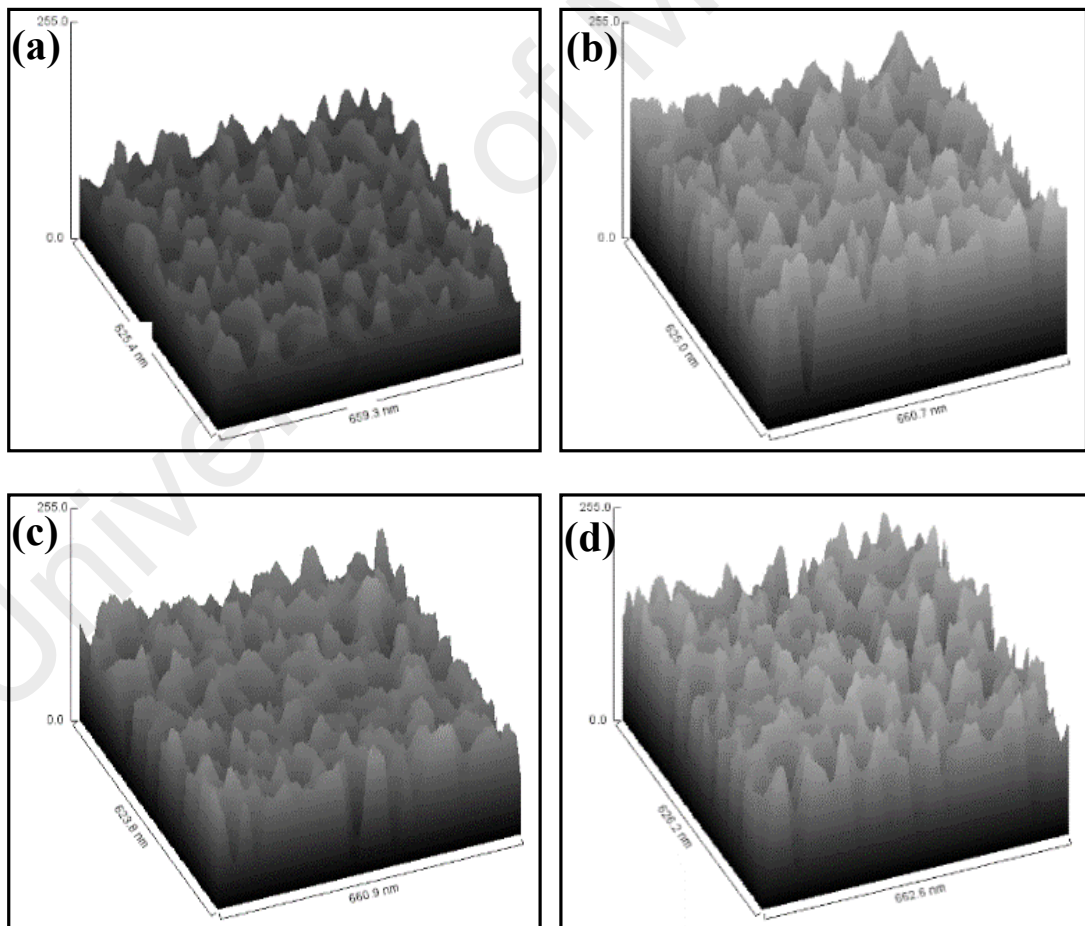


Figure 4.4: 3-Dimensional surface plot of AAO template with 5% of phosphoric acid (widening) at stirring speed of (a) 0 rpm, (b) 50 rpm, (c) 100 rpm, (d) 200 rpm, and (e) 300 rpm (the analysed surface area is 628 nm x 660 nm).

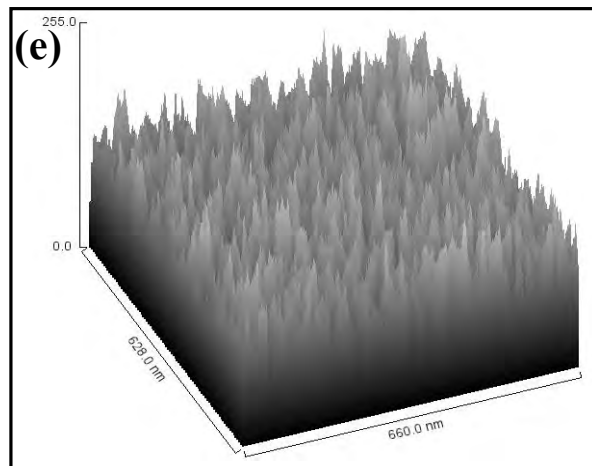


Figure 4.4, continued.

Figure 4.4 (a-e) shows a 3D surface plot of AAO template with 5 % of phosphoric acid (widening) at stirring speed of 0, 50, 100, 200 and 300 rpm, respectively. The size of analysed surface area is approximately 628 nm x 660 nm. These 3D surface plot graphs give information on their possible thicknesses, however, not quantitatively on their surface roughness. Looking at these 3D graphs, confirmation on the formation of porous structure from all parameters can be deduced. The only difference shown between these surface plots is the opening porous which represents its pores size. If comparison between 0 and 200 rpm is made, identical opening porous is likely to be dominated by 50, 100 and 200 rpm of stirring speed. This observation is supported by their top-view FESEM images and plot profile. During the stirring process, perturbation on the static solution (electrolyte) is occurred with means of the dispersion of ions. Stirring rate affects the dispersion of electrolyte ions (O^{2-} or OH^{-}) to be transported to the anode surface i.e. sample. At 50 till 200 rpm, ions get well dispersed across samples. At 300 rpm and higher, collision between ions occurs vigorously and thus highly affects ions dispersion, which reduces the density of porous formation on sample. On the other hand, at 300 rpm and higher, much more stir force will exert to electrolyte ions, which start to act upon the sample. Therefore, these ions could get washed away from sample.

Stirring speed of 100 rpm is chosen for the further synthesise of porous AAO of different pore widening parameters due to its capability in producing uniform structured porous. Figure 4.5 (a-c) show the FESEM images and plot profiles of AAO template at stirring speed of 100 rpm with no pore widening, widening in 5 % phosphoric acid and widening in 10 % phosphoric acid, respectively. As expected, the porous AAO with no pore widening treatment, presents the irregular pores size with elongated-like porous. Plot profile proves this statement with no well-arranged pores presented in this sample. Sample with pore widening of 5wt. % phosphoric acid produced nanoporous structures shown in Figure 4.5 (c). Sample with pore widening of 10wt.% phosphoric acid however has larger pores formed with 40 nm diameter as the most abundant pores size with porous structures with non-uniform height and wall thickness. In fact, we can see that many of these holes actually start to merge with their neighbouring pores. This is due to the effect of higher molarity acid which is having more hydrogen ions and molecules will increase the reaction rate of pores with the shorter period of time, accelerating the alumina's dissolution but reducing pores' growth rate (Houng et al., 2014). Both stirring speed and pore widening treatment play the essential roles in producing the porous AAO template. Rounded-sphere pores will unlikely to be formed if the highest stirring speed or lowest molarity of phosphoric acid is applied. No pore widening treatment has led to an occurrence of non-expansion nucleated pore. Figure 4.6 (a-c) show the 3D surface plots of porous AAO template with no pore widening, widening in 5 % phosphoric acid and widening in 10 % phosphoric acid, respectively. The 3D surface plots support the formation of porous structure displayed in top view of FESEM images.

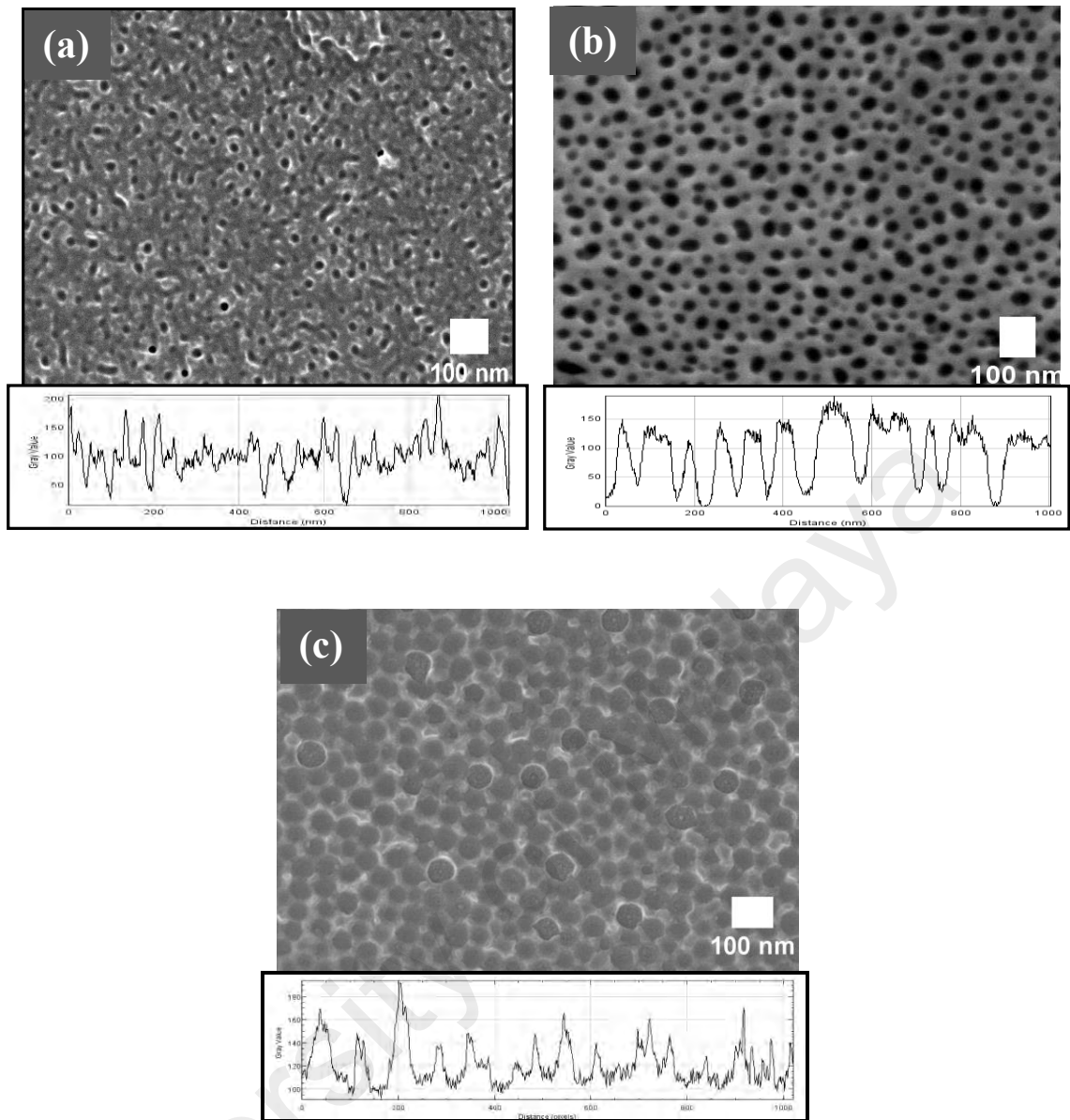


Figure 4.5: FESEM images of AAO template at stirring speed of 100 rpm with (a) no pore widening, (b) widening in 5 % phosphoric acid and (c) widening in 10 % phosphoric acid (outset is a plot profile).

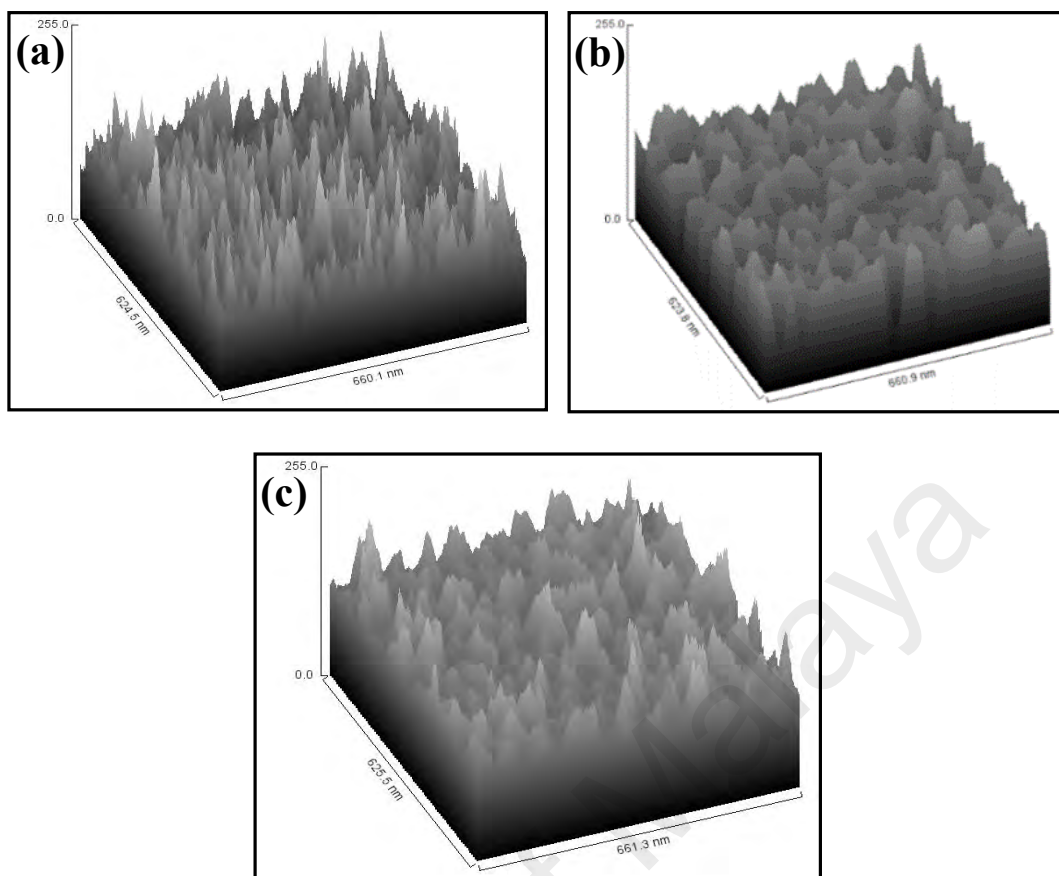


Figure 4.6: Surface plot of AAO template at stirring speed of 100 rpm with (a) no pore widening, (b) widening in 5 % phosphoric acid and (c) widening in 10 % phosphoric acid.

Figure 4.7 (a) shows the top-view FESEM image of AAO:VOPcPhO nanocomposite with the inset is its plot profile. Infiltration of VOPcPhO is done onto the porous AAO that synthesized from the parameter of 100 rpm of stirring speed and 5 % of phosphoric acid. As expected, the top surface (morphology) of nanocomposite is different from the top surface of porous AAO. This is due to the success infiltration of VOPcPhO into the porous AAO arrays. No rounded-sphere pores are detected from the top surface of nanocomposite apart from its undulating top surface. Undulating surface is most probably originated from the formation of VOPcPhO layer on top of porous AAO surface. Plot profile proves the presence of VOPcPhO since no clear pores presented in this plot. Infiltration and thin layer formation of VOPcPhO are supported by the cross-section view of FESEM image shown in Figure 4.7 (b). The FESEM image shows the infiltrated

VOPcPhO between the pores with a very thin layer of VOPcPhO on top of it. This brings to the fabrication of AAO:VOPcPhO nanocomposite with the thickness of porous AAO and VOPcPhO layer on top of it, is approximately 85 ± 5.5 nm and 95 ± 5.0 nm, respectively. It is clearly seen that two different regions of brighter and darker, which corresponds to AAO and VOPcPhO, respectively, are successfully created. As reported elsewhere (Kamarundzaman et al., 2013; Makinudin et al., 2015), VOPcPhO solution is capable to infiltrate into nanoporous with pores size between 20 and 200 nm.

There is no doubt for the VOPcPhO infiltration to occur into the porous AAO with pores size between 10 and 60 nm as synthesized in the present study. However, due to the lengthy immersion time of 6 hours, excess layer of VOPcPhO is created which makes total thicknesses of VOPcPhO inside the porous arrays (85 nm) and its top layer (95 nm) is approximately 180 nm. Figure 4.7 (c) & (d) show the 3D surface plot and simulation image of AAO:VOPcPhO nanocomposite which its dissimilarity with porous AAO template's morphological properties is observed. This observation has confirmed the postulation on having VOPcPhO as a capable guest material to wetting the pores' wall of higher surface tension. VOPcPhO solution with concentration of 5 mg/ml has undergone a flow into a channel of closed-end.

Understanding transportation of fluid in nanoscale is important in this part of work. A particular phenomenon considered is capillary filling (CF) of nanochannels. This process has been experimented for open capillaries, which is touching with a liquid bath at a channel end. In this situation, CF happens with action of capillary force with viscous drag. In the sufficiently length channel, CF first occur by a fast density increase since the accommodation of molecules on the inner pore surface with unbinding of meniscus. After that, the meniscus accelerated towards the pore opening (Schneider et al., 2014). We can

assume that this type of fluid mechanics occurs in our nanochannel structures when VOPcPhO started to infiltrate into structures.

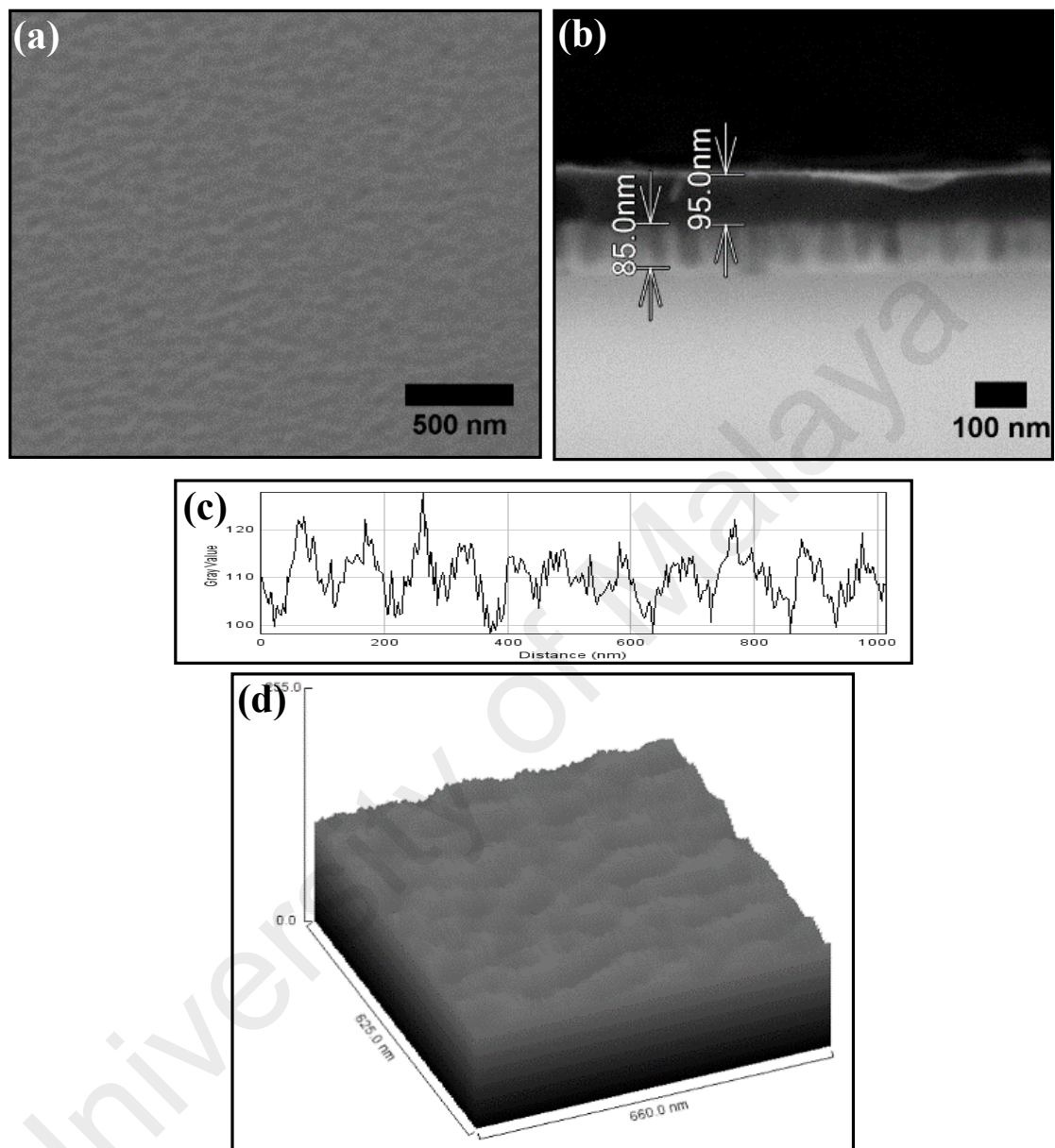


Figure 4.7: FESEM images of AAO: VOPcPhO nanocomposite in (a) top-view and (b) cross-section view, (c) surface plot of AAO: VOPcPhO nanocomposite and (d) 3D simulation of AAO: VOPcPhO nanocomposite surface.

Figure 4.8 (a) presents the bar chart of pores size of porous AAO template that not undergoes a stirring process with the mode and counts is 30 - 39 nm and 164 counts per area, respectively. The total counts of pores are 560 with the mean of its diameter size recorded to be 50.34 ± 17.63 nm. Porous AAO template that obtained from the stirring

speed of 50 rpm (Figure 4.8 (b)) shows a higher homogeneity of structured pores if compared with the one without stirring. As the stirring speed is increase to 100 rpm (Figure 4.8 (c)), the pores size is almost similar; however, it is highly dense with more counts per area. Mode of pore size is 20.0 ± 9.56 nm with its counts per area is 608 and the total pores available are 1540 counts. Porous AAO template that synthesized by stirring at 200 rpm almost has the similar pores size with the former, however, recorded a slightly lower homogeneity of pores (Figure 4.8 (d)). Porous AAO template with no stirring can produce a larger pores size despite of having non-homogenous pores size. In contrary to the pores size, template that produced higher pore counts per unit area has resulted to the decrease in size. Figure 4.8 (e) presents the similar pores size and pores counts per unit area as Figure 4.8 (c) since they undergone the similar anodization parameter process. Figure 4.8 (f) depicts the pore distribution of template with 10 % of phosphoric acid of pore widening treatment. With the higher concentration of acid, the largest pores size of 40-49 nm can be formed with the counts per unit area are 292. The reason to the largest formation of the pore size is the occurrence of individual pores' merging with their neighbouring pores. A higher molarity of phosphoric acid can contribute to a higher availability of hydrogen ions and molecules. Therefore, the reaction rate to form the pore is increased, with more area is being attack by hydrogen ions and molecules to construct a bigger pore (Houng et al., 2014).

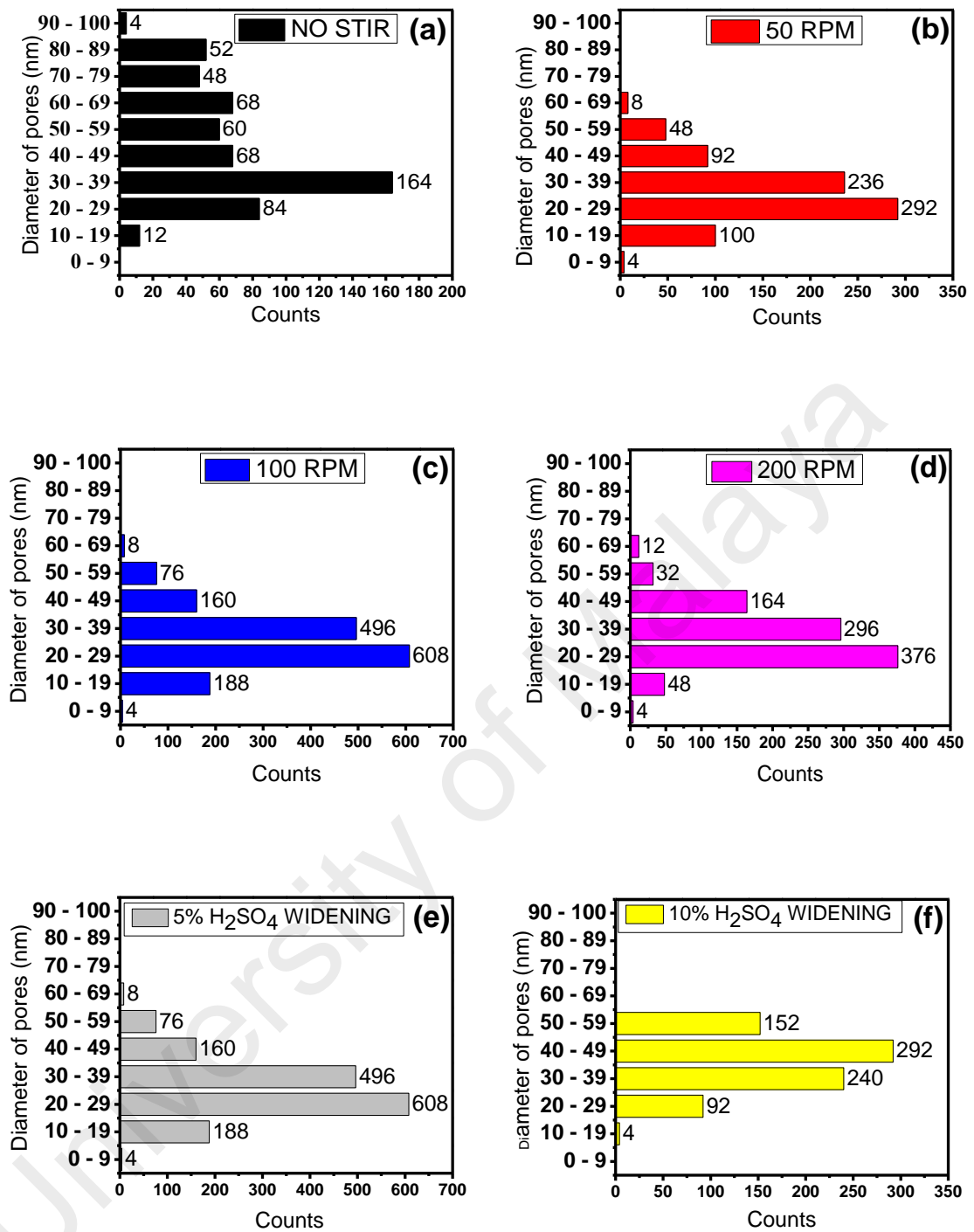


Figure 4.8: Chart distribution of template with pores diameter of (a) 0 rpm, (b) 50 rpm, (c) 100 rpm, (d) 200 rpm, (e) widening in 5 % phosphoric acid and (f) widening in 10 % phosphoric acid.

4.2.3 Optical Characteristics of Porous Alumina and Alumina:VOPcPhO Nanocomposite.

Figure 4.9 (a) demonstrates the transmission spectra of glass and porous AAO template of different stirring speeds deposited onto glass. As demonstrated in the spectra, glass with no deposition of AAO, depicts 100 % of transmittance, which is used as reference. Porous AAO templates that obtained by stirring the speed between 50 and 200 rpm record transmittance between 45 % and 85 % with 200 rpm of stirring speed produced a higher transparency template. Meanwhile, porous AAO template that fabricated with no application of stirring recorded the lowest transmittance percentage of 28 %. Transparency presented by template without stirring has much connected to its morphological properties. As mentioned earlier, template without stirring has a wider pore size distribution between 10 and 90 nm than the template with stirring. The range of pore size distribution of template with stirring is between 10 and 60 nm. Due to the variations of pore size, light interference order and light absorption will be higher. The less transparent porous AAO template of larger pore size variations can cause to the higher absorption by the available acid radical and aluminium remains (Peitao et al., 2011) since template is not undergoing the annealing treatment. Refractive index of glass n_s is calculated using the (4.1) (Zhuo et al., 2011) while other samples' refractive index calculated using Manifacier method by using Equation (4.2) and (4.3). Porous AAO template of no stirring, 50, 100 and 200 rpm has recorded a refractive index of 3.86, 3.76, 3.38 and 2.94, respectively, while a refractive index of glass substrate used in this study is 1.15.

$$n_s = \frac{1}{T_s} + \left(\frac{1}{T_s^2} - 1\right)^{1/2} \quad (4.1)$$

where T_s = transmittance of glass substrate and n_s = refractive index of glass.

$$n = (N + (N^2 - n_s^2)^{\frac{1}{2}})^{\frac{1}{2}} \quad (4.2)$$

where n_s = refractive index of glass and N can be obtained from equation 4.3 below.

$$N = 2 n_s \frac{T_{max} - T_{min}}{T_{max} T_{min}} + \frac{n_s^2 + 1}{2} \quad (4.3)$$

where T_{max} and T_{min} is maximum and minimum transmittances for each wavelength with peak.

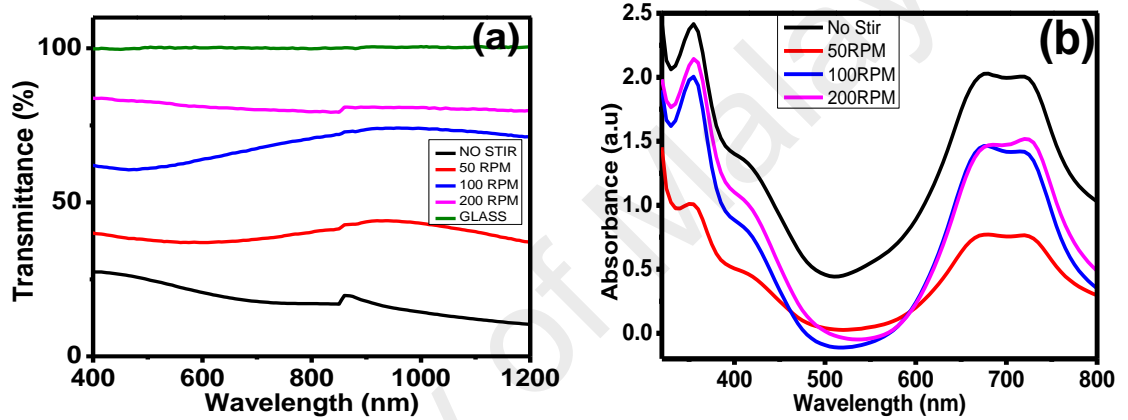


Figure 4.9: UV-vis spectra of (a) transmission of AAO template and (b) absorption of AAO:VOPcPhO nanocomposite.

Figure 4.9 (b) shows the UV-vis absorption spectra of infiltrated VOPcPhO. Peaks observed are tabulated in Table 4.1. The first peak is corresponded to the Soret-band while the latter two peaks are corresponded to the Q-band. As reported elsewhere, UV-vis absorption peaks for VOPcPhO thin film are 348 nm at Soret-band while 677 and 713 nm at Q-band (Makinudin et al., 2015). As in Table 4.1, peaks obtained by 100 rpm stirred sample are 355, 679 and 721 nm while 200 rpm stirred sample has 354, 683 and 720 nm peaks and 50 rpm stirred sample has peaks at 354, 678 and 718 nm which all peaks are red-shifted compared to VOPcPhO thin film peaks. These redshifted peaks most likely to occur due to the VOPcPhO nanotubes in nanoporous structures resulted from VOPcPhO infiltration. The sample without stirring possesses has two redshifted peaks at 354 and

715 nm while peak at 677 nm indicating the presence of VOPcPhO thin film on top of the nanoporous structures. These observations support that stirred samples are better light absorber than no stirred sample since more VOPcPhO is able to infiltrate into nanoporous structures homogeneously with 100 rpm stirred sample that has two highest redshifted peaks than other two stirred samples at 355 and 721 nm peaks. Low homogeneity of nanoporous structures in no stirred sample will halt more material to be infiltrated. Postulation on the dependency between template architecture and absorption of photon can be rather acceptable. From Figure 4.9 (b), all graphs exhibit shoulder at 397, 398, 399 and 400 for 50, 100, 200 and 0 rpm samples, respectively. At Q-band of no stirred sample, stronger peak than stirred sample is observed at 715 nm. The first π - π^* transition on phthalocyanine macro-cycle is more dominant for the no stirred sample (Supangat et al., 2014). This occurs since most VOPcPhO obtained on this sample lay onto its nanoporous structure instead of infiltrate. Therefore, more light will be absorbed into the VOPcPhO layer rather than AAO:VOPcPhO nanocomposites.

Table 4.1: Peaks absorption of alumina: VOPcPhO nanocomposites.

Bands / Stirring speeds	0 rpm	50 rpm	100 rpm	200 rpm
B-band	354 nm	354 nm	355 nm	354 nm
1 st Q-band	677 nm	678 nm	679 nm	683 nm
2 nd Q-band	715 nm	718 nm	721 nm	720 nm

Figure 4.10 (a) shows the PL spectra of AAO:VOPcPhO nanocomposites plotted between the wavelength of 400 and 1000 nm. PL peaks observed are tabulated in Table 4.2. Peaks of 100 and 200 rpm stirred samples are shifted. The distinguishable shifts for 100 and 200 rpm stirred sample to longer wavelength compared to the no stirred sample occurred by 2 nm for sample of 100 rpm stirring and 1 nm for sample of 200 rpm stirring. Besides that, compared to no stirred sample, sample of 100 rpm and 200 rpm stirring have

other shifts by 7 nm and 6 nm, respectively. In this characterisation, molecules from VOPcPhO and AAO will interact with visible light wavelength. Then, the molecules energized due to excess energy before ‘jump’ to excited state of energy. These molecules then ‘jump down’ to lower energy level and emit photons amid the process. These photons are the difference in energy levels between the two states involved in the transition. Quenching effect is observed for porous AAO template that synthesized at stirring speeds of 100 and 200 rpm, which exhibited a better photo-induced charge transfer.

Table 4.2: Photoluminescence peaks of alumina: VOPcPhO nanocomposites.

PL peaks (nm)				
Peaks originated	0 rpm	50 rpm	100 rpm	200 rpm
Alumina template	578	577	585	579
VOPcPhO	720	716	721	720
VOPcPhO	787	788	794	793

Figure 4.10 (b) shows the Raman spectra of AAO:VOPcPhO nanocomposites of different parameters. The nanocomposites exhibited the similar Raman shifts however with different intensities. Assignments and changes of wavenumbers are presented in Table 4.3. From the table, 100 rpm sample exhibit shifts at 687, 1003, 1024, 1193, 1236, 1341, 1464, 1528, 1591 and 1616 cm^{-1} which correspond to VOPcPhO nanotubes (Makinudin et al., 2015). The remaining shifts at 838 and 1113 cm^{-1} are corresponding to the VOPcPhO thin film. These are most probably corresponding to the VOPcPhO layer on the top surface. This sample also possesses a shift at 1395 and 1479 cm^{-1} that does not correspond to any of VOPcPhO structure. On the other hand, 0 rpm sample exhibits shift at 686, 838, 1002, 1113, 1192, 1232, 1527 cm^{-1} that correspond to VOPcPhO thin film. The shifts at 1024, 1464 and 1590 cm^{-1} is corresponding to VOPcPhO nanotubes. Meanwhile, shifts at 1339, 1395, 1479 and 1615 cm^{-1} do not correspond to any VOPcPhO structures. Overall, the stirred samples presented more VOPcPhO nanotube shifts

compared with the no stirred sample. Each upward shift occurred between no stirred and stirred samples are around 1-5 cm^{-1} . These is related to the structures of template themselves where stirred samples have higher homogeneity of nanostructures. These upward shifts are due to the change in wavelength of scattered light when passing through VOPcPhO that infiltrated inside the alumina nanoporous compared to other shifts that passing through VPOcPhO layer that lay on top of the alumina nanoporous. Higher intensity shifts at 686/687, 1527/1528 and 1615/1616 cm^{-1} exhibit macrocycle breathing, pyrrole stretching and C=C stretching, respectively, are dominant in the infiltrated VOPcPhO.

Table 4.3: Raman shift and assignments of alumina: VOPcPhO nanocomposites.

Raman shift (cm^{-1})				Assignments
0 rpm	50 rpm	100 rpm	200 rpm	
686	687	687	687	Macrocycle breathing
838	838	838	838	Macrocycle stretching
1002	1003	1003	1003	Benzene ring breathing
1024	1024	1024	1029	C-H bending
1113	1113	1113	1113	
1192	1192	1193	1193	
1232	1231	1236	1232	
1339	1339	1341	1342	Pyrrole stretching
1395	1395	1395	1396	Ring stretching
1464	1464	1464	1469	
1479	1477	1479	1479	
1527	1528	1528	1528	Pyrrole stretching
1590	1588	1591	1591	C=C stretching
1615	1616	1616	1616	

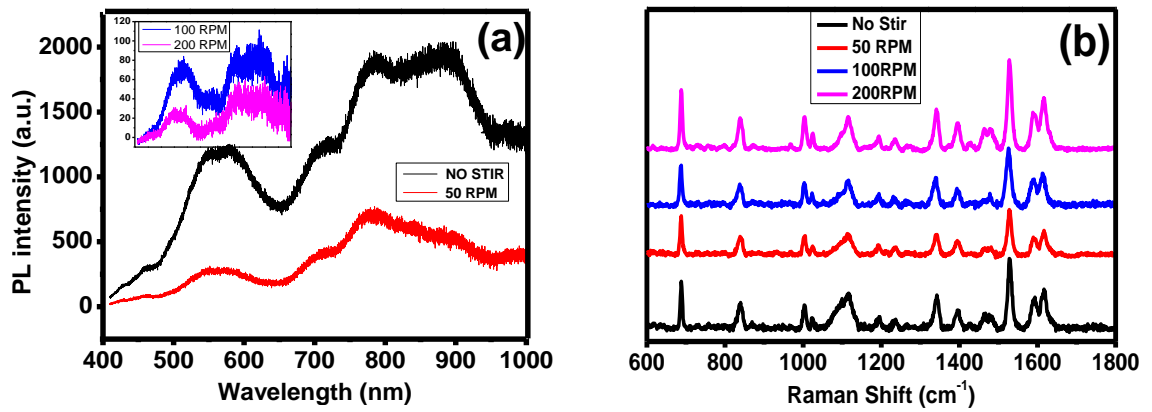


Figure 4.10: (a) PL spectra and (b) Raman spectra of AAO:VOPcPhO nanocomposites.

4.2.4 Anodization Process onto Glass and ITO Substrate

FESEM images in Figure 4.11 exhibit AAO templates produced on top of (a) glass and (b) ITO substrates with 100 rpm stirring rate in sulphuric acid. From these images, both substrates do not produce nanoporous template with morphology that is almost the same in terms of size and amount of nanopores. In the chart distribution of Figure 4.12, the pattern of number of pores for each class of pores sizes is almost the same. Only the total number of pores is slightly less on ITO compared to glass substrate, which is 1455 and 1540, respectively. From 3D surface plot in Figure 4.13 (a) & (b), pores amount pattern is about the same, which does correlate with the chart distribution in Figure 4.12 (a) & (b) except that the sharp pattern produced for template on ITO compared on glass.

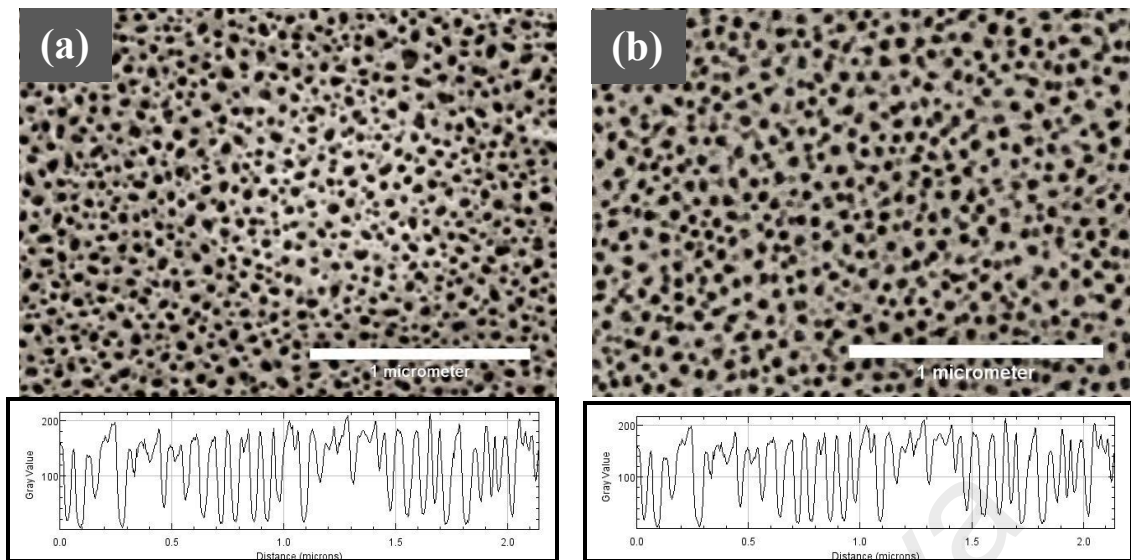


Figure 4.11: FESEM images of AAO on (a) glass and (b) ITO with stirring rate of 100 rpm in sulphuric acid.

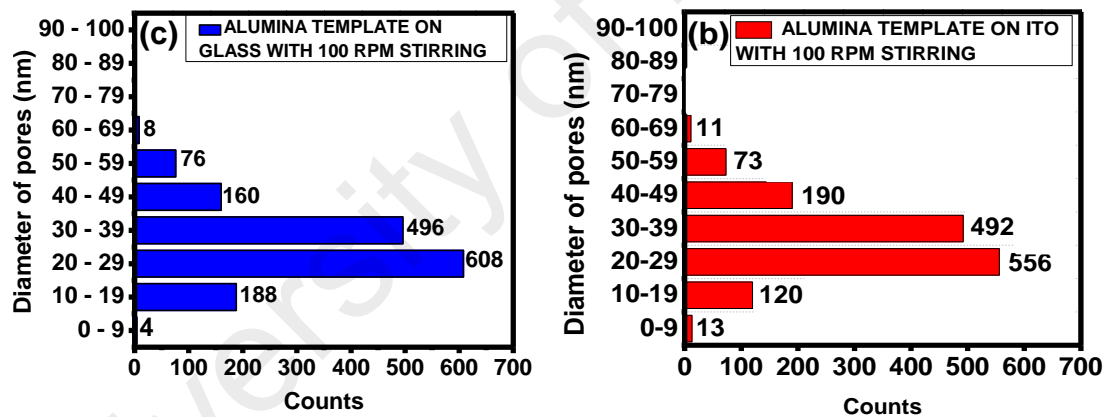


Figure 4.12: Chart distribution of template with 100 rpm stirring on (a) glass and (b) ITO substrates.

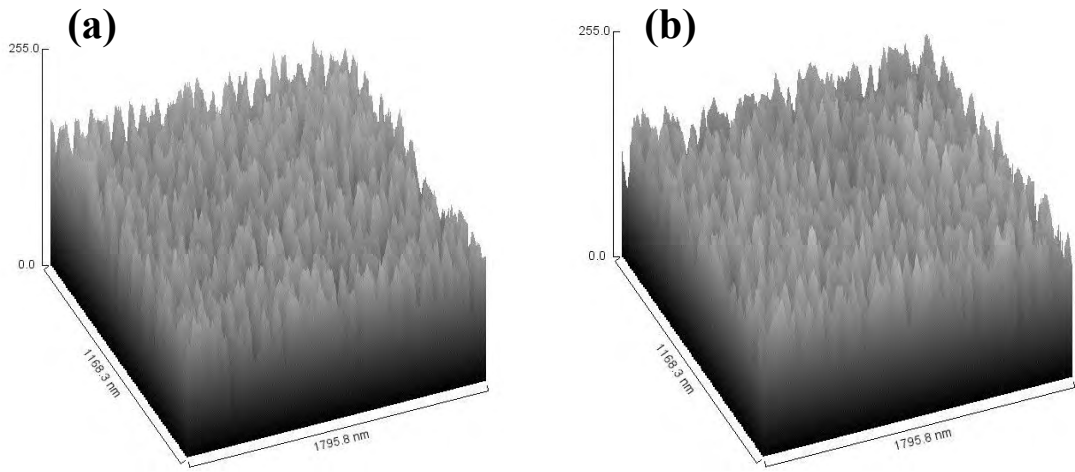


Figure 4.13: 3D surface plot of AAO template on (a) glass and (b) ITO substrates.

FESEM images in Figure 4.14 (a) & (b) exhibit the AAO templates under anodization of 40 V with sulphuric acid as electrolyte. From these images, it is clear that their structures are rough and damaged compared to other templates produced. This is most probably due to high voltage employed rather than 25 V which is normally practiced by researchers for anodization using sulphuric acid (Sulka & Parkola, 2007). Other than that, both images exhibit almost the same morphology. This experiment is to confirm that the higher voltage can ruin the morphology of porous AAO template and not recommended to be used in future.

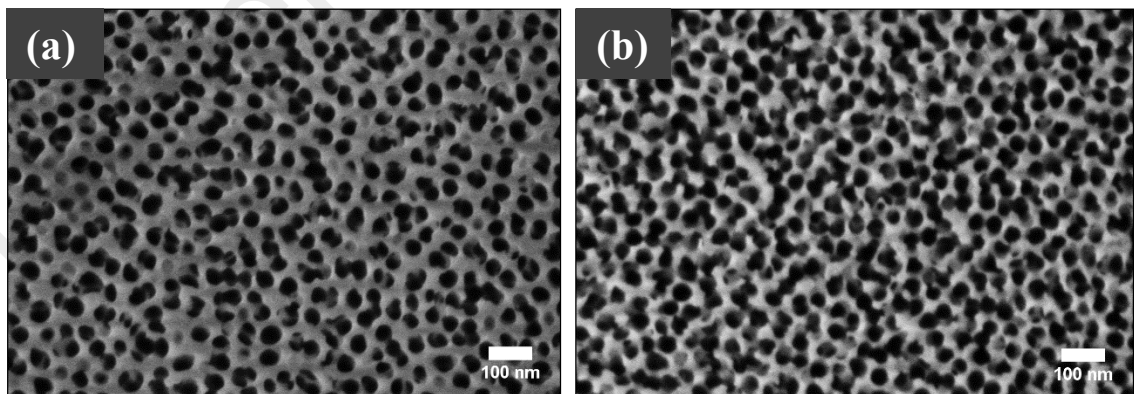


Figure 4.14: FESEM images of AAO under anodization of 40 V on (a) glass and (b) ITO.

4.3 Summary

In summary, varying the stirring rates of anodization can produce the porous AAO templates. The produced AAO templates show some significant morphology changes in size and number of pores of each template. The significant change in morphology also happens by varying the different concentration of phosphoric acid in the pore-widening step. Table 4.4 exhibits the basic comparisons between different stirring rates in anodization process. Table 4.5 shows the results of AAO template produced on the different substrates of glass and ITO. It suggests that these AAO templates can be produced on the different substrates with almost the identical morphology. Therefore, in this work, 100 rpm stirring rate will be applied for the synthesis of AAO templates using ITO as a substrate in VOFET application since it produced the most uniform and most abundant nanoporous structures regardless of their smaller sizes compared to nanoporous from other stirring rate template.

Table 4.4: Results of different stirring rates.

Stirring rate (rpm)	Mode size of pores (nm)	Count of mode size of pores	Mean size of pores (nm)	Total count of pores	$\frac{\text{Count of modal size}}{\text{Total count of pores}}$
0	(30.0 ± 6.05)	164	(50.34 ± 17.63)	560	0.293
50	(25.00 ± 2.34)	292	(38.78 ± 10.45)	780	0.374
100	(20.84 ± 9.56)	608	(33.33 ± 12.99)	1540	0.397
200	(21.35 ± 3.35)	376	(41.20 ± 17.02)	932	0.401

Table 4.5: Results of different substrates.

Substrates	<u>Count of modal size</u> Total count of pores
Glass	0.397
ITO	0.395

University of Malaya

CHAPTER 5: THIN FILM VOFET AND NANOSTRUCTURED VOFET

5.1 Introduction

In this chapter, discussions on the results of Vertical Organic Field Effect Transistor (VOFET) with two systems: one with thin film dielectric layer (PVDF-TrFE) and another one with nanostructured layer of PVDF-TrFE are presented. Dielectric layer of P(VDF-TrFE) has been altered from non-porous film to the porous film with the integration of templating method by using AAO template for the replication process between the template and P(VDF-TrFE) to occur. It is found that the replication process has generated the porous structure of P(VDF-TrFE). By deploying porous AAO template, the effect of non-porous and porous dielectric layer in VOFET can be further elaborated. The results comprised of morphological, structural, chemical and electrical of samples and device fabricated.

5.2 Results and Discussion

5.2.1 Alumina Porous Template and P(VDF-TrFE)

AAO template that produced from aluminium foil or aluminium deposited onto substrate will produce porous structures all across the template (Naber et al., 2005; Xu et al., 2000). Figure 5.1 (a) exhibits the FESEM image of AAO template produced via anodization technique. It is clear that high uniformity of template can be produced by using this affordable and effective technique. Cross-sectional and topography simulation images (Figure 5.1 (b) & (c)) show that high uniformity porous structures are successfully produced. There is clear presence of aluminium and oxygen which is the main element in the template (alumina) and the presence of carbon is due to glass substrate usage (Figure 5.1 (d)).

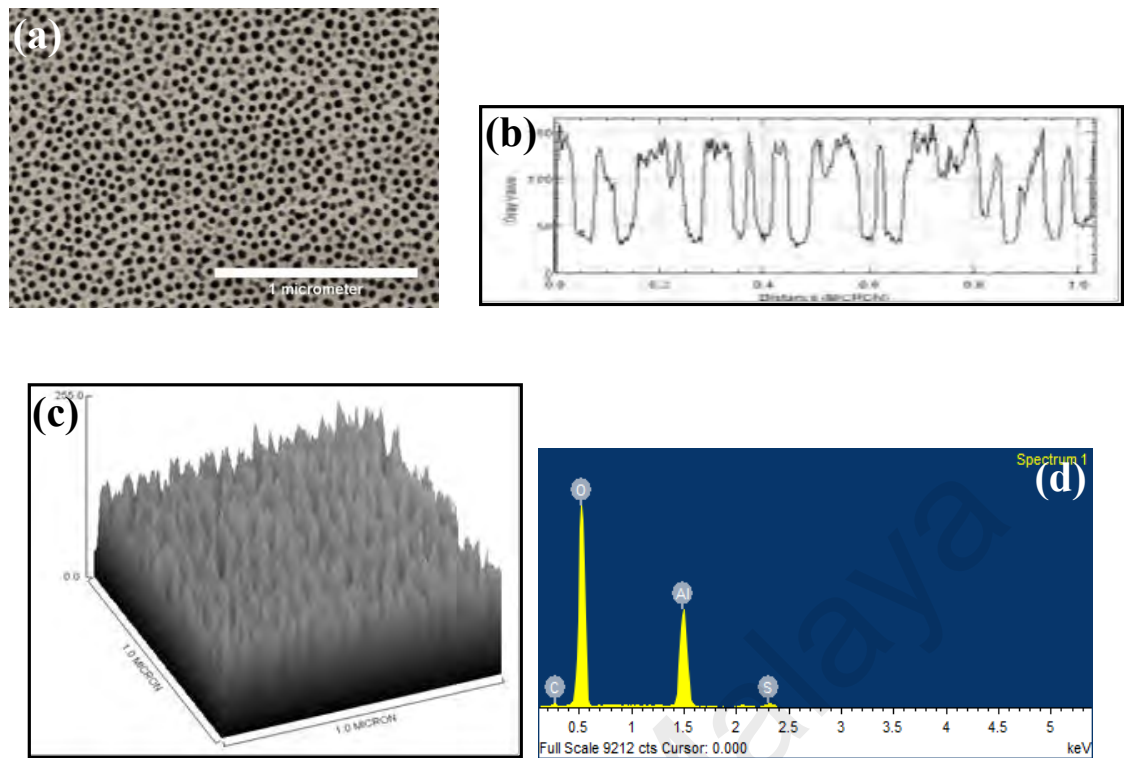


Figure 5.1: (a) FESEM image, (b) cross-sectional simulation view, (c) 3D simulation view and (d) EDX of AAO template.

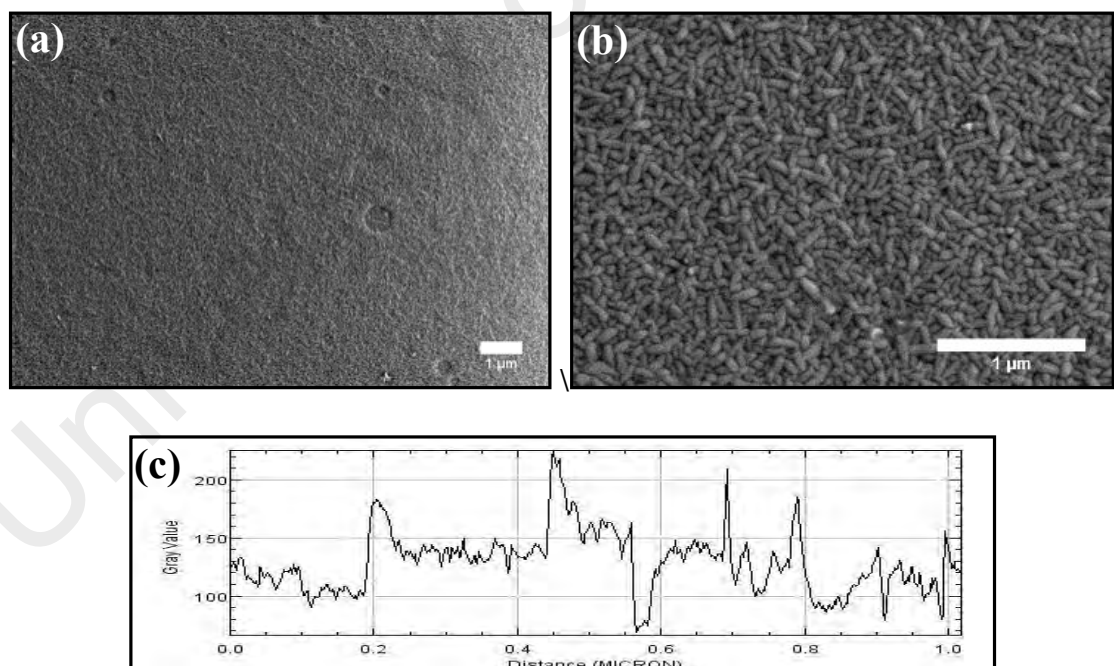


Figure 5.2: (a) & (b) FESEM images and (c) cross-sectional simulation view of P(VDF-TrFE).

Figure 5.2 (a & b) and (c) shows the FESEM images and cross-sectional simulation view of P(VDF-TrFE), respectively. It is clearly seen that P(VDF-TrFE) has a non-homogenous morphology with appearance of rice-like structure is exhibited. This explanation is supported by the non-homogenous distribution of distance shown by the cross-sectional simulation view. It can be concluded that, P(VDF-TrFE) possesses a rice-like structure at its surface. Figure 5.3 (a) & (b) shows the FTIR and XRD spectra of P(VDF-TrFE) after being soaked in different electrolytes, respectively. These analyses are done in order to determine if electrolyte could alter β -phase property of P(VDF-TrFE) after undergo the anodization. In the fabrication of porous AAO template, different types of electrolytes are heavily used by means of anodization and pores widening process. FTIR spectra show that similar peaks in P(VDF-TrFE) presented before and after the P(VDF-TrFE) is being soaked in electrolytes. Wavenumbers of 472.90, 508.24, 880.21, 1116.85, 1172.50, 1234.03, 1399.80 and 1428.69 cm^{-1} represent the polar β -phase while wavenumbers of 880.21, 1170 and 1399.80 cm^{-1} are assigned to symmetric rocking modes of C-F₂, asymmetric stretching mode of C-F₂ and wagging C-H₂, respectively (Costa et al., 2012; Mahdi et al., 2014; Weber et al., 2010). Stretching C-F bond is seen at 523, 543, 549 and 658.08 cm^{-1} , which is the main characteristic of P(VDF-TrFE).

XRD spectra of both before and after electrolytes soaking have exhibited the similar main peak at 20°. This peak is corresponded to (200) and (110) plane of P(VDF-TrFE) (Mao et al., 2011) that related to the presence of polar β -phase. Both of these characterisations are important as their primary function is to detect the presence of polar β -phase in P(VDF-TrFE) before and after the soaking process because polar β -phase is much important for application of VOFET since P(VDF-TrFE) needs to react well to bias from gate electrode for sake of conductivity in VOFET.

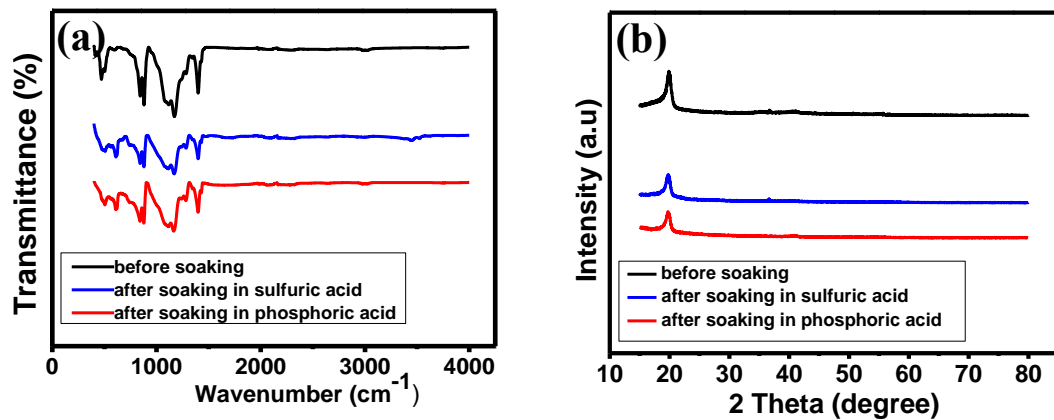


Figure 5.3: Graph of (a) FTIR and (b) XRD before and after P(VDF-TrFE) soaked in anodization and pore widening acids.

5.2.2 Anodization of Aluminium: P(VDF-TrFE)

Figure 5.4 (a) & (b) present the anodization graph of aluminium and aluminium: P(VDF-TrFE), respectively. In both graphs, the decrement of current is primarily originated from the production of barrier layer. Pores are initiated at random positions started from the top surface of aluminium. Current has stopped decreasing until the formation of pore is met. Then, the current is constant which indicate the formation of pores are in self-organizing condition (Sulka & Stepnowski, 2009). Anodization graph of aluminium shows a peak-like graph that mainly due to the further penetration of pores to the substrate since the only interface occurred in this system is between aluminium and substrate. In contrast, two peaks are seen from the aluminium: P(VDF-TrFE) anodization graph. The second peak is most likely due to the presence of P(VDF-TrFE) that allowed the ‘stamping’ process between the AAO template and P(VDF-TrFE) to happen. At this stage, pores are formed down to the P(VDF-TrFE) region rather than to the substrate. Anodizing current is related to the movement of oxygen molecules from acid. For anodization of aluminium, these ions will move through the barrier layer into the interface of oxide layer while Al^{3+} ions will drift across the oxide structure (Sulka & Stepnowski, 2009). Formation of oxide layer is considered sufficient, with the limitation of diffusion of ions due to the high resistance. However, the ions are encountered with the high

resistance that due to the presence of P(VDF-TrFE). Thus, it's led to the appearance of the second peak shown in the graph.

Two different systems of VOFETs are fabricated: (i) VOFET integrated with thin film P(VDF-TrFE) and (ii) VOFET integrated with nanoporous P(VDF-TrFE). FESEM images of these two systems are shown in Figure 5.5 (a) & (b), respectively. Silver nanowire is seen to cover up almost the whole sample with the diameter of nanowires are 20 nm. FESEM cross-sectional views show the different morphology of P(VDF-TrFE) used in VOFETs. Both systems have perforated pattern of silver nanowire on top of the dielectric layer, however, they are different in term of the dielectric layer morphology. As per image (a), the structure of dielectric layer is clearly thin film with smooth and homogenous morphology. There are no distinct structures present in this structure. Contrary to that, image (b) does portray distinctive structures on top of the dielectric layer. These are nanoporous structures that do presence after the anodization process. From the image, their estimated depth is around 200-300 nm. Thin film below the nanoporous is the remained area after anodization since anodization period of 45 minutes just ample to produce nanostructure around 200-300 nm depth.

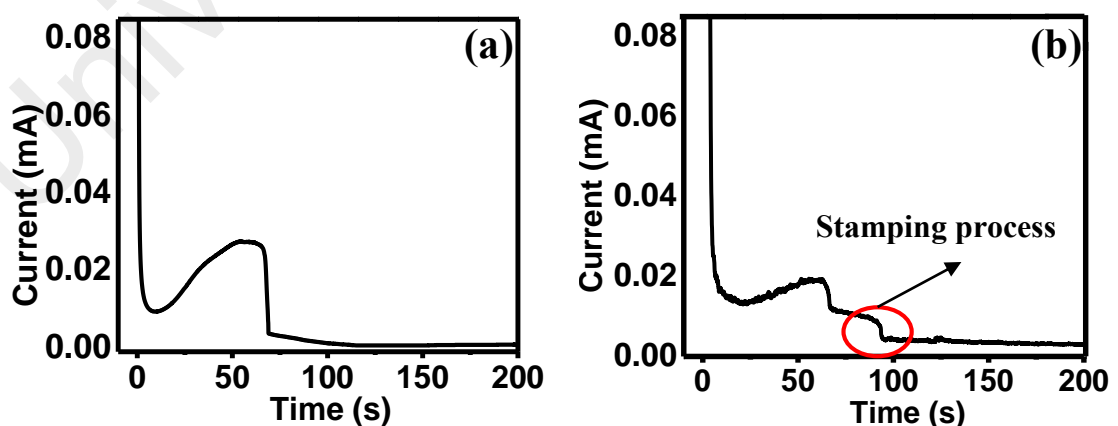


Figure 5.4: Anodization graph of (a) aluminium and (b) aluminium: P(VDF-TrFE).

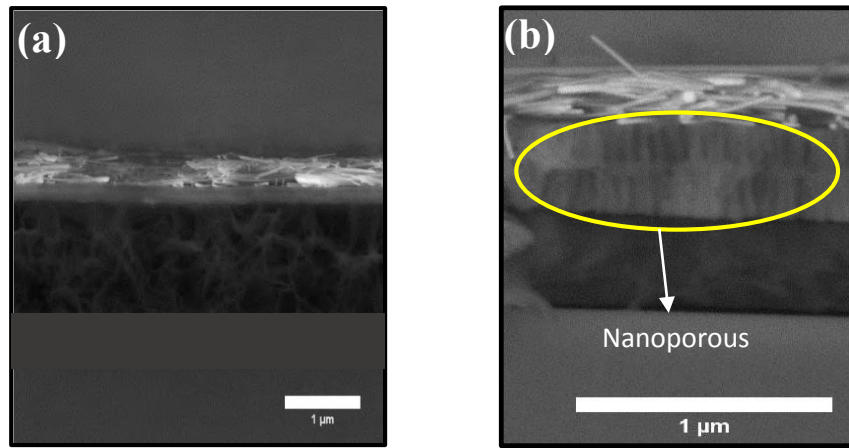


Figure 5.5: FESEM images of (a) P(VDF-TrFE) thin film and (b) nanostructured P(VDF-TrFE).

Figure 5.6 (a) exhibits the layer-by-layer arrangement of VOFET that integrated with P(VDF-TrFE) thin film. The presence of perforated silver nanowire layer enables the accumulation of VOPcPhO inside the nanowire network (hole). In this system, only the silver nanowire exhibits the porous structures while other layers such as ITO, dielectric, VOPcPhO and aluminium electrode are deposited in the thin film form. Figure 5.6 (b) shows the layer-by-layer arrangement of VOFET, which integrated with P(VDF-TrFE) nanoporous. The main difference between the two systems is the latter system has the incorporation of nanoporous dielectric layer that embedded within the device. Due to the perforated structure exhibited by the silver nanowire network, VOPcPhO is expected to fill and not to fill some of the nanoporous. Some of these nanoporous are assumed not to fill with VOPcPhO due to their locations that are fully direct under the nanowires that leads blockade. The role of silver nanowires networks is to act as the ‘perforated’ area that represents spaces between the nanowires in order to increase the number of charge carrier. The transparency properties of metal nanowires have also play a role in VOFET performance. High transparent metal nanowires could benefit to the two functional parts of VOFET, which is capacitor and diode parts that located at the bottom and top of source electrode (Ben-Sasson et al., 2015).

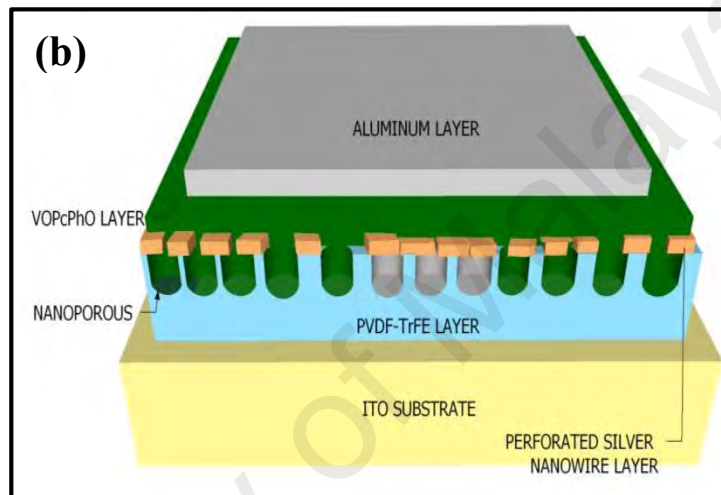
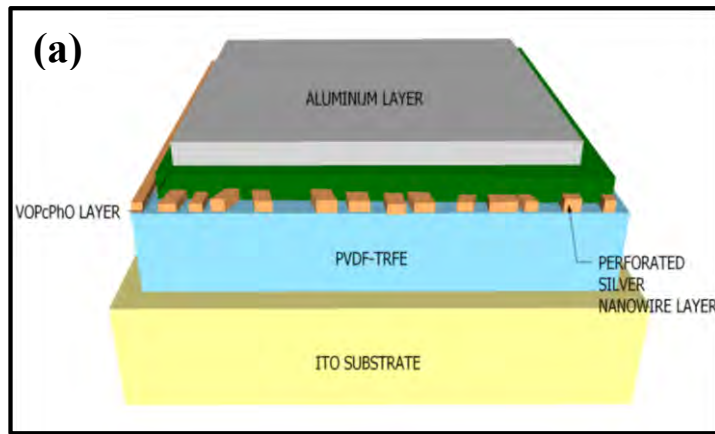


Figure 5.6: Cross-sectional view of fabricated VOFETs of (a) P(VDF-TrFE) thin film and (b) nanostructured P(VDF-TrFE).

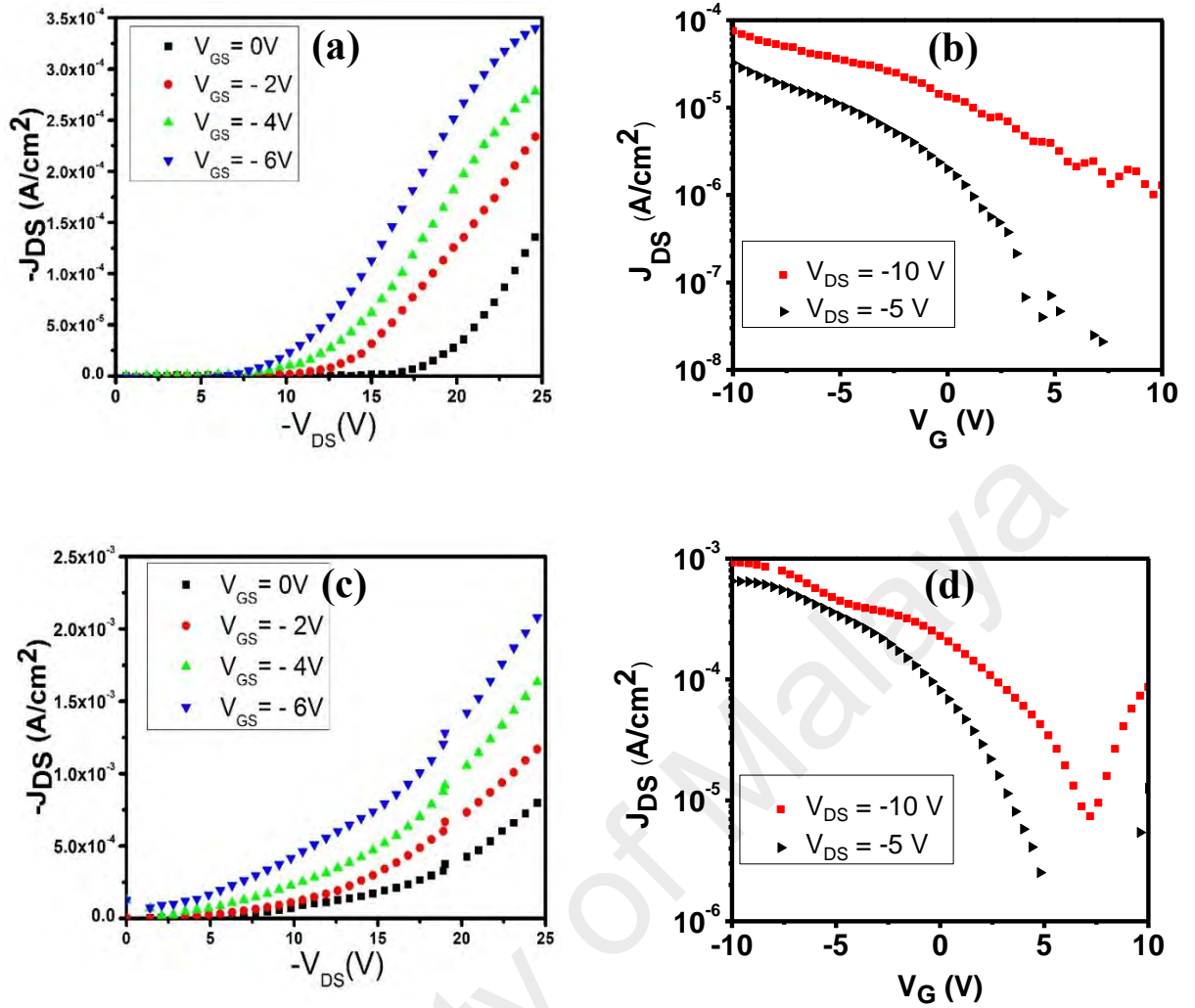


Figure 5.7: Output graph of VOFET integrated with (a) P(VDF-TrFE) thin film & (c) nanostructured P(VDF-TrFE). Transfer graph of VOFET integrated with (b) P(VDF-TrFE) thin film (d) nanostructured P(VDF-TrFE).

Figure 5.7 (a-d) shows the output and transfer characteristics graphs of VOFET fabricated with P(VDF-TrFE) thin film and nanostructured P(VDF-TrFE). For output characteristics shown in Figure 5.7 (a), V_{DS} swept from 0 to -25 V with variation of V_{GS} from 0 to 6 V. The maximum current density achieved for V_G of 6 V and V_{DS} of 25 V is $\sim 3.5 \times 10^{-4}$ A/cm² which is comparable or higher than VOFET reported by other researcher which are 1.0×10^{-4} A/cm² at unstated V_G bias (Ben-Sasson et al., 2009). This value also is higher than some of values reported by other researchers 1.2×10^{-6} A/cm² at $V_{GS} = -40$ V (Stutzmann et al., 2003) and 5.5×10^{-6} A/cm² at $V_{GS} = 0$ V (Kudo et al., 2001). This may due to the application of silver nanowire as perforated source electrode that can enhance and accumulate the number of electrons, which will reside between the

perforated networks (Ben-Sasson et al., 2015). This thin film VOFET recorded the turn on voltage (when $V_{GS} = 0$ V) of ~ 10 V. Figure 5.7 (c) shows the output characteristic of VOFET with nanoporous structure in dielectric layer. From the graph, it can be seen that VOFET can be enhanced for its maximum current density to 2.0×10^{-3} A/cm². In addition, turn on voltage is decreased from 10 V to 7 V.

From the transfer graphs (Figure 5.7 (b) & (d)), it shows that the V_G is swept from -10 to 10 V at V_{DS} of -5 and -10 V. Values of drain current, I_{DS} of the transistor is increased towards negative values of V_{DS} . This depicts that these transistors are having *p*-type semiconducting materials of VOPcPhO as reported by previous work (Makinudin et al., 2015). For *p*-type material (VOPcPhO), current will flow when the $V_{GS} < 0$ V and experimentally, the I_{ON}/I_{OFF} ratio calculated from this graph obtained by dividing the maximum I_{DS} over its pinch off currents. This ratio does indicates the device's ability to shut down and this characteristic can be utilised in applications likewise logic circuits and matrix active displays (Horowitz, 1998). I_{ON}/I_{OFF} ratios obtained from these graphs are $\sim 10^3$ for V_G of 5 V and $\sim 10^2$ for 10 V of both systems.

Figure 5.8 (a) & (b) exhibit two possible schematic diagrams of contact areas that related with Figure 5.6 (a) and (b) between source electrode and organic layer with the presence of non-porous and porous P(VDF-TrFE) within the VOFET, respectively (Ben-Sasson et al., 2009; Ben-Sasson et al., 2015; Ben-Sasson et al., 2014). In the presence of non-porous copolymer with the patterned or perforated source electrode, electric field from dielectric layer will move upwards and focused more through the perforated areas rather than areas covered by silver nanowire structures (Ben-Sasson et al., 2009). Therefore, more electrons will accumulate inside the perforated structures as following the electric field from dielectric layer. Besides that, the semiconductor layer has already filled up the perforated networks. As in Schottky concept, when the bias is applied to gate

electrode, semiconducting material will sweep charge carriers from source towards drain to complete the circuit.

In porous integrated VOFET system, there are three possible structures arrangements occurred between the dielectric layer and silver nanowire. The mechanisms of charge carrier movements involved in these three arrangements are still not fully understandable yet. In assumption, the first possible arrangement (marked by double ring-sided circle in Figure 5.8 (b)) is assumed as a perforated network (hole) of silver nanowire being occurred directly on top of the porous. This possible arrangement may not enable the accumulation of electrons inside the perforated holes due to electric field defocused from the perforated hole. Thus, positive charges (electric field) from dielectric layer attract the electrons from the nanowires to accumulate at the contact area between nanowires and P(VDF-TrFE) without the electrons being accumulated inside the perforated network (hole). This may reduce the sweeping process by semiconductor since electrons do not directly contact with the material. The second possible arrangement (marked by normal-sided circle in Figure 5.8 (b)) assumed that this arrangement could provide better field from dielectric layer since the porous is located directly below the source electrode region. Thus, the probability of the electrons to accumulate inside the perforated holes and semiconductor material is high. This occurrence will then enable the movement of charge carrier to be easily swept by semiconducting material as in first system of VOFET. The third possible arrangement (marked by dash-sided circle in Figure 5.8 (b)) predicted that from this structure, the porous is semi-exposed by the perforated hole, with semiconductor material can still be able to involve in contact. Since the electric field will be dominant in the perforated hole, charges will locate at the border between porous and perforated hole. This occurrence will enable the accumulation of electrons from silver nanowire towards perforated hole. In addition, more electrons from nanowire can be attracted from the bottom parts to be accumulated inside the porous that has been previous filled with

semiconductor. This condition could allow more electrons to be swept by the semiconducting material. We can assume that this arrangement most likely occurred in our VOFET since the probability for perforated hole or silver nanowire network to be placed fully on top of porous is much less than probability of them to partially on top of porous structures. This is due to the scattered locations of silver nanowire and almost similar diameter between porous and nanowires. The output current of VOFET can be improved and increased if compared with the non-porous integrated VOFET, which in this case is higher 5-6 times.

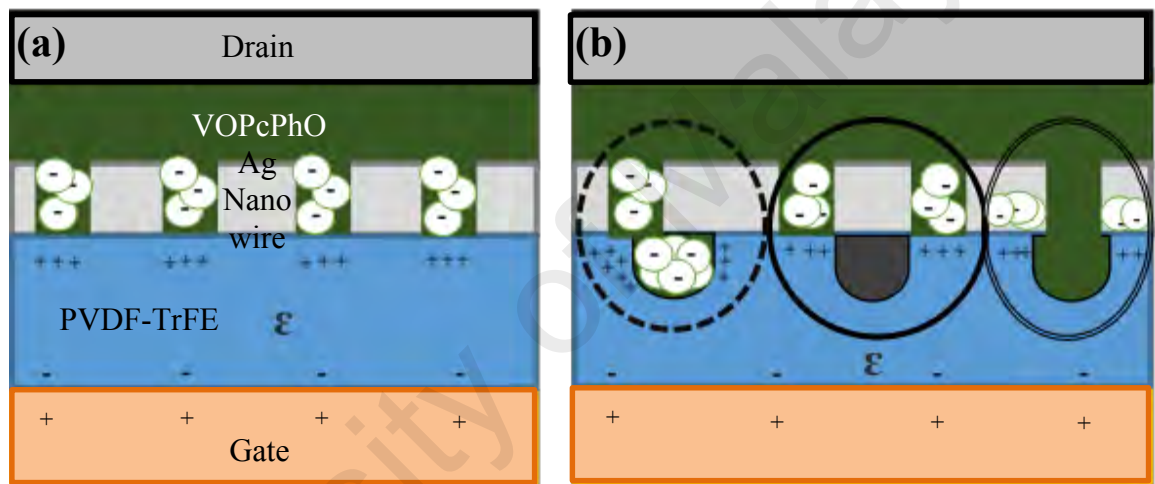


Figure 5.8: Schematic diagram of differences in effective contact areas between single silver nanowire and VOPcPhO of (a) non-porous and (b) porous structures.

5.3 Summary

P(VDF-TrFE) can be anodized without altering its original properties and elements. Since two systems of VOFET structure are fabricated, we are comparing the electrical properties of these systems. The output and transfer graphs shown that VOFET with porous dielectric layer enable to produce the higher output current and lower turn on voltage. In summary, the enhancement of output current at 25 V of V_{GS} is done by applying nanostructured dielectric layer. Besides, the turn on voltage can be reduced from 10 V to 7 V. However, the ON/OFF ratio is almost the same for both systems. Table 5.1 illustrates the comparison of basic performances between VOFET of both systems.

Table 5.1: IV curve data of thin film and nanostructured dielectric layer.

Measurements	Thin film dielectric layer	Nanostructured dielectric layer
Highest output current at 25V	3×10^{-4} A	2.5×10^{-3} A
Turn on voltage	10 V	7 V
ON/OFF ratio	10^3 - V_G of 5V 10^2 - V_G of 10V	10^3 - V_G of 5V 10^2 - V_G of 10V

University of Malaya

CHAPTER 6: CONCLUSION AND FUTURE WORKS

6.1 Conclusion

The fabrication of porous AAO template on glass substrate via the single-step anodization technique, which later infiltrated by VOPcPhO has successfully been realised. Instead of hexagonal shape of nanoporous as normally produced by anodization, rounded-sphere shape of nanoporous is mostly formed. Stirring or without stirring process can affect to the uniformity and homogeneity of the pores size and density of pores. In addition to the stirring treatment, pore widening treated in different molarity of phosphoric acid can lead to the changes of morphology. Optical properties have suggested that porous AAO template synthesized from higher stirring speed exhibited a better transmittance and refractive index. Infiltration of VOPcPhO into the template has been proven by the observation of its morphological and optical properties. AAO: VOPcPhO nanocomposite has a potential to be employed in sensor applications.

P(VDF-TrFE) can be anodized without altering its original properties and elements. The current reading of anodization with P(VDF-TrFE) suggests that AAO template 'stamping' does occur. Last but not least, we succeeded in fabricating the VOFET of both systems i.e. with thin film and nanostructured dielectric layer. The output and transfer graphs exhibited that nanostructured VOFET is enable to produce the higher output current and lower turn on voltage.

6.2 Future Works

As for now, this work is able to prove that the construction of new architecture from lateral OFET to vertical OFET can enhance the output current and turn on voltage. Furthermore, by nanostructuring the dielectric layer, we can further increase the output current of VOFET. Besides, by applying VOPcPhO as semiconducting material, environmentally friendly atmosphere in electronics fabrication can be preserved. However, one of biggest challenges in the fabrication of VOFET is its difficulty to be reproduced for enormous scale production as it consumes time and requires many steps to be fabricated. Besides, industry demands now requires researchers all over the world to fabricate transistor with much higher output current with much lower turn on voltage as to compete with inorganic FET performance, but with safer and environmentally friendly organic device.

In this work, the silver nanowires as source does lie on top of dielectric layer with direct contact with the thin film or nanostructured dielectric layer. Thus, for future work, ones can apply the usage of AAO template to produce the standing silver nanowires. By having the freestanding silver nanowires, more electrons from silver nanowires can be accumulated between them or even in nanostructured dielectric layer (in case ones applying nanostructure replication steps as in this work). Apart from that, more effective area between nanowires and semiconducting material can be obtained by having this configuration. Hence, this can enable these accumulated electrons to be transferred to drain electrode easier and faster.

REFERENCES

- Abdullah, S. M., Ahmad, Z., Aziz, F., & Sulaiman, K. (2012). Investigation of VOPcPhO as an acceptor material for bulk heterojunction solar cells. *Organic Electronics*, *13*(11), 2532-2537.
- Allard, S., Forster, M., Souharce, B., Thiem, H., & Scherf, U. (2008). Organic semiconductors for solution-processable field-effect transistors (OFETs). *Angewandte Chemie International Edition*, *47*(22), 4070-4098.
- Ashar, A., & Narayan, K. (2017). Electric field induced ferroelectric-surface modification for high mobility organic field effect transistors. *Organic Electronics*, *42*, 8-12.
- Azmer, M. I., Ahmad, Z., Sulaiman, K., & Touati, F. (2016). Morphological and structural properties of VoPcPhO: P3HT composite thin films. *Materials Letters*, *164*, 605-608.
- Azmer, M. I., Zafar, Q., Ahmad, Z., Sulaiman, K., & Karimov, K. S. (2014). VOPcPhO based organic pressure sensor and displacement transducer. *Synthetic Metals*, *191*, 120-125.
- Bakar, N. A., Supangat, A., & Sulaiman, K. (2014). Elaboration of PCDTBT nanorods and nanoflowers for augmented morphological and optical properties. *Materials Letters*, *131*, 27-30.
- Balde, M., Vena, A., & Sorli, B. (2015). Fabrication of porous anodic aluminium oxide layers on paper for humidity sensors. *Sensors and Actuators B: Chemical*, *220*, 829-839.
- Bao, Z. (2000). Materials and fabrication needs for low-cost organic transistor circuits. *Advanced Materials*, *12*(3), 227-230.
- Bao, Z., Dodabalapur, A., & Lovinger, A. J. (1996). Soluble and processable regioregular poly (3-hexylthiophene) for thin film field-effect transistor applications with high mobility. *Applied Physics Letters*, *69*(26), 4108-4110.
- Beaupré, S., & Leclerc, M. (2013). PCDTBT: en route for low cost plastic solar cells. *Journal of Materials Chemistry A*, *1*(37), 11097-11105.
- Ben-Sasson, A. J., Ankonina, G., Greenman, M., Grimes, M. T., & Tessler, N. (2013). Low-temperature molecular vapor deposition of ultrathin metal oxide dielectric for low-voltage vertical organic field effect transistors. *ACS Applied Materials & Interfaces*, *5*(7), 2462-2468.
- Ben-Sasson, A. J., Avnon, E., Ploshnik, E., Globberman, O., Shenhar, R., Frey, G. L., & Tessler, N. (2009). Patterned electrode vertical field effect transistor fabricated using block copolymer nanotemplates. *Applied Physics Letters*, *95*(21), 213301.
- Ben-Sasson, A. J., Azulai, D., Gilon, H., Facchetti, A., Markovich, G., & Tessler, N. (2015). Self-assembled metallic nanowire-based vertical organic field-effect transistor. *ACS Applied Materials & Interfaces*, *7*(4), 2149-2152.

- Ben-Sasson, A. J., & Tessler, N. (2012). Unraveling the physics of vertical organic field effect transistors through nanoscale engineering of a self-assembled transparent electrode. *Nano Letters*, 12(9), 4729-4733.
- Ben-Sasson, A. J., Greenman, M., Roichman, Y., & Tessler, N. (2014). The mechanism of operation of lateral and vertical organic field effect transistors. *Israel Journal of Chemistry*, 54(5-6), 568-585.
- Chau, R., Datta, S., Doczy, M., Doyle, B., Kavalieros, J., & Metz, M. (2004). High- κ /metal-gate stack and its MOSFET characteristics. *IEEE Electron Device Letters*, 25(6), 408-410.
- Costa, C. M., Rodrigues, L., Sencadas, V., Silva, M. M., & Lanceros-Méndez, S. (2012). Effect of the microstructure and lithium-ion content in poly [(vinylidene fluoride)-co-trifluoroethylene]/lithium perchlorate trihydrate composite membranes for battery applications. *Solid State Ionics*, 217, 19-26.
- Cui, Y., Zhong, Z., Wang, D., Wang, W. U., & Lieber, C. M. (2003). High performance silicon nanowire field effect transistors. *Nano Letters*, 3(2), 149-152.
- Davis, E., & Mott, N. (1970). Conduction in non-crystalline systems V. Conductivity, optical absorption and photoconductivity in amorphous semiconductors. *Philosophical Magazine*, 22(179), 0903-0922.
- Diggle, J. W., Downie, T. C., & Goulding, C. (1969). Anodic oxide films on aluminum. *Chemical Reviews*, 69(3), 365-405.
- Dimitrakopoulos, C., Purushothaman, S., Kymissis, J., Callegari, A., & Shaw, J. (1999). Low-voltage organic transistors on plastic comprising high-dielectric constant gate insulators. *Science*, 283(5403), 822-824.
- Drury, A., Chaure, S., Kröll, M., Nicolosi, V., Chaure, N., & Blau, W. J. (2007). Fabrication and characterization of silver/polyaniline composite nanowires in porous anodic alumina. *Chemistry of Materials*, 19(17), 4252-4258.
- Durban, M. M., Kazarinoff, P. D., & Luscombe, C. K. (2010). Synthesis and characterization of thiophene-containing naphthalene diimide n-type copolymers for OFET applications. *Macromolecules*, 43(15), 6348-6352.
- Facchetti, A. (2007). Semiconductors for organic transistors. *Materials Today*, 10(3), 28-37.
- Fakir, M. S., Supangat, A., & Sulaiman, K. (2014). Templated growth of PFO-DBT nanorod bundles by spin coating: effect of spin coating rate on the morphological, structural, and optical properties. *Nanoscale Research Letters*, 9(1), 225.
- Fan, Z., Wang, D., Chang, P.-C., Tseng, W.-Y., & Lu, J. G. (2004). ZnO nanowire field-effect transistor and oxygen sensing property. *Applied Physics Letters*, 85(24), 5923-5925.
- Gamerith, S., Klug, A., Scheiber, H., Scherf, U., Moderegger, E., & List, E. J. (2007). Direct Ink-Jet Printing of Ag-Cu Nanoparticle and Ag-Precursor Based

- Electrodes for OFET Applications. *Advanced Functional Materials*, 17(16), 3111-3118.
- Geffroy, B., Le Roy, P., & Prat, C. (2006). Organic light-emitting diode (OLED) technology: materials, devices and display technologies. *Polymer International*, 55(6), 572-582.
- Horowitz, G. (1998). Organic field-effect transistors. *Advanced Materials*, 10(5), 365-377.
- Hou, Q., Chen, J., & Cao, Y. (2006). Luminescence and photovoltaic cells of benzoselenadiazole-containing polyfluorenes. *Synthetic Metals*, 156(5), 470-475.
- Houng, M.-P., Lu, W.-L., Yang, T.-H., & Lee, K.-W. (2014). Characterization of the nanoporous template using anodic alumina method. *Journal of Nanomaterials*, 2014.
- Hu, W., Gong, D., Chen, Z., Yuan, L., Saito, K., Grimes, C. A., & Kichambare, P. (2001). Growth of well-aligned carbon nanotube arrays on silicon substrates using porous alumina film as a nanotemplate. *Applied Physics Letters*, 79(19), 3083-3085.
- Hu, Z., Tian, M., Nysten, B., & Jonas, A. M. (2009). Regular arrays of highly ordered ferroelectric polymer nanostructures for non-volatile low-voltage memories. *Nature Materials*, 8(1), 62-67.
- Hwang, D. K., Fuentes-Hernandez, C., Kim, J., Potscavage, W. J., Kim, S. J., & Kippelen, B. (2011). Top-Gate Organic Field-Effect Transistors with High Environmental and Operational Stability. *Advanced Materials*, 23(10), 1293-1298.
- Ismail, L., Fuad, A. A., Wahid, M., Habibah, Z., Norsabrina, S., & Nazirah, M. (2015). *Study on the effect of PVDF-TrFE layer to the electrical properties of MIS devices*. Paper presented at the IOP Conference Series: Materials Science and Engineering.
- Javey, A., Guo, J., Wang, Q., Lundstrom, M., & Dai, H. (2003). Ballistic carbon nanotube field-effect transistors. *Nature*, 424(6949), 654-657.
- Jones, B. A., Facchetti, A., Wasielewski, M. R., & Marks, T. J. (2008). Effects of Arylene Diimide Thin Film Growth Conditions on n-Channel OFET Performance. *Advanced Functional Materials*, 18(8), 1329-1339.
- Kamarundzaman, A., Fakir, M. S., Supangat, A., Sulaiman, K., & Zulfiqar, H. (2013). Morphological and optical properties of hierarchical tubular VOPcPhO nanoflowers. *Materials Letters*, 111, 13-16.
- Keren, K., Berman, R. S., Buchstab, E., Sivan, U., & Braun, E. (2003). DNA-templated carbon nanotube field-effect transistor. *Science*, 302(5649), 1380-1382.
- Kudo, K., Iizuka, M., Kuniyoshi, S., & Tanaka, K. (2001). Device characteristics of lateral and vertical type organic field effect transistors. *Thin Solid Films*, 393(1), 362-367.

- Kyotani, T., Tsai, L.-f., & Tomita, A. (1996). Preparation of ultrafine carbon tubes in nanochannels of an anodic aluminum oxide film. *Chemistry of Materials*, 8(8), 2109-2113.
- Li, F., Zhang, L., & Metzger, R. M. (1998). On the growth of highly ordered pores in anodized aluminum oxide. *Chemistry of Materials*, 10(9), 2470-2480.
- Li, T., Ruden, P., Campbell, I., & Smith, D. (2003). Investigation of bottom-contact organic field effect transistors by two-dimensional device modeling. *Journal of Applied Physics*, 93(7), 4017-4022.
- Li, Y., Xu, D., Zhang, Q., Chen, D., Huang, F., Xu, Y., Gu, Z. (1999). Preparation of cadmium sulfide nanowire arrays in anodic aluminum oxide templates. *Chemistry of Materials*, 11(12), 3433-3435.
- Lin, H.-C., Zan, H.-W., Chao, Y.-C., Chang, M.-Y., & Meng, H.-F. (2015). Review of a solution-processed vertical organic transistor as a solid-state vacuum tube. *Semiconductor Science and Technology*, 30(5), 054003.
- Lu, G., Blakesley, J., Himmelberger, S., Pingel, P., Frisch, J., Lieberwirth, I., Salleo, A. (2013). Moderate doping leads to high performance of semiconductor/insulator polymer blend transistors. *Nature Communications*, 4, 1588.
- Ma, L., & Yang, Y. (2004). Unique architecture and concept for high-performance organic transistors. *Applied Physics Letters*, 85(21), 5084-5086.
- Mahdi, R. I., Gan, W., & Majid, W. (2014). Hot plate annealing at a low temperature of a thin ferroelectric P (VDF-TrFE) film with an improved crystalline structure for sensors and actuators. *Sensors*, 14(10), 19115-19127.
- Makinudin, A. H. A., Fakir, M. S., & Supangat, A. (2015). Metal phthalocyanine: fullerene composite nanotubes via templating method for enhanced properties. *Nanoscale Research Letters*, 10(1), 1-8.
- Małachowski, M., & Żmija, J. (2010). Organic field-effect transistors. *Opto-Electronics Review*, 18(2), 121-136.
- Mao, D., Gnade, B. E., & Quevedo-Lopez, M. A. (2011). *Ferroelectric Properties and Polarization Switching Kinetic of Poly (vinylidene fluoride-trifluoroethylene) Copolymer*: INTECH Open Access Publisher.
- Masuda, H., & Fukuda, K. (1995). Ordered metal nanohole arrays made by a two-step replication of honeycomb structures of anodic alumina. *Science*, 268(5216), 1466.
- Masuda, H., Yada, K., & Osaka, A. (1998). Self-ordering of cell configuration of anodic porous alumina with large-size pores in phosphoric acid solution. *Japanese Journal of Applied Physics*, 37(11A), L1340.
- Minami, T., Sato, T., Minamiki, T., Fukuda, K., Kumaki, D., & Tokito, S. (2015). A novel OFET-based biosensor for the selective and sensitive detection of lactate levels. *Biosensors and Bioelectronics*, 74, 45-48.

- Muccini, M. (2006). A bright future for organic field-effect transistors. *Nature Materials*, 5(8), 605-613.
- Naber, R., De Boer, B., Blom, P., & De Leeuw, D. (2005). Low-voltage polymer field-effect transistors for nonvolatile memories. *Applied Physics Letters*, 87(20), 203509-203509.
- Natali, D., Fumagalli, L., & Sampietro, M. (2007). Modeling of organic thin film transistors: Effect of contact resistances. *Journal of Applied Physics*, 101(1), 014501.
- Pauling, L. (1960). *The Nature of The Chemical Bond and The Structure of Molecules and Crystals: An Introduction to Modern Structural Chemistry* (Vol. 18): Cornell University press.
- Peitao, G., Zhilin, X., Yiyu, X., Caihua, H., & Lixin, Z. (2011). Morphology and transmittance of porous alumina on glass substrate. *Applied Surface Science*, 257(8), 3307-3312.
- Rahman, S., & Yang, H. (2003). Nanopillar arrays of glassy carbon by anodic aluminum oxide nanoporous templates. *Nano Letters*, 3(4), 439-442.
- Rost, C., Karg, S., Riess, W., Loi, M. A., Murgia, M., & Muccini, M. (2004). Ambipolar light-emitting organic field-effect transistor. *Applied Physics Letters*, 85(9), 1613-1615.
- Routkevitch, D., Bigioni, T., Moskovits, M., & Xu, J. M. (1996). Electrochemical fabrication of CdS nanowire arrays in porous anodic aluminum oxide templates. *The Journal of Physical Chemistry*, 100(33), 14037-14047.
- Scharber, M. C., Mühlbacher, D., Koppe, M., Denk, P., Waldauf, C., Heeger, A. J., & Brabec, C. J. (2006). Design rules for donors in bulk-heterojunction solar cells—Towards 10% energy-conversion efficiency. *Advanced Materials*, 18(6), 789-794.
- Schneider, D., Valiullin, R., & Monson, P. A. (2014). Filling dynamics of closed end nanocapillaries. *Langmuir*, 30(5), 1290-1294.
- Shankar, K. S., & Raychaudhuri, A. (2005). Fabrication of nanowires of multicomponent oxides: Review of recent advances. *Materials Science and Engineering: C*, 25(5), 738-751.
- Shen, L., Ali, M., Gu, Z., Min, B., Kim, D., & Park, C. (2013). Preparation of anodic aluminum oxide (AAO) nano-template on silicon and its application to one-dimensional copper nano-pillar array formation. *Korean Journal of Chemical Engineering*, 1-7.
- Sirringhaus, H. (2014). 25th Anniversary Article: Organic Field-Effect Transistors: The Path Beyond Amorphous Silicon. *Advanced Materials*, 26(9), 1319-1335.
- So, F. (2009). *Organic Electronics: Materials, Processing, Devices and Applications*: CRC press.

- Song, M., You, D. S., Lim, K., Park, S., Jung, S., Kim, C. S., Park, J. (2013). Highly efficient and bendable organic solar cells with solution-processed silver nanowire electrodes. *Advanced Functional Materials*, 23(34), 4177-4184.
- Stutzmann, N., Friend, R. H., & Sirringhaus, H. (2003). Self-aligned, vertical-channel, polymer field-effect transistors. *Science*, 299(5614), 1881-1884.
- Suh, J. S., & Lee, J. S. (1999). Highly ordered two-dimensional carbon nanotube arrays. *Applied Physics Letters*, 75(14), 2047-2049.
- Sui, Y., Acosta, D., Gonzalez-Leon, J., Bermudez, A., Feuchtwanger, J., Cui, B., Saniger, J. (2001). Structure, thermal stability, and deformation of multibranched carbon nanotubes synthesized by CVD in the AAO template. *The Journal of Physical Chemistry B*, 105(8), 1523-1527.
- Sulka, G., & Parkoła, K. (2007). Temperature influence on well-ordered nanopore structures grown by anodization of aluminium in sulphuric acid. *Electrochimica Acta*, 52(5), 1880-1888.
- Sulka, G. D., & Stępniewski, W. J. (2009). Structural features of self-organized nanopore arrays formed by anodization of aluminum in oxalic acid at relatively high temperatures. *Electrochimica Acta*, 54(14), 3683-3691.
- Sun, Y. (2010). Silver nanowires—unique templates for functional nanostructures. *Nanoscale*, 2(9), 1626-1642.
- Sun, Y., Liu, Y., & Zhu, D. (2005). Advances in organic field-effect transistors. *Journal of Materials Chemistry*, 15(1), 53-65.
- Supangat, A., Kamarundzaman, A., Bakar, N. A., Sulaiman, K., & Zulfiqar, H. (2014). P3HT: VOPcPhO composite nanorods arrays fabricated via template-assisted method: Enhancement on the structural and optical properties. *Materials Letters*, 118, 103-106.
- Taşaltın, N., Öztürk, S., Kılınc, N., Yüzer, H., & Öztürk, Z. Z. (2009). Simple fabrication of hexagonally well-ordered AAO template on silicon substrate in two dimensions. *Applied Physics A*, 95(3), 781-787.
- Tashiro, K. (1995). Crystal structure and phase transition of PVDF and related copolymers. *Plastics Engineering-New York-*, 28, 63-63.
- Wang, G., Luo, Y., & Beton, P. H. (2003). High mobility organic transistors fabricated from single pentacene microcrystals grown on a polymer film. *Applied Physics Letters*, 83(15), 3108-3110.
- Wang, G., Moses, D., Heeger, A. J., Zhang, H.-M., Narasimhan, M., & Demaray, R. (2004). Poly (3-hexylthiophene) field-effect transistors with high dielectric constant gate insulator. *Journal of Applied Physics*, 95(1), 316-322.
- Wang, X., & Han, G.-R. (2003). Fabrication and characterization of anodic aluminum oxide template. *Microelectronic Engineering*, 66(1), 166-170.

- Weber, N., Lee, Y.-S., Shanmugasundaram, S., Jaffe, M., & Arinzeh, T. L. (2010). Characterization and in vitro cytocompatibility of piezoelectric electrospun scaffolds. *Acta Biomaterialia*, 6(9), 3550-3556.
- Wu, J., Becerril, H. A., Bao, Z., Liu, Z., Chen, Y., & Peumans, P. (2008). Organic solar cells with solution-processed graphene transparent electrodes. *Applied Physics Letters*, 92(26), 237.
- Xu, H., Shanthi, G., Bharti, V., Zhang, Q., & Ramotowski, T. (2000). Structural, conformational, and polarization changes of poly (vinylidene fluoride-trifluoroethylene) copolymer induced by high-energy electron irradiation. *Macromolecules*, 33(11), 4125-4131.
- Yamashita, Y. (2009). Organic semiconductors for organic field-effect transistors. *Science and Technology of Advanced Materials*, 10(2), 024313.
- Yan, H., Chen, Z., Zheng, Y., Newman, C., Quinn, J. R., Dötz, F., Facchetti, A. (2009). A high-mobility electron-transporting polymer for printed transistors. *Nature*, 457(7230), 679-686.
- Yang, Y., & Wudl, F. (2006). *High Performance Organic Materials and Devices*. Retrieved from
- Yu, H., Dong, Z., Guo, J., Kim, D., & So, F. (2016). Vertical Organic Field-Effect Transistors for Integrated Optoelectronic Applications. *ACS Applied Materials & Interfaces*, 8(16), 10430-10435.
- Zafar, Q., Ahmad, Z., Sulaiman, K., Hamzah, A. S., & Rahman, Z. A. (2014). A MEHPPV/VOPcPhO composite based diode as a photodetector. *Sensors and Actuators A: Physical*, 206, 138-143.
- Zhao, S., Roberge, H., Yelon, A., & Veres, T. (2006). New application of AAO template: a mold for nanoring and nanocone arrays. *Journal of the American Chemical Society*, 128(38), 12352-12353.
- Zhuo, H., Peng, F., Lin, L., Qu, Y., & Lai, F. (2011). Optical properties of porous anodic aluminum oxide thin films on quartz substrates. *Thin Solid Films*, 519(7), 2308-2312.
- Zolper, J. (1998). A review of junction field effect transistors for high-temperature and high-power electronics. *Solid-State Electronics*, 42(12), 2153-2156.

LIST OF PUBLICATIONS AND PAPER PRESENTED

- 1 **Halizan, M. Z. M.**, Makinudin, A. H. A., & Supangat, A. (2016). Infiltration of VOPcPhO into porous alumina template grown by in situ method. *RSC Advances*, 6(44), 37574-37582 (ISI-Cited Publications).
- 2 **Halizan, M. Z. M.**, Roslan, N. A., Abdullah, S. M., Halim, N. A., Velayutham, T. S., Woon, K. L., & Supangat, A. (2017). Improving the operational voltage of vertical organic field effect transistor (VOFET) by altering the morphology of dielectric layer. *Journal of Materials Science: Materials in Electronics*, 1-8 (ISI-Cited Publications).

University of Malaya